# Ultra-fast electronic pulse control at cryogenic temperatures

Martin Schalk

Martin Schalk. Ultra-fast electronic pulse control at cryogenic temperatures. Quantum Physics [quant-ph]. Université Grenoble Alpes, 2019. English. NNT : 2019GREAY061 . tel-02619748

HAL Id: tel-02619748
https://theses.hal.science/tel-02619748v1
Submitted on 25 May 2020

Communauté
UNIVERSITÉ Grenoble Alpes

**THÈSE**

Pour obtenir le grade de

**DOCTEUR DE LA COMMUNAUTÉ UNIVERSITÉ GRENOBLE ALPES**
Spécialité : **Physique de la Matière Condensée et du Rayonnement**

Arrêté ministériel : 25 mai 2016

Présentée par

**Martin SCHALK**

Thèse dirigée par **Christopher BÄUERLE**

préparée au sein du **CNRS au Laboratoire Institut Néel**
dans **l'École Doctorale de Physique**

# Ultra-fast electronic pulse control at cryogenic temperatures

# Contrôle électronique ultra-rapide d'impulsion à températures cryogéniques

Thèse soutenue publiquement le **12 novembre 2019**,
devant le jury composé de :

**Olivier BOURGEOIS**
Directeur de recherche, Institut Néel, Université Grenoble Alpes, Président
**Christophe CHAUBET**
Professeur, L2C, Université Montpellier II, Rapporteur
**Yong JIN**
Directeur de recherche, C2N, Université de Paris Saclay, Rapporteur
**Clemens WINKELMANN**
Professeur associé, INPG, Université Grenoble Alpes, Examinateur
**Stephan LUDWIG**
Directeur de recherche, PDI, Université Humboldt de Berlin, Examinateur

# ABSTRACT

## Ultra-fast electronic pulse control at cryogenic temperatures

Martin Schalk

2019

Ultra-fast synchronization, pulse shaping, and efficient switching are at the heart of precise, time-resolved measurements. The aim of this thesis project is to bring ultra-fast electronic control to small nano-metric circuits cooled down to mK temperatures. The fast quantum operation will bring the field of quantum-electronic optics closer to its photonic counterpart with applications for fast and efficient electronic control in quantum devices. To this end, the experimental setups developed during the thesis project are described and tested in a way to outline also possible device integration for scalable solid-state quantum technology. As a first step, a Lorentzian-shaped voltage pulse with a full width half maximum $\Gamma = (76 \pm 2)$ ps is measured in a time-resolved manner at cryogenic temperatures. Secondly, the phase and amplitude drifts are analyzed and optimized together with the noise spectrum. A new pulse generation setup using a microwave frequency comb generator is then described and tested. Finally, a future realization of a quantum interference experiment by manipulating and detecting electronic pulses in a quantum conductor is described along with challenges for low-temperature quantum hardware and interconnects.

# CONTENTS

# ACKNOWLEDGMENTS

I want to express my sincere gratitude to my supervisor, Christopher Bäuerle, for guiding me through the process of my PhD. From my very first day to the final drafts of my thesis, he has been extremely helpful at every step of my academic path. I enjoyed and felt encouraged working with him. Always available yet never micromanaging, he provided the perfect environment for me to grow as a researcher and personality. Benefiting from his immense experience in experimental quantum science and cryogenics I was able to surpass the frontiers of what I believed was possible. I could not have imagined having a better advisor and mentor for my PhD. Furthermore, I appreciate his focus on actual results as opposed to proxy measures such as time spent at the desk. Thus, I could explore the beauty of Grenoble and its surrounding mountains while still finishing my PhD at a very good pace and participating in projects with publications in major journals. As an important part of my experience at Institut Néel as a young researcher, many friendships and collaborations were forged. They are too numerous to list them all, but I want to specially mention: the AsGaSi team Everton Arrighi, Giorgos Georgiou, Matias Urdampilleta, Shintaro Takada, Tristan Meunier, Hermann Edlbauer, Bernhard Klemt, David Niegemann, Cameron Spence, Emanuel Chanrion, Baptiste Jadot, Junliang Wang, Pierre-André Mortemousque, Julien Paparone, Vivien Thiney, Yannis Zancanaro, Colin Scarato, Martin Nurizzo, Clément Geffroy, including all students, collaborators and involved permanents; the CQ team, the Electronics Workshop(s), the micro-mechanical Workshop, the Nanofab Team, the Calorimétrie team and the Carac team for their technical support, fruitful discussions, helpful advises and for good times in refreshing breaks.

*To my family*

# RÉSUMÉ

Synchronisation ultra-rapide, mise en forme d'impulsions et commutation efficace sont au cœur des mesures précises. L'objectif de ce projet de thèse est d'apporter le contrôle électronique ultra-rapide aux circuits nanométriques refroidis à des températures de l'ordre du mK. L'opération quantique rapide rapprochera le domaine de l'optique électronique quantique de son homologue photonique avec des applications pour un contrôle électronique rapide et efficace des dispositifs quantiques. Les dispositifs expérimentaux développés au cours de ce projet de thèse sont décrits et testés de manière à esquisser également les possibilités d'intégration dans les technologies quantiques. Dans un premier temps, une impulsion de tension de forme lorentzienne $\Gamma = (76 \pm 2)$ ps est mesurée de manière résolue dans le domaine temporel à des températures cryogéniques. Ensuite, les dérives de phase et d'amplitude sont analysées et optimisé avec le spectre de bruit. Un nouveau dispositif de génération d'impulsions utilisant un générateur de peigne est ensuite décrit et testé. Enfin, un futur réalisation d'une expérience d'interférence quantique par manipulation et détection dans un conducteur quantique est décrite, de même que les défis posés pour les dispositives quantiques à basse température et ses interconnexions.

*"Die Gedanken sind frei - Thoughts are free."*
old German student song

– Sophie Scholl

# 1

# INTRODUCTION AND MOTIVATION

## 1.1 A NEW ERA OF TECHNOLOGY POWERED BY APPLIED QUANTUM SCIENCE

Testing new ideas and discovering new technology is fundamental for improving society. The process of questioning and discovering is a key part of innovative research or applied science. A scientific discipline is said to be interesting because it is hard to understand from a theoretical point of view and even more challenging to show experimentally. Quantum science is such a fascinating discipline of research, which should not only be seen as difficult per se, but can be seen as rewarding since it provides a lot of room for creative innovation. In this broad field, the discrete, quantized nature of a physical property such as energy or matter determines the overall behavior of a studied process. At the beginning of the $20^{th}$-century quantum science focused on developing and testing the novel quantum theory. Brilliant minds like Albert Einstein, Marie Curie, Niels Bohr, Max Planck and many others discussed vividly at the Solvay conference in 1927 about "electrons and photons" and the fundamentally new understanding of wave-like particle behavior and quantization. This time where the foundations of quantum mechanics were laid is often named the first quantum revolution. Nowadays, experimental results have verified a big part of the first quantum theories and the quantum approach of describing nature is well-accepted. A big part of quantum science could consequently develop more towards applied quantum-enabled technologies. Advanced technology is reaching fundamental limits[93,118] where controlling quantum processes at very low temperatures, high resolution, and at small nano-metric length scales becomes essential. The enforced quantum functionality beyond the limits of classical physics initiates a new era of technology called the second quantum revolution[52].

Some famous examples of enforced quantum functionality are coherent lasers for spectroscopy and fast data communication, nuclear magnetic resonance for sensing and imaging, atomic clocks for precision timing, quantum hall channels defining a resistance standard, superconducting Josephson effect devices for precise flux control forming also a voltage standard and tunneling in transistor devices. The quest goes on empowered by the scientific developments mentioned above to connect analog quantum operation to the digital world. More precisely, analog quantum control optimizes minimum noise analog signals for primitive gate operations on physical quantum bit states opening up the field of digital, logic-gate based quantum computing[72]. A lot of industrial and scientific effort concentrates currently in the area of quantum computing, where quantum states are manipulated in a coherent way to perform circuit logic on quantum bit states. A quantum system's state is considered as coherent, if the total state of the system can be described by a series of complex numbers, one for each state of the system. A routine part of an algorithm that benefits from a quantum coherent approach of simulation is for instance a Fourier transformation. The Fourier transform naturally exists in quantum systems due to the complementarity of time and energy. The control of a linearly increasing number $n$ of entangled quantum bit states provides an exponentially increasing resource $2^n$ for parallel calculations and quantum simulations. It is important to note that quantum control has classical speed limits in contrast to some German highways. Sequential quantum operations can not be exponentially faster in the time domain as the following shows.

## 1.2 SPEED LIMITS FOR QUANTUM OPERATIONS

The speed limit of quantum operations and transfer of quantum bits scales with the inverse of the relevant energy scales and the group velocity. A speed limit for state rotation known as Mandelstamm-Tamm bound can be derived from the time-energy uncertainty principle[130]:

$$\tau \geq \frac{\pi\hbar}{2\Delta E}, \tag{1.1}$$

where $\Delta E$ is the energy variance related to the Hamiltonian. Similarly, the minimum two-qubit gate time[5] scales with the inter-qubit coupling strength J $T_{CNOTmin} \geq \pi/J$. Transfer of qubit chains such as moving ion or spin chains is limited by their maximum group velocity for adiabatic transport[109,152]. The pulse control times in the experiments presented afterwards are in the picosecond range. Currently, ultra-fast control pulses are orders of magnitude too fast compared to current maximum gate speeds in experiments with ions (µs) and superconducting or spin systems (ns). The maximum speed of operation is inversely proportional to the maximum driving frequency set by the coupling strength, which is possible within the rotating control frame. To first order, the speed of operation is limited by the inverse relevant coupling energy $g$ in a resonator atom model.

As the basic building blocks of today's computers also did not start off with ultra-fast operation speeds there is still room for speeding up quantum device operation. Moreover, the main advantages of using quantum operations are more on the efficiency side and the possible operation of many states in parallel. There is a class of problems which can be most efficiently or even solely simulated using quantum algorithms[141]. These problems strongly profit from a quantum approach for computing and simulation. The quantum speed-up for specific important algorithms can theoretically be exponential[22]. Despite great advances for instance recently on the Google AI Quantum processor and future hopes, hardware challenges to be able to run deep quantum gate circuits needed for these algorithms are still considerable[72]. A quantum advantage for specific problems in computing compared to classical, high performance computing remains a moving target also due to recent advances in classical simulations[37,119] and quantum-enspired, improved classical algorithms[162]. Predicting the exact date when there will be a useful quantum computer with commercial profit is not as important as developing ever improved quantum control and finding a technological quantum advantage not only for computing along the way.

One of the biggest challenges for coherent quantum control and systems engineering in solid-state quantum technology is the transfer of existing large bench-top approaches to small, embedded, on-chip devices. Solid-state quantum devices are often developed hands-on and tested at low cryogenic temperatures as portrayed in figure 1.1. Thus, the following also focuses on quantum-electronic engineering for integrated, on-chip devices. I then test, built and apply all introduced methods and measurement setups (in chapters 3-6) . The main topic of this experimental study is the control and time-resolved measurements of the electronic wave function in a nano-metric quantum conductor at cryogenic temperatures. I introduce subsequently the outline of the thesis and how electronic quantum control is investigated in this thesis.

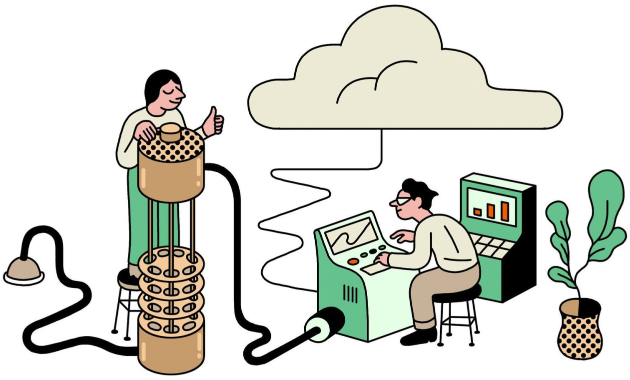

**Figure 1.1. | Quantum cloud services and the lab.** Researchers working on a cryogenic measurement setup for developing hardware for future applications in solid-state quantum technology. Artwork reprinted with permission from Simon Landrein [104].

## 1.3 ELECTRONIC QUANTUM CONTROL AND COHERENCE

Charge interactions and noise for instance introduced by insufficiently filtered coupling to the environment limit coherent quantum operation. Voltage controlled spin qubits are limited by the charge decoherence rate[149,185] and the need for high stability, low noise and well-defined fast control pulses[73,183]. High-frequency and minimum-noise electronic control in close-by conductors is crucial for fast and efficient quantum operations and read-out. Fast minimum-noise electronic control is to this end optimized on-chip and at low temperatures. Coherence also means that the relative phases of the states are experimentally accessible for instance in an interference experiment. A possible way to probe charge coherence of an electronic wave package is the injection of a very sharp (full width half maximum around 70 ps) voltage pulse into a two-path interferometer. The aim of the thesis is to investigate the propagation of an electron wavepaket inside a quantum conductor. Therefore, I outline the thesis contents in the following way: the theoretical background for quantum-electronic optics in solid-state devices is shortly outlined in the following chapter 2. The semiconductor heterostructures are introduced which I used for the experiments. Then, I outline how confinement and dimensionality leads to different physics, energy dispersions and transport behavior. The starting point for my quantum transport recapitulation is an electronic waveguide with Landau-Büttiker transmission modes at a quantum point contact constriction. Subsequently, I describe electronic wavefunction of single charge sources such as the Leviton wavefunction probed later on experimentally. In the next chapter 3, I portray the design guidelines used for the samples operated at high frequencies (several tens of gigahertz) and low temperatures (20 mK). After introducing the high mobility heterostructures, I then describe electrostatic simulations and waveguide calculations to bring ultra-fast pulses down to nano-meter scales at cryogenic temperatures. In chapter 4, I describe signal recovery and noise. Then, the introduced noise characterization methods are applied to install and test a low noise amplification setup at cryogenic temperatures. After having characterized the low frequency parts and the long-term stability of the setup, I go on to the high frequency pulse control in chapter 5. I describe and built coaxial lines, the sample holder with a new radio frequency (RF) printed circuit board (PCB). A tapered coplanar waveguide is then used to measure the transmission down to the sample chip. In the following, I introduce sampling at a quantum point contact and sample a Lorentzian pulse train, which is the basis wave function for Levitons. After discussing the limits of the first version of the pulse control setup to produce the Lorentzian pulses, I built up a phase locked clock generator setup to improve the drift stability and synchronize the source sine waves. In order to produce even smaller wave packet widths, I introduce a microwave comb generator setup in chapter 6. Therein, I describe Fourier synthesis of a Lorentzian pulse train. Then, the analysis of the time-domain shape of a pulse train derived from a comb generator spectrum follows. I describe the blueprint of the comb generator setup and measure the comb generator output at different frequencies. The last chapter 7 finally summarizes the current status of the project with a short outlook and possible roads towards further development of electronic quantum control. Additional material for setup engineering and development of the shown measurement methods, important material and supplementary information is summarized in the appendix A. In the following chapter, I review the solid-state physics background for semiconductor quantum electronics and microwave propagation.

*“If you’re not having fun, you’re not learning.*
*There’s a pleasure in finding things out.“*

– Richard Feynman

# 2

# FROM SOLID-STATE ELECTRONICS TOWARDS QUANTUM-ELECTRONIC OPTICS

This chapter provides a snapshot-like introduction to the most relevant solid-state physics background[29] and to electronic wave functions. Therein, I outline only the most important concepts of solid-state physics[70] to provide an understandable background for my thesis project. Solid-state electronic devices enabled by semiconductor technology are the workhorses of the 21st century’s digital evolution. Semiconductors provide the material property of being switchable between two digit states, a conducting one, and an insulating zero state, by definition. The tunable behavior of charge carrier transport and recombination is the physical hardware basis for registers, logic, amplification, emission, detection, feedback and control. Trillions of semiconductor devices are produced every year for today’s modern logic circuitry, electronics, optics and also sensors. More than 50 years ago Gordon E. Moore, co-founder of Intel and then research director at Fairchild Semiconductor, predicted that the number of transistors placed in an integrated circuit would approximately double every two years.

The extrapolated trend for minimizing transistor sizes known as Moore's law slowly comes to a natural halt with semiconductor industry attempting the 7 nm node and below. Minimizing semiconductor component sizes ultimately leads to quantum confinement, which prohibits a flow of electrons in a classical way. Research on solid-state quantum devices is therefore a logical step to advance modern technology beyond its current limits[175].

## 2.1 ELECTRONIC BAND STRUCTURE AND DENSITY OF STATES

The *"electronic world map"* (Herbert Kroemer[100]) or the key characteristics of a solid-state device is the band structure. The **band structure** gives:

*A dispersion relation* $E(\mathbf{k})$ *of possible carrier occupation in an energy region depending on the carrier's momentum given by the wave vector* $\mathbf{k}$.

Charge carriers can be confined in different directions using barriers as for instance electric field barriers defined by gate voltages or piezoelectric potentials. The effects of quantum confinement arise when one or more boundary dimensions become comparable to the de Broglie wavelength $\lambda$ of the charge carrier's wave function and consequently energy levels become discrete or quantized:

$$L \approx \lambda = \frac{h}{|\mathbf{p}|}. \tag{2.1}$$

The reduced dimensionality gives rise to different transport and (electron-hole) recombination behavior for sheets, wires and dots compared to bulk materials[41,45]. Figure 2.1 shows the density of states $D(E)$ for materials with reduced dimensionality. The density of states $D(E)$ is the number of available electronic energy levels within the energy

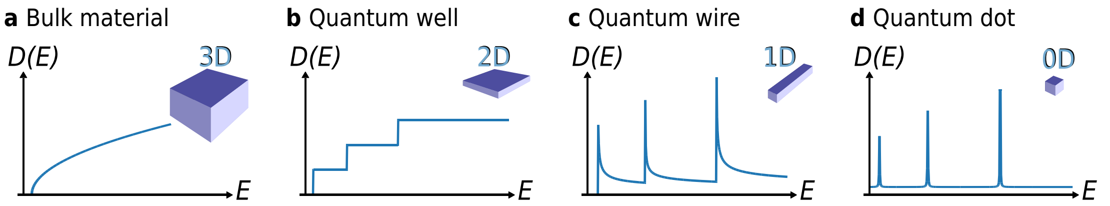

**Figure 2.1. | Density of states for low dimensional quantum materials. a**, Three-dimensional (3D) bulk material unconfined. **b**, Two-dimensional (2D) quantum well layer of charge carriers quantum confined in one direction, for instance in the growth direction for an AlGaAs heterostructure. **c**, One-dimensional (1D) quantum wire displacement of carriers is only likely in one direction for instance in a nano wire. **d**, Zero-dimensional or point-like (0D) quantum dot quantum confined particles in a box.

range $E + \Delta E$ and per integrated confined k-space volume $V_{confinement} = \Delta k^d = \left(\frac{2\pi}{L}\right)^d$ in $d$ dimensions:

$$D(E) = \int_{\mathbf{R}^d} \frac{d^d k}{(2\pi)^d} \cdot \delta\left(E - E(\mathbf{k})\right) \tag{2.2}$$

Using the energy-momentum relation

$$E = \frac{p^2}{2m} = \frac{\hbar^2 k^2}{2m^*} \tag{2.3}$$

$$\frac{dk}{dE} = \frac{m^*}{\hbar^2 k},$$

with the effective mass $m^*$ leads to the density of states of low dimensional semiconductors shown in table 2.1. The effective mass tensor can be derived from a parabolic (second-order Taylor) expansion of the band $\epsilon_n$ at the minimum:

$$\epsilon_n(\mathbf{k} + \mathbf{q}) = \epsilon_n(\mathbf{k}) + \frac{1}{2}\Sigma_{ij}\frac{\delta^2 \epsilon_n}{\delta k_i \delta k_j} q_i q_j + \mathcal{O}(q^3) \tag{2.4}$$

$$\frac{\hbar^2}{2m^*_{ij}} = \frac{1}{2}\frac{\delta^2 \epsilon_n}{\delta k_i \delta k_j} \tag{2.5}$$

This means that the curvature of the band $\epsilon_n$ is inversely proportional to the mass of the regarded charge transport band. In this way, the effective mass tensor relates the inertial motion in a band to the motion of a free electron $\epsilon_0$ in vacuum with the

| Dimensionality d | 3D | 2D | 1D | 0D |
|---|---|---|---|---|
| $k$ volume | $\left(\frac{2\pi}{L}\right)^3$ | $\left(\frac{2\pi}{L}\right)^2$ | $\frac{2\pi}{L}$ | point-like |
| $D_d(k)/g$ | $\frac{k^2}{2\pi^2}$ | $\frac{k}{2\pi}$ | $\frac{1}{2\pi}$ | $\propto \delta(\mathbf{k} - \mathbf{k_C})$ |
| $D_d(E)/g$ | $\frac{(2m^*)^{3/2}}{4\pi^2\hbar^3}\sqrt{E - E_C}$ | $\frac{m^*}{2\pi\hbar^2}\sigma(E - E_C)$ | $\frac{1}{2\pi\hbar}\sqrt{\frac{m^*}{2(E-E_C)}}$ | $\propto \delta(E - E_C)$ |

**Table 2.1. | Density of states and dimensionality.** Mathematical summary of the available number of energy levels per unit k-volume in different confined dimensions, $E_C$ is the bottom of the regarded charge band, $m^*$ is the respective effective mass tensor in the equation of motion compared to the electron mass $m_e$ in vacuum. Moreover, the spin and valley degeneracy factor $g$ can also influence this density and the band structure.

electron mass $m_e$. The dimensionality of charge motion can be designed from bulk semiconductors (3D), over two-dimensional (2D) quantum wells and one-dimensional (1D) quantum wires to zero-dimensional (0D) confined states in all directions, so called quantum dots[16,24,79]. An overview of the cases above is given in the following. Bulk semiconductors can form when the crystal's periodicity leads to a periodic potential $V(\mathbf{r}) = V(\mathbf{r} + \mathbf{R})$ and therefore gives rise to the formation of bands allowing charge carrier occupation. The Fourier expansion (in $\mathbf{k}$-space) of this potential can be inserted in Schrödinger's equation[79]:

$$\left[-\frac{\hbar^2}{2m_e}\Delta + \Sigma_{\mathbf{G}} V_{\mathbf{G}} \mathrm{e}^{i\mathbf{G}\cdot\mathbf{r}}\right]\Psi(\mathbf{r}) = E\Psi(\mathbf{r}), \tag{2.6}$$

with the lattice periodicity condition for the reciprocal lattice vector $\mathbf{G}$ and for the real space lattice repetition vector $\mathbf{R}$ given as:

$$\mathbf{G}\cdot\mathbf{R} = 2\pi n. \tag{2.7}$$

A plane electronic wave in such a periodic crystal lattice can be written as:

$$\Psi_{\mathbf{k}}(\mathbf{r}) = e^{i\mathbf{kr}} \cdot u_{n\mathbf{k}}(\mathbf{r}), \tag{2.8}$$

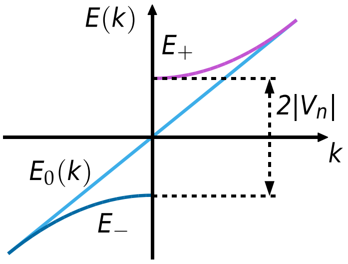

**Figure 2.2. | Energy level splitting in a band diagram or dispersion relation.** The light blue line $E_0(k) \propto v_g \cdot k$ represents the linear dispersion with slope $v_g$ of a free electron model as it can be seen for a Dirac fermion, the split bands $E_+$ and $E_-$ correspond to a free electron moving in a periodic potential or perturbation $V_n$ leading to a splitting of the Energy states.

which is known as Bloch's theorem. The Bloch function $u_{n\mathbf{k}}(\mathbf{r})$ contains the periodicity of the crystal lattice via:

$$u_{n\mathbf{k}}(\mathbf{r}) = u_{n\mathbf{k}}(\mathbf{r} + \mathbf{R}), \tag{2.9}$$

where $n$ is the index of the regarded band. More general wave functions $\mathbf{\Psi}(\mathbf{r})$ are often described in terms of Bloch functions $u_{n,\Gamma}(\mathbf{r})$ using the envelope function or $\mathbf{k} \cdot \mathbf{p}$ theory[45]:

$$\mathbf{\Psi}(\mathbf{r}) = \sum_n \Psi_n(\mathbf{r}) u_{n,\Gamma}(\mathbf{r}), \tag{2.10}$$

where $\Psi_n(\mathbf{r})$ is a slowly varying envelope function, a generalized form of the plane wave approach in equation 2.8 and $u_{n,\Gamma}(\mathbf{r})$ is the periodic Bloch function evaluated at the $\Gamma$ point $\mathbf{k} = 0$.

The periodic crystal potential also leads to a splitting of the energy eigenstates or an energy band gap for a semiconductor at $\mathbf{k} \approx -1/2\mathbf{G}$, which is also called Peierl's transition[95]. This splitting is a direct consequence of the interference of the incoming wave function with a wave function reflected by the periodic potential perturbation. The energy gap consequently appears when going from a free electron model to a nearly free electron model with a space-periodic perturbation $V(\mathbf{r}) = V(\mathbf{r} + \mathbf{R})$. An energy gap (or forbidden energy bands) in the dispersion relation $E(k)$ is quite characteristic for a periodic reflecting potential as it can be seen also for plane light waves under Bragg reflection. Therefore, a periodic reflecting potential, also called Bragg reflector, is commonly used for microwave or photonic band engineering. Photonic band gap engineering is important for designing chips and transmission lines adapted for high frequencies as for instance at the 50 GHz switch design (cf. 5.23).

An avoided level crossing or quantum resonance of two Energy levels $E_1$ and $E_2$ can be described by a two-state Hamiltonian Hamiltonian operator ($H$) with an off-diagonal perturbation $P$:

$$H' = H + P = \begin{pmatrix} E_1 & 0 \\ 0 & E_2 \end{pmatrix} + \begin{pmatrix} 0 & V_n \\ V_n^* & 0 \end{pmatrix} \tag{2.11}$$

leading to the new energy eigenvalues of the upper $E_+$ and lower $E_-$ state:

$$E_\pm = \frac{1}{2}(E_1 + E_2) \pm \frac{1}{2}\sqrt{(E_1 - E_2)^2 + 4|V_n|^2} \tag{2.12}$$

The real band gap values and semiconductor band structure can be approximated using a periodic atomic orbital background for instance with a tight-binding model[26,172]. In a 4x4 $\mathbf{k} \cdot \mathbf{p}$ theory model, the different energy bands would, for instance, correspond to $n = e, hh, lh, so$ the electron, heavy hole, light hole and spin-orbit band respectively[108,113]. These different energy bands close to the band extrema (at the $\Gamma$ point) are also illustrated in the band structure scheme of a direct band gap semiconductor like gallium arsenide (GaAs)[80] in figure 2.3a.

An energy transition in the band structure occurs if different semiconductor materials are stacked on top of each other. Controlled layer stacking defined for example by semiconductor heterostructure growth is the basis for designing a band structure. The material stacking can lead to a lattice mismatch and defects in the atomic layer grid. Figure 2.3b shows the material engineering guidelines for semiconductor heterostructure growth. It relates the energy gap to the lattice constant. The materials used in this thesis project for high-speed two-dimensional semiconductor heterostructures (HEMTs) are highlighted in blue[100].

Using aluminium arsenide (AlAs)[81] and GaAs as primary elements for the heterostructure growth leads to very high quality atomically smooth interfaces since there is no lattice mismatch between AlAs and GaAs. The sharp interfaces are the material basis for tight confinement along the growth direction and quantum transport.

## 2.2 QUANTUM TRANSPORT AND ELECTRON OPTICS

If carriers are confined in a two-dimensional sheet the corresponding physics is described by a two-dimensional electron gas (2DEG). 2DEGs in quantum wells can be built by having a material like GaAs sandwiched between two layers of a material with a wider band gap, like AlAs. Important device parameters of the 2DEG used during the measurements are summarized in table 2.2. Another similar example for a 2DEG in a layered material heterostructure would be graphene sandwiched in boron nitride. Charge carriers in 2DEGs can be described by approximating the potential at the interface by an infinite square well or triangular well and solving the Schrödinger equation analytically[178]. Numerical approaches are used if the full material stacking of a high-electron-mobility transistor (HEMT) including the metal Schottky barrier, the modulation doping and the (triangular) well potential is taken into account. The material stacking of a HEMT and the resulting band structure are shown in figure 2.3d and 2.3c. The numerical simulation software nextnano[26] can be used to calculate the band structure of the 2DEG[176] in a high mobility device similar to the band structure scheme in figure 2.3c. A numerical simulation software can also be used as a tool for designing HEMTs and modulation-doped semiconductor heterostructures.

A lot of high-frequency 5G and radar technology is powered up by fast transistors, since HEMTs are very important active elements in millimetre integrated cir-

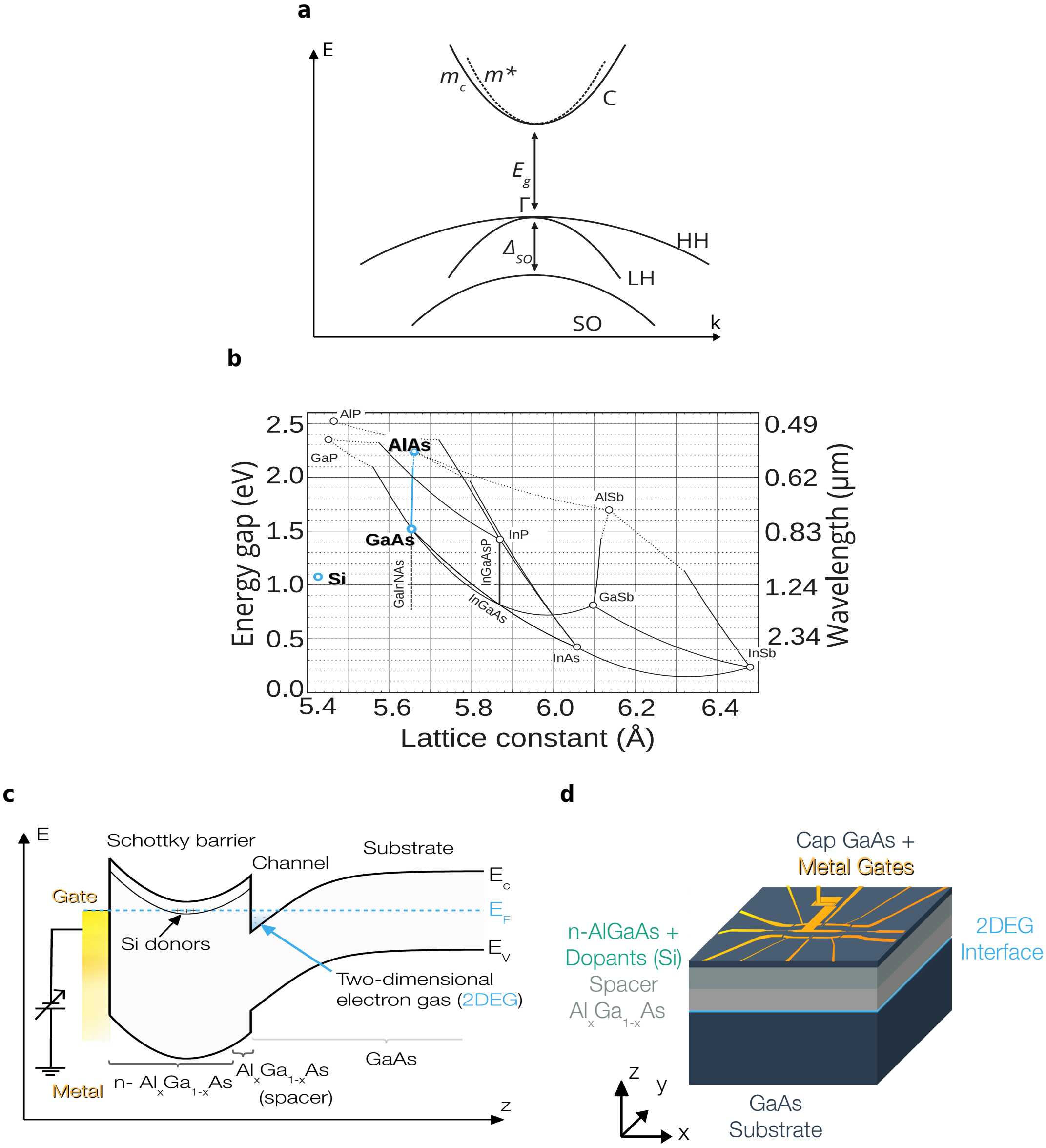

**Figure 2.3. | Semiconductors and high electron mobility devices. a**, Band structure of a direct band gap semiconductor. Conduction band *C* with an approximated effective mass $m^*$, energy gap $E_g$ at the $\Gamma$ point, valence band split into heavy hole *HH*, light hole *LH* and spin-orbit band *SO* band. **b**, Band gap energy to lattice constant relation of semiconductor compounds at $T = 0K$. Highlighted in blue materials relevant for high electron mobility wafer growth. Reprinted figure with permission from [100]. Copyright (2001) by the American Physical Society. **c**, Schematic of the band structure of a high electron mobility device. Energy levels [176] for the material stacking in *z*-direction are schematically depicted. **d**, Scheme of the layer stacking of a high electron mobility device in a semiconductor heterostructure.

| Device parameter | Formula | Value |
|---|---|---|
| Fermi energy | $E_F = \frac{\hbar^2 k_F^2}{2m^*}$ | $7.5\,\mathrm{meV}$ |
| Fermi wave vector | $k_F = \sqrt{2\pi n_S}$ | $11.5 \times 10^7\,\mathrm{m}$ |
| Effective mass | $1/m^* \propto \frac{\mathrm{d}^2E}{\mathrm{d}^2k}$ (2.5) | $m^*_{GaAs} = 0.067 m_e$ |
| Fermi velocity | $v_F = \frac{\hbar k_F}{2m^*}$ | $100\,\mathrm{km\,s^{-1}}$ |
| Fermi wavelength | $\lambda_F = \sqrt{\frac{2\pi}{n_S}}$ | $55\,\mathrm{nm}$ |
| Mean free path | $l_{el} = \frac{\mu_S m^* v_F}{e}$ | $7\,\mathrm{\mu m}$ |
| Collision time | $\tau_{el} = \frac{l_{el}}{v_F}$ | $72\,\mathrm{ps}$ |
| Fermi temperature | $T_F = \frac{E_F}{k_B}$ | $87\,\mathrm{K}$ |
| Sheet resistance per square | $R_s = \frac{1}{e n_S \mu_S}$ | $16\,\Omega$ |
| Carrier density | $n_S$ | $2.11 \times 10^{11}\,\mathrm{cm^{-2}}$ |
| Mobility | $\mu_S$ | $1.89 \times 10^6\,\mathrm{cm^2\,V^{-1}\,s^{-1}}$ |

**Table 2.2. | HEMT device parameters.** Energy, length scales and other device parameters of the 2DEG inside the high mobility wafer at 4 K used for time-resolved measurements.

cuits. High electron mobility structures can reach mobilities up to $32 \times 10^6$ V/s at low temperatures[102]. HEMT devices have therefore also been long time prime candidates for testing high-speed electronics and improving and investigating fundamental electronic quantum transport[97]. A charge motion can then further be confined by growth or electrostatic confinement using for instance depletion gates. A quantum wire with length $L$ along the x-direction is described by a quantum equation of motion when scattering with impurities can be neglected[16]:

$$L < l, \tag{2.13}$$

where $l$ is the mean free path between scattering events. This regime where scattering can be neglected is called the ballistic transport regime. If coherent propagation can additionally be ensured and optics-like experiments can be performed, the regime is named **electron optics regime**[14,31]. The one-dimensional wire in the electron optics case can be treated as an electronic wave guide. Similarly, fast control of few-electron pulses can be effectively described in a wave-like optical manner. The Schrödinger equation of an electronic wave guide with transport along x direction reads as[106]:

$$\left[-\frac{\hbar^2}{2m}(\delta_y^2+\delta_z^2)+V(y,z)\right]\mathbf{\Psi}=E\mathbf{\Psi} \tag{2.14}$$

where $V(y,z)$ is the wire's confinement potential in y and z direction, for instance given by depletion gates forming the waveguide in y and the 2DEG in z-direction. A slowly varying confinement potential $V(y,z)$ defined at the quantum wire cross section leads to a wave propagation in x direction with a wave function:

$$\mathbf{\Psi}(x,y,z)=\chi(y,z)\mathrm{e}^{ikx}, \tag{2.15}$$

where $\chi(y,z)$ are normalized envelope wave functions originating from the confinement potential. The general solution of the electronic waveguide is then given as a sum of the mode functions[106]:

$$|n,k\rangle=\sum_n c_n\chi_n(y,z)\mathrm{e}^{ik_nx}, \tag{2.16}$$

where $n$ labels the mode of energy $E_n(k)$, $k_n=\sqrt{2m(E-E_n)}/\hbar$ is the wave vector and $c_n$ are constants. The wave vector $k_n$ gives the dispersion or energy dependence of the $n$th mode. Modes with energy $E<E_n$ decay exponentially $\mathrm{e}^{-\alpha_nx}$ at the rate $\alpha_n=\sqrt{2m(E_n-E)}/\hbar$. The different modes $n,m$ of the electronic waveguide sum up to a measurable electrical conductance $G$ described by Landauer-Büttiker scattering formalism:

$$G=G_0\sum_{n,m}T_{nm}, \tag{2.17}$$

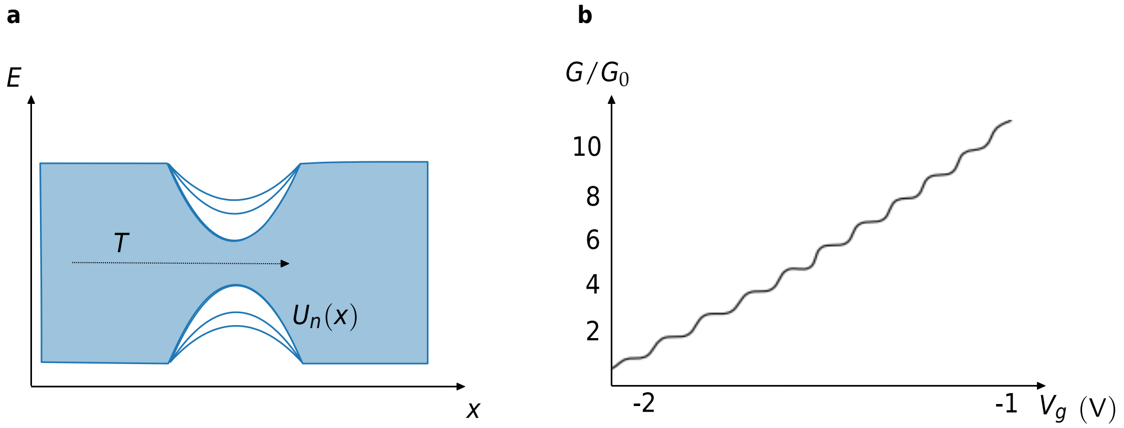

**Figure 2.4. | Quantum Point Contact. a**, Quantum point contact constriction. Potential pinching off a transmission channel in a clean conducting region like a two-dimensional electron gas. Quadratic confinement potential $U_n(x)$ leads to step-wise selected transmission $T$ and quantum tunneling. **b**, Measured conductance plateaus at a quantum point contact. The constriction is opened by applying a less negative depletion gate voltage $V_g$ and quantized conductance steps can be observed experimentally in transmission. Reprinted figure with permission from [168]. Copyright (1988) by the American Physical Society.

with the corresponding transmission probabilites $T_{nm}$ from $n$ to $m$, where $G_0 = \frac{2e^2}{h}$ is the conductance quantum. Electronic transmission is frequently written in scattering matrix form to describe more general transport problems.

A constriction between two conductors is called quantum point contact, if the constriction is so small that only a few electron wavelengths can fit in. Such a constriction can be formed by setting a negative voltage on two depletion gates on top of a two-dimensional electron gas. The depletion gates with a tip to tip distance of the order of 300 nm can then step-wise pinch off the conducting channels.

## 2.3 QUANTUM POINT CONTACT

The quantum point contact acts similar to a tunable slit or filter for the transmission modes of the electron wave guide. The quantum point contact can be tuned to conduct stepwise smoothed due to quantum tunneling as shown in figure 2.4a. The smooth

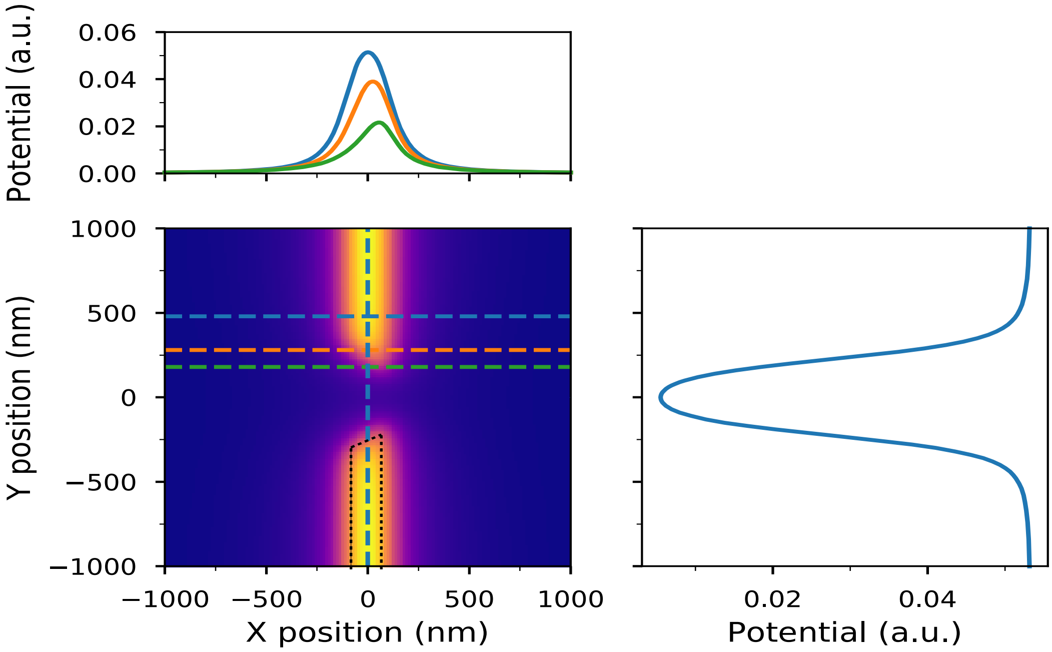

**Figure 2.5. | Simulated potential of the gates of the QPC.** Poisson potential simulation of the gate configuration used in [168] using a numerical Poisson solver [71]. The gate geometry is indicated as black dashed line. The dimensions correspond to a gate width of $w = 200$ nm and tip to tip distance $d = 250$ nm. The horizontal cuts through the potential in y-direction in the top part can be described by a quadratic tunneling potential.

steps can then be described by a transmission probability to cross the potential even if the energy to classically pass the barrier is not enough. The tunneling through an inverted quadratic confinement potential can be described by the following transmission function[35,92]:

$$T_n(E) = \frac{1}{e^{2\pi(E_n - E)/\hbar\Omega_n} + 1}, \tag{2.18}$$

where $\Omega_n$ is defined by the geometry:

$$\Omega_n = \frac{\hbar \pi n}{mWL}, \tag{2.19}$$

with a width $W$ and a length $L$, of the confinement potential $U_n(x)$:

$$U_n(x) = E_n - \frac{m}{2}\Omega_n^2 x^2 \tag{2.20}$$

the electron mass $m = m_e$ and $E_n$ is the Eigenenergy offset of the corresponding transmission mode step $n$

$$E_n = \frac{\hbar^2 \pi^2 n^2}{2mW^2} \tag{2.21}$$

Figure 2.5 shows then how Schottky depletion gates define a quadratic transmission potential at the 2DEG layer. I use a numerical electrostatic Poisson solver[71] to simulate the electrostatic potential environment starting from the meshed gate configuration (here a QPC). The different line cuts show then how the point contact is formed. Quantum point contacts are very sensitive to impurities. The high sensitivity makes them applicable for sensing impurities or spin fluctuations in their microscopic vicinity[13]. Rapidly operable quantum point contacts are to this end also used to read out the configuration of a close-by spin memory[136]. A network of quantum point contact (QPC) switches routing pulses can additionally be used to create fast, low-noise and power-efficient time-domain multiplexers at mK temperatures[18]. A charge wave function can be quantum-confined in all directions forming quantum dots. A quantum dot can be described as a point-like quantum-confined box for charge carriers leading to discrete energy levels similar to an atom is called quantum dot. The energy levels of a quantum dot are discrete if the confinement potential is static and the charges are isolated from the reservoirs. In the static case, the occupation of a quantum dot can be approximated well by a particle in a box model. Quantum dot energy levels can be occupied by charge carriers. The charge's spin vector pointing up $|\Uparrow\rangle$ or down $|\Downarrow\rangle$ can be used to form the basis states of a memory for quantum computing (cf. A.8).

During this thesis project, we investigate minimum-noise, fast and effective electronic control, static long-term stability, and a quantum conductor which could be applied as a fast bus line to exchange and reset information using single electrons. Strong interaction with the environment leads to a rapid vanishing of the complex amplitudes and a so-called collapse of the wave function to a probabilistic value. Small interactions with the environment cause a well-isolated quantum state to slowly decohere. Therefore, a time-resolved probe of electronic coherence using single electron wave packets will be a very important tool for designing and testing quantum hardware. Optical coherence is probed in quantum optics by measuring Glauber's correlation function at output detectors after an exchange interaction at a beam splitter[68]. Similarly, Glauber's correlation function can also be mapped to electronic wave packages in the ballistic regime[69]. The following describes the electronic wave function forming the basis for fast quantum control in an electronic wave guide.

## 2.4 ELECTRONIC WAVE FUNCTION - THE WIGNER FUNCTION

The electronic wave function has different contributions. A stationary one given by the presence of an equilibrium carrier distribution in a solid-state matrix. This equilibrium carrier distribution is also known as the Fermi sea. Injection and recombination of charge carriers lead to an excess carrier distribution relative to the Fermi sea. The many-body state of the Fermi sea is normally described starting from it's equilibrium state:

$$\rho = \mathrm{e}^{-\beta H}/Z, \tag{2.22}$$

with $Z$ being the partition function. In the frequency domain, the equilibrium state is then a superposition of many modes centered at energy $\hbar\omega$ populated with a probability:

$$f_{e,T_{el}}(\omega) = \frac{1}{\mathrm{e}^{(\hbar\omega-\mu)/k_B T_{el}} + 1}, \tag{2.23}$$

with the electronic temperature $T_{el}$ and the global potential shift in energy given by the chemical potential $\mu$. $f_{e,T_{el}}(\omega)$ is known as the Fermi-Dirac distribution. Wave functions in quantum optics are often expressed as a Wigner probability distribution function in time and energy domain. Electron wave packages can in a similar way be described in a quantum-electronic optics manner[58]. The Wigner function of the Fermi sea $\mathcal{W}^{(e)}$ is given as a time-stationary electronic distribution function:

$$\mathcal{W}^{(e)}_{\mu,T_{el}}(t,\omega) = f_{e,T_{el}}(\omega) := |F\rangle \tag{2.24}$$

The **equilibrium state** description **in quantum-electronic optics** is:

*An electronic solid-state device's ground state is the Fermi sea's Wigner probability distribution function* $|F\rangle$.

A direct electric current (DC) bias or classical voltage offset leads to a global shift of the chemical potential ($\mu \neq 0$) and therefore also an energy shift of the stationary Fermi sea Wigner function $\mathcal{W}^{(e)}_{\mu,T_{el}}$. In general, a classical voltage drive like for instance a DC voltage or a low frequency sine wave generates a stream of excess excitations consisting of electrons and holes. The number of excess excitations fluctuates. Arbitrary wave functions injected on top of the Fermi sea cannot be regarded as an efficient electron source with a very low excess noise. Investigating efficient single quantum charge sources for applications in quantum hardware is a very active research topic and described subsequently.

## 2.5 SINGLE QUANTUM CHARGE SOURCES

There are multiple ways to inject single charges into quantum conductors[14,158]. Quantum-electronic optics experiments made a fast development during the last decade due to the new experimental ways to isolate and transfer single electrons. Electronic analogues to Mach-Zehnder[83], Hanbury Brown-Twiss[126], Hong-Ou-Mandel[30] and quantum tomography of the electron wavefunction[54,87] are only a few selected highlights of the significant experimental advances. Single electron sources commonly used in solid-state quantum devices are the quantum confined turnstile[169], SAW assisted single electron injection[19] and Lorentzian shaped short voltage pulses so-called Levitons[107]. The injection of a Lorentzian-shaped, time-dependent voltage pulse forms a coherent electron state in an electronic wave guide:

$$V(t) = \frac{2\hbar}{e} \frac{\tau_e}{(t - t_0)^2 + \tau_e}, \tag{2.25}$$

where each pulse carries a flux quantum proportional to the time integral of the pulse:

$$\int V(t)dt = \frac{h}{e}. \tag{2.26}$$

The coherent electronic wave function above is also called Leviton[82,90,107]. The Leviton wave function has a Lorentzian form in time domain:

$$\Psi^{(e)}_{Levitov}(t) = \sqrt{\frac{\tau_e}{2\pi}} \frac{1}{t + i\tau_e} \tag{2.27}$$

and follows an decaying exponential in energy domain with $1 \geq k \geq n$ electrons[58]:

$$\Psi^{(e)}_{Levitov}(\omega) = \mathcal{N} \cdot \Theta(\omega) \mathrm{e}^{-\omega\tau_e} = \sqrt{2\tau_e} L_{k-1}(2\pi\tau_e) \cdot \Theta(\omega) \mathrm{e}^{-\omega\tau_e}, \tag{2.28}$$

where $\mathcal{N}$ is a prefactor depending on the electron number inside the pulse, $\tau_e$ is the time spread of the pulse, $L_k$ is the $k$th Laguerre polynomial and $\Theta(\omega)$ the Heaviside step function ensuring positive frequencies and by that the fermion character. Figure 2.6 shows the Wigner distribution function of the Landau and the Levitov electron source[36]. The Wigner function provides a framework to do an autopsy of quantum effects in a quantum-electronic measurement[27,146]. A good indicator for quantum be-

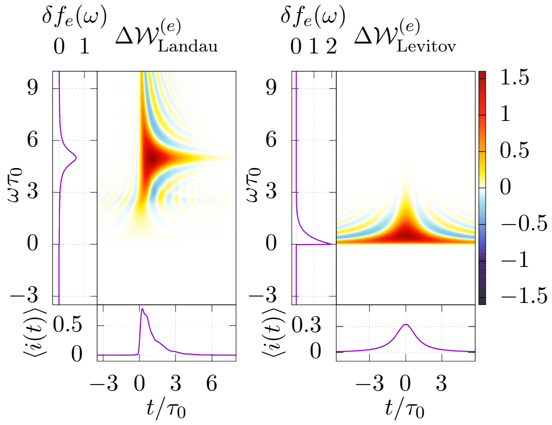

**Figure 2.6. | Wigner distribution function of single electron excitations.** Left side Landau excitation, right side Lorentzian Leviton excitation. Reprinted figure with permission from [36]. Copyright (2018) by the American Physical Society.

havior is for instance if interference terms lead to areas of negative probability in the Wigner distribution function as shown by the negative blue fringes in figure 2.6 due to destructive quantum interference. Also purely positive Wigner function states like Gaussian states[65] can show quantum behavior if they are in superposition or entangled. It is important in an experiment that the thermal energy or fast energy relaxation does not obscure completely interference, superposition and entanglement effects. A well isolated level configuration[111] for instance by level sensing at detuned positions can help to relax thermal low temperature requirements[182]. The read-out level scheme and therein the relevant line-widths and energy differences of transitions with respect to the solid state matrix bands like for instance the valence and conduction band define at which maximum temperature coherence can be probed. Levitons are directly injected on top of the thermal Fermi sea distribution. Therefore, the temperature of the experiment presented here should be low compared to the frequency of the investigated injection:

$$hf > k_B T_{el}, \tag{2.29}$$

where $T_{el}$ is a low electronic thermal state temperature and $f$ is the frequency of the injection. The relevant energies in the experiments range for instance from a "high" energy 100 µeV corresponding to a frequency of 24.18 GHz or an equivalent temperature of 1.16 K to a low energy 1 µeV respectively 241.8 MHz) or ≈ 12 mK. The energy condition above means in other words that the excess quantum electronic effect must be distinguishable from the Fermi sea ground state thermal contribution. Levitons in a quantum conductor at mK temperatures show quantum behavior on ultra-fast picosecond time scales and the Wigner function has been measured by photo-assisted shot-noise spectroscopy[54,87]. Moreover, a Josephson relation for the onset of the excess shot-noise at microwave frequencies (GHz) allows to experimentally analyze frequency-dependent noise signatures of complex topological electronic states such as recently measured with Fractional Quantum Hall states[89]. A setup developed for direct ultra-fast sampling inside a quantum conductor[147] which then allows to create a time lapse of an electronic pulse such as a Leviton at cryogenic temperatures is shown later in the experimental part. If a periodic sum of Lorentzian pulses where each pulse carries n electrons is injected, the electronic state is still a minimum noise coherent state[107] and the voltage sums up to:

$$V_n(t) = \frac{V_L}{\pi} \sum_{k=-\infty}^{+\infty} \frac{1}{1 + (t - kT)^2/\tau_e}, \tag{2.30}$$

with the time repetition period $T$ and the wave package time spread $2\tau_e = \Gamma$ related to $\Gamma$ the full width half maximum of the Lorentzian peak with amplitude $V_L$ in time domain. The analytical periodic expression for the Lorentzian voltage pulse train wave form is then[54]:

$$V_n(t) = \mathcal{N}_L \frac{\sinh(\omega\tau_e)}{\sinh(\omega/2\tau_e)^2 + \sin(\omega/2t)^2} \tag{2.31}$$

with the prefactor $\mathcal{N}_L = \frac{nhf}{e}$ and the number of electrons $n$ experimentally tunable by the voltage amplitude. The Fourier components of a periodic train of Lorentzian pulses are given by $\tilde{f}_{-1} = -\mathrm{e}^{-2\pi\tau_e/T}$, $\tilde{f}_n = \mathrm{e}^{-2\pi n\tau_e/T} - \mathrm{e}^{-2\pi(n+2)\tau_e/T}$ and otherwise $\tilde{f}_{n<-1} = 0$[171]. And the amplitude probabilities of the Fourier components as:

$$P_l = \left|\tilde{f}_l\right|^2 \tag{2.32}$$

The number of electron excitation per period is given as:

$$N_e = \sum_{l=1}^{+\infty} l P_l \tag{2.33}$$

and the hole contribution

$$N_h = \sum_{l=-\infty}^{-1} (-l) P_l \tag{2.34}$$

The number of excess electron hole pairs also called excess noise is given as:

$$\Delta N_{eh} = \sum_{l=-\infty}^{+\infty} |l+q| P_l - |q| \tag{2.35}$$

The excess number of electron hole pairs or excess noise is minimal (using the Fourier components of a Leviton pulse train above):

$$\Delta N_{eh} = 0 \quad \forall q = n \cdot e, \tag{2.36}$$

if the pulse train contains a sum of Lorentzian pulses of integer charge $q = n \cdot e$ per pulse.

The energy-equivalent of the time-resolved Leviton source is the quantum confined single electron turnstile. A turnstile source is given as a Landau energy-resolved electron excitation:

$$\psi^{(e)}_{Landau}(\omega) = \mathcal{N}_0 \frac{\Theta(\omega)}{\omega - \omega_e - i\gamma_e/2}, \tag{2.37}$$

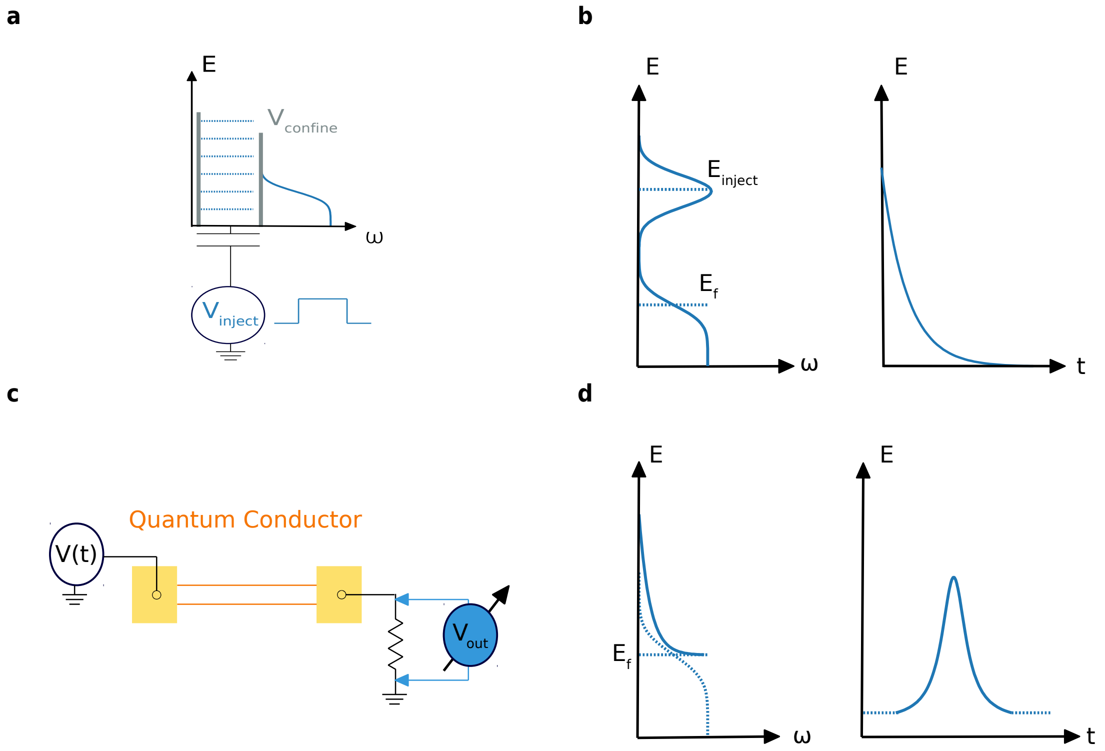

**Figure 2.7. | Single electron sources. a**, A fast pulse, opening the barrier gate releases a single electron excitation high above the Fermi sea level. **b**, Landau source: quantum confined, energy-resolved turnstile. **c**, A fast Lorentzian voltage pulse is applied to the Ohmic contact (yellow squares) and therefore injected on top of the Fermi sea. **d**, Leviton source: Lorentzian time-resolved voltage pulses.

with the spectral width $\gamma_e$, decay time $\tau_e = 1/\gamma_e$ and the normalization

$$\mathcal{N}_0 = \sqrt{\frac{v_F \gamma_e}{\frac{1}{2} + \frac{1}{\pi} \arctan \frac{2\omega_e}{\gamma_e}}},$$

to ensure the absence of negative energies (Landau hole excitation). The Landau wave package can be decomposed as a superposition of weighted Leviton wave packages at different times[36]. The decomposition of an energy-resolved excitation in Leviton states exemplifies Levitons being minimum noise, coherent states of electric current. The quantum confined turnstile source depicted in figure 2.7 consists out of a charge island with charge levels separated by a Coulomb blockade barrier to the channel[59] for instance a quantum dot or a mesoscopic capacitor. A fast gate pulse changes the coulomb level to barrier energy detuning so that an electron can surpass the barrier potential. The fast pulse kicks out a single electron charge excitation above the Fermi sea[62]. Hereby, the barrier height defines the emission energy above the Fermi sea. A quantum confined turnstile source can produces a nicely energy resolved wave package.

Levitons provide favorable conditions for minimal noise excitation in quantum conductors and a well defined wave function in the time domain[107]. Figure 2.7c schematically depicts a Leviton source with a voltage applied at an Ohmic contact in a quantum conductor. The Fourier transform of this Leviton pulse sequence shows that the energy spread of the wave package is exponentially decaying towards higher frequencies above the Fermi sea as shown in figure 2.7d. Levitons are a high frequency probe for electronic transport. The measurement schemes already show that Leviton signal processing needs only good Ohmic contacts, a microwave electronic waveguide and precise voltage conditioning at room temperature, whereas quantum confined sources need more elaborated gates and gate tuning control at low cryogenic temperatures. Bandwidth is one of the limitations of the theoretical speedup in latency of the execution of a task at a fixed workload in information processing. Bandwidth considerations and improvements are important in communications for processing classical signals, in parallel computing (Amdahl's law) and also in quantum-electronic transport as described in the following chapter, where design guidelines are discussed.

*"It's no longer a physicist's dream - it is an engineer's nightmare."*

– Isaac Chuang

# 3

# DESIGN GUIDELINES FOR QUANTUM NANOELECTRONIC DEVICES

In this chapter, I outline design considerations and simulations for the solid state devices characterized during the thesis. First, I introduce semiconductor heterostructures. Then, I describe electrostatic Poisson simulations, waveguide calculations and interconnects to bring ultra-fast pulses down to nanometer scales at low temperatures. The basis to study fast electronics is a semiconductor heterostructure which supports high mobility transport. The focus of the new sample generation is on fast operation. Therefore, the ohmic contacts and the QPCs are optimized compared to earlier sample designs for high frequency operation. The RF mode transmission limit is currently up to 40 GHz set by the coaxial lines with K connector. The basis for fast electronic transport is a 2DEG with high mobility.

## 3.1 SEMICONDUCTOR HETEROSTRUCTUES

High mobility wafers are grown using high-quality molecular-beam epitaxy growth techniques[117,153]. Low growth rates of only 0.1 to two monolayers per second accessible in molecular beam epitaxy allow to produce atomically smooth interfaces. The impurity and defect concentration can be very low, down to the order of $10^{13}\,\mathrm{cm}^{-3}$ under ultra high vacuum conditions. Best vacuum conditions, sharp interface transitions tunable by the growth rate and low defect contamination form the basis to achieve very high electron mobilities exceeding $10^7\,\mathrm{cm}^2\,\mathrm{V}^{-1}\,\mathrm{s}^{-1}$. Aluminium gallium arsenide (AlGaAs) heterostructures are the only material system where such high mobilities can be reached presently. Graphene encapsulated in boron nitride is catching up lately with mobilities exceeding $10^6\,\mathrm{cm}^2\,\mathrm{V}^{-1}\,\mathrm{s}^{-1}$[9]. The stacking of a typical high electron mobility AlGaAs heterostructure is schematically depicted in figure 3.1a and 2.3d. I outline the sample fabrication in the following. The substrate on which gate patterns are defined is a high electron mobility transistor. The HEMT wafer consists of a GaAs substrate and an embedded $\mathsf{Al}_{0.3}\mathsf{Ga}_{0.7}\mathsf{As}$ quantum well heterostructure with silicon (Si) doping. There is a natural oxide layer of $\approx 4\,\mathrm{nm}$ on top of the GaAs capping layer. Depletion gates out of gold, coplanar transmission lines, ohmic contacts and the bridge structure are deposited on this wafer surface following the process steps[161] described in the appendix A and summarized subsequently. A height profile of the different layers measured by optical interferometry is shown in figure 3.1b. In a first step, the wafer surface is partly etched down around 150 nm to set free the so-called mesa. The mesa predefines the region where the electron gas is located, which is very susceptible to charge fluctuations. In the following, ohmic contacts depicted schematically in figure 3.1a are evaporated using a low bandgap NiGeAu alloy contact layer. The ohmic contacts can be seen as small red spikes in figure 3.1b since the evaporation thickness is primarily around 400 nm. The sample is then annealed at 450 °C for one minute to form a contact from the contact pads down to the 2DEG around 100 nm below the surface of the wafer. After that, small gates for the central structure with a thickness of 15 nm are deposited. Finally, Schottky gates (orange) and RF lines (yellow big pads and center conductor) are evaporated with a thickness of 170 nm.

Figure 3.1c shows the RF transmission lines for injection and fast pinch-off and QPC filtering control. The central part of the electronic Mach-Zehnder interferometer with a three-dimensional bridge supported by an insulating SU8 resist layer can be seen in figure 3.1d. Two additional nano-lithography layers together with the number of needed operational gates (>20) complex the sample design and can reduce the yield of the fabrication. Fabrication of similar quantum-electronic interferometer samples is delicate and is currently done in a reproducible way by only few specialized groups in the world. An alternative to a multi-layer fabrication would be using magnetic fields to create and split quantum hall channels. The gates, which are evaporated on the surface define Schottky gates for 2DEG depletion, transmission lines for high frequency injection and QPC sampling and ohmic contacts for read-out and setting a stable charge background reference. High frequency signals need to be sent down to the nanometric quantum conductor lines using transmission lines. A tapered coplanar waveguide structure shown in figure 3.2a is used as a transmission line. It consists of a center conductor with width $W$ and thickness $T_{met}$ and length $L$, two co-parallel air slots with a width $S$ and ground planes at both sides and at a substrate height $H$ below the metallic strip lines to confine and shield the traveling wave. These dimensional parameters are then also used to simulate the electromagnetic field profiles and the impedance of the coplanar waveguide[43,173].

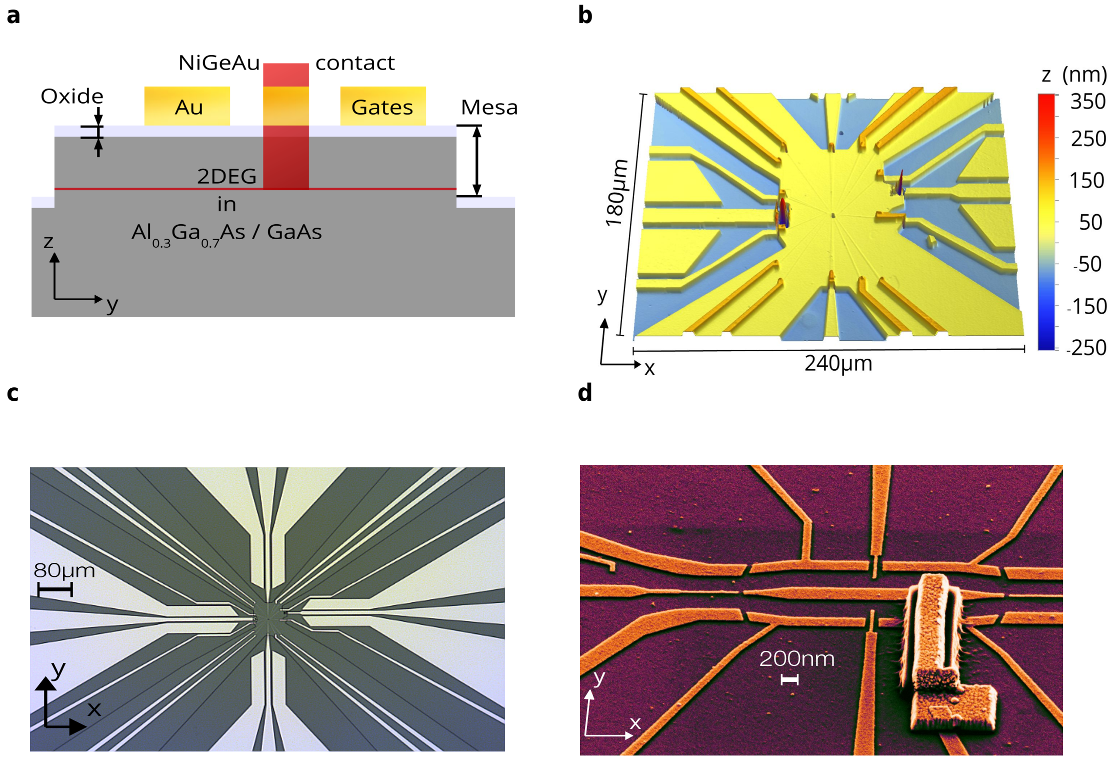

**Figure 3.1.** | **Electronic Mach Zehnder interferometer.** **a**, Side view of the sample scheme of a cut through the sample. **b**, Top view of the sample chip. Height profile of the sample layers by optical interferometry **c**, Top view of the sample similar scale as **b**,. Optical microscope images of the RF lines and contacts. **d**, Tilted top view of the central part. SEM image of the interferometer.

## 3.2 SAMPLE DESIGN FOR CHIP INTEGRATION

A transmission line needs to convert the incoming radiation down to a small scale without strongly reflecting, dephasing and deforming the incoming waveform. Thus, the on-chip waveguide is tapered starting from a slot width $S = 125\,\mu m$ and a conductor width $W = 200\,\mu m$, as shown in figure 3.2b. The GaAs substrate has a height of $H_{GaAs} = 508\,\mu m$ (wafer specification $H_{GaAs} = (500 \pm 25)\,\mu m$) measured at the edge of the HEMT wafer with an optical microscope. The dielectric permittivity is $\epsilon_r = \epsilon_{GaAs} = 12.9$. This leads to a calculated characteristic impedance of the $Z_0 \approx 46\,\Omega$ and down close to the sample at $S = 10\,\mu m$ and $W = 10\,\mu m$ to an impedance of

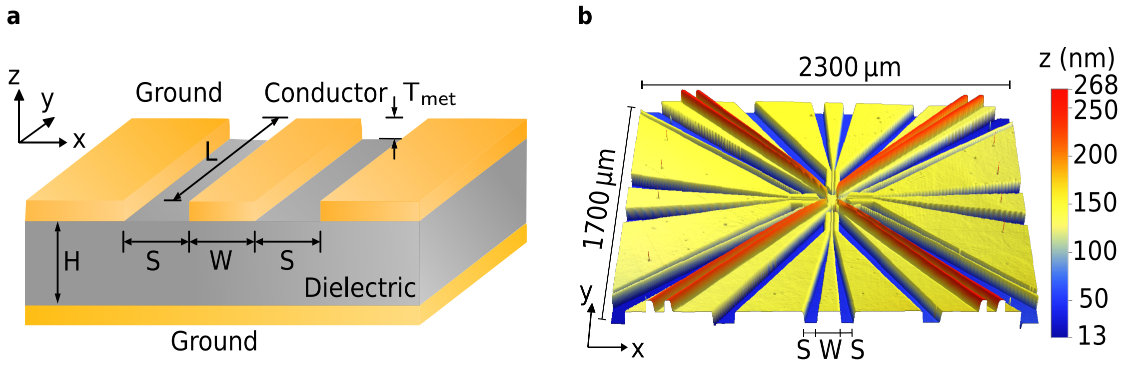

**Figure 3.2. | Waveguide design. a**, Schematic view of a coplanar waveguide for frequency analysis. Simulation parameters of a metallic transmission line are the thickness $T_{met}$, the height of the dielectric $H$ between the ground planes, width of the air slot $S$, width of the center conductor $W$ and length $L$. **b**, Measured height profile of the sample chip with coplanar waveguides. Tapering coplanar waveguide lines from $S_0, W_0 = (125, 200)$µm to $S_1, W_1 = (10, 10)$µm at a measured height $T = 150\,\text{nm}$ on a GaAs chip and $H_{GaAs} = 508\,\mu\text{m}$. This leads to the impedances $Z_0, Z_1 = (47, 56)\Omega$ with $ffl_R = 12.9$.

$Z_1 \approx 57\,\Omega$ The standard waveguide calculation uses conformal mappings of the coplanar waveguide geometry leading to an effective permittivity $\epsilon_{eff}$:

$$\epsilon_{eff} = 1 + q \cdot (\epsilon_r - 1) \tag{3.1}$$

and the impedance[173]:

$$Z_{CPW} = \frac{60\pi}{\sqrt{\epsilon_{eff}}} \frac{1}{\frac{K(k_1)}{K'(k_1)} + \frac{K(k_3)}{K'(k_3)}}. \tag{3.2}$$

The complete analytical formulae are shown in the appendix A.7. It is important to note that analytical formulae using the parameters shown in figure 3.2a are quite accurate approximations of the dispersion relation up to THz frequencies of common transmission line designs[75].

There are many different waveguide geometries such as the micro strip, slot waveguides, coplanar waveguides, substrate integrated waveguides as also combinations of them. The standard geometries can be simulated using the Maxwell equations with

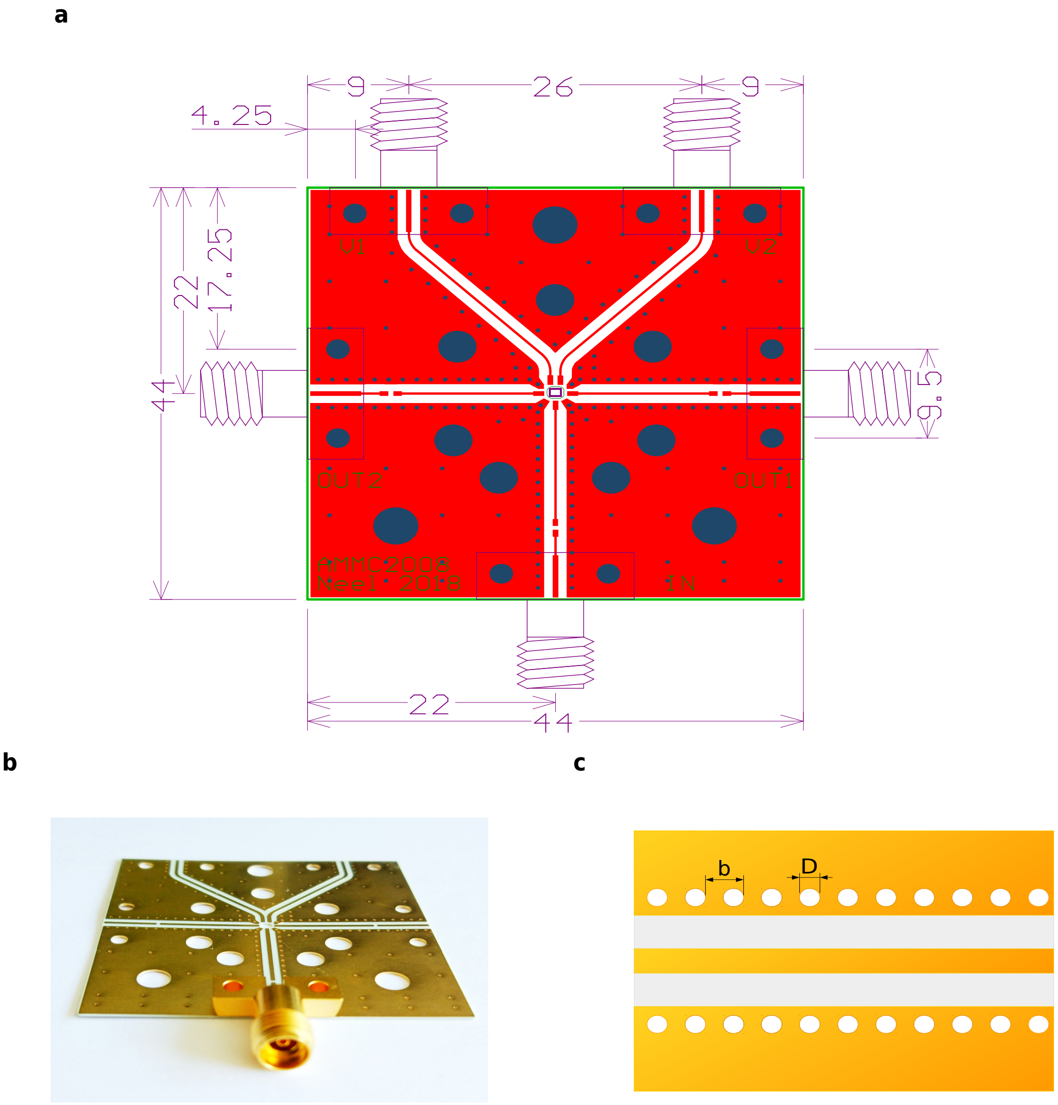

**Figure 3.3. | PCB design for a 50 GHz switch. a**, PCB design for a 50 GHz SPDT (single pole double through) switch (Avago AMMC 2008). **b**, PCB chip with a RF dielectric (RO4350B) ENIG surface finish, different via hole diameters, and a via hole fence along the coplanar waveguide **c**, Via hole dimensions for a substrate integrated waveguide hole diameter *D* and inter-hole distance *b*.

for instance a microwave circuit simulator[186]. The simulation of diffent via hole diameters and distances leads to design guide lines for via holes of substrate integrated waveguides used in all the PCBs designed during the project[181]:

$$D < \lambda_g/5 \tag{3.3}$$

$$b < 2D, \tag{3.4}$$

where $\lambda_g$ is the smallest guided wavelength leading to a cut-off frequency $f_c = \frac{hc}{\lambda_g}$ and $b$ is the distance between two via holes with diameter $D$. A PCB design with via hole fences is exemplary shown in figure 3.3 together with the produced PCB chip for a 50 GHz switch. The device structure portrayed above is studied in the following simulations.

## 3.3 ELECTROSTATIC ENVIRONMENT

The gate pattern provides a distinct way to deplete and pinch off conducting channels in the electron gas below the Schottky gates using negative voltages around −1 V. The effect of Schottky depletion gates can be simulated electrostatically using the Poisson equation and a numerical solver to map the gate geometry[71]. Therein the gates are discretized using rectangles and polygons[46,174]. The poisson equation is then solved and tuned with realistic device parameter estimates. Figure 3.4 shows the potential map cut at the height of the 2DEG sheet. The Schottky gates define an upper and lower path to form an interferometer depicted also by the blue and green dashed vertical cuts. The horizontal cut through the potential map at $y = 0$ in figure 3.4 shows the central island and the low potential tunnel-coupled region. The arms of the two-path interferometer can be probed by point contacts. Tunneling between the arms can be tuned by applying a voltage at the tunnel-coupled wire split gate as it is depicted by

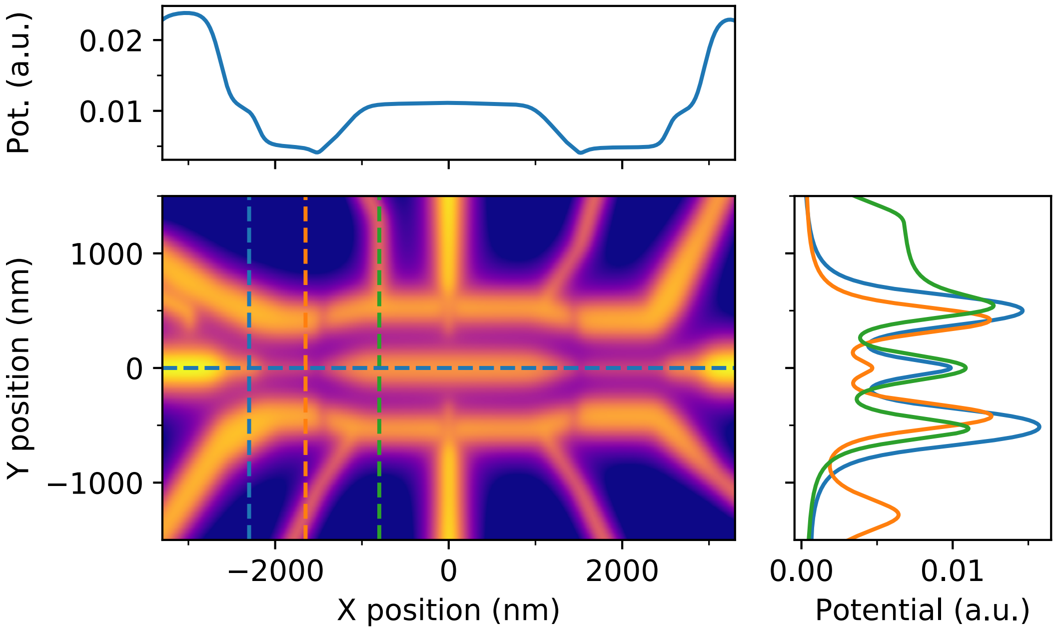

**Figure 3.4. | Simulated electrostatic confinement by the Schottky gates of the sample shown in figure 3.1d.** Electrostatic potential map at the heigt of the 2DEG calculated using a numerical Poisson solver [71]. Schottky depletion gates define an interferometer with two arms, which can be probed by point contacts. The horizontal cut through the potential map (top part) depicts the central island and the low potential tunnel coupled region. The three vertical cuts on the right side show the formation of two channels (blue and green dashed line cut) with tunable tunnel coupling (orange line cut) by a tunnel-coupled wire split gate.

the vertical cut (orange dashed line) on the right side of figure 3.4. The three vertical cuts show the formation of two channels with tunable tunnel coupling by split gates[15]. The complete bandstructure including the doping for getting the exact pinch-off voltages can then be obtained with a 3D numerical simulation of the high electron mobility transistor[26].

The sample is then connected using multiple bond wires and RF mini smp connectors as described in the following.

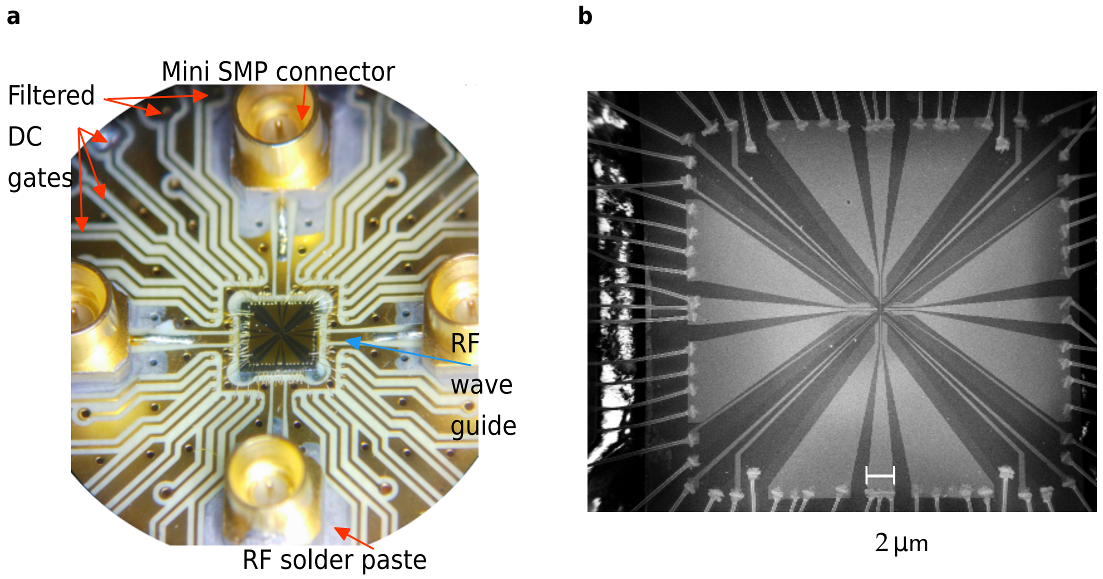

**Figure 3.5. | Wired connections to the sample chip. a**, PCB with connectors, sample chip and bond wires. RF lines with mini SMP connectors soldered on the Ni Au plane of the sample PCB chip using RF solder paste. Six DC lines at the four corners and coplanar wave guides connected using golden bond wires to connect to the center chip with a size of $3.2\times3.2\,\text{mm}^2$, three wires in parallel for the RF waveguide center conductor, multiple wires to the ground planes. **b**, Scanning electron microscope of the sample chip with bond wires. SEM showing tapered waveguides, bond pads, wedge bonds, and multiple bond wire interconnections for higher bandwidth transmission.

## 3.4 CONNECTIONS AT THE DEVICE LEVEL

The sample is connected to the interposer PCB board using 67 bond wires shown in figure 3.5b using a manual wedge bonder (West Bond 7476E). The wire bonding settings are summarized in the appendix A.3.9. Figure 3.5a shows the PCB and the miniSMP connectors solder to the PCB with RF solder paste and a little droplet of tin solder. The HEMT chip with a size of $3.2\times3.2\,\text{mm}^2$ and a height of $\approx 500\,\mu\text{m}$ is glued inside a hole of the PCB using Varnish adhesive (GE 7031) to obtain a flat surface transition between the sample chip wafer and the coplanar transmission lines. Figure 3.6 shows the PCB board and cut-out for the device under test. The new board I designed during the thesis project features more DC lines (32) and improved characteristics of the RF

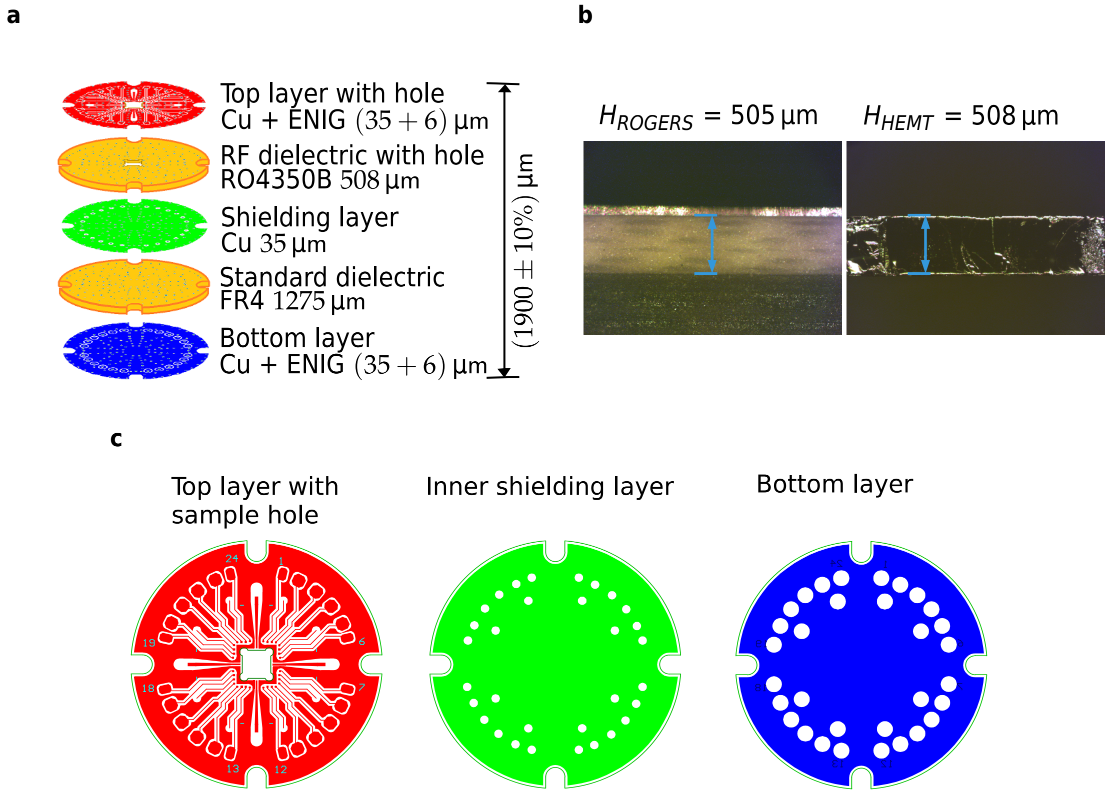

**Figure 3.6. | PCB sample holder design.** **a**, PCB board and cut-out for the device under test. Stacking of the PCB layers and hole for sample chip, with design sizes and typical production error (10%). **b**, Cross section height measurement. Measured height of the PCB layers and the HEMT. The RF dielectric inset RO4350B and the sample chip should form a flat surface ($\Delta(H) << \pm 100$ µm) once glued inside the *PCB* on the copper ground plane using Varnish (GE 7031) **c**, Zoomed top view of the metallic layers of the PCB from top to bottom. .

lines (4) as presented later in chapter 5. The PCB consists of two functional layers one high frequency layer (Ro4350B) with waveguides and high frequency connectors on the top side and a low frequency part (FR4) on the bottom side. The stacking of the PCB layers and hole for sample chip have a typical production error of around 10% which is also comparable to the HEMT wafer specification $(500 \pm 25)\,\mu\text{m}$. A high frequency, low-temperature compatible dielectric (RO4350B) with a measured height of $(505 \pm 1)\,\mu\text{m}$ is used for the top part. The ENIG (Electroless nickel immersion gold) surface finishing is around $(43 \pm 1)\,\mu\text{m}$ high as measured in the cross section microscope image 3.6b. The lower layer of the PCB is isolated from the top part by a Cu ground plane. The lower side is then produced with standard dielectric FR4 and leaves space and pads for the DC to MHz lines, filters and surface mount circuits. The RF dielectric with the ENIG surface and the sample chip glued inside the PCB on the copper ground plane form a flat surface. A flat surface transition and a close position $L < 500\,\mu\text{m}$ of the RF waveguides on the PCB to the waveguides on the sample chip ensure good impedance matching. Typically, the parasitic inductance of a bond wire interconnect[94] is $1\,\text{nH}\,\text{mm}^{-1}$. It is important to use several bond wires in parallel to obtain a high bandwidth connection with a low impedance at high frequencies, since bond wires acts as parasitic inductors. The bond wire's inductance scales with the length $L$, the diameter $d$ and the height $h$ over the ground plane. The scanning electron microscope image in figure 3.5b displays three bond wires in parallel connected to the center conductor of the coplanar waveguide to ensure that the parasitic inductance is low and the transmission can go to high frequencies. The RF characterization of the connected waveguides and the PCB is presented in chapter 5. A highly sensitive detection is desirable to measure small signals inside an electronic quantum circuit. Therefore, the following parts of the cryogenic setup are optimized during the project.

*"Divide et impera! - Divide and rule!"*

– Gaius Iulius Caesar

This maxim characterizing the foreign
policy of the Roman emperor Gaius Iulius
Caesar should only be applied to noise
and signals

# 4

# STABILITY AND LOW NOISE PULSE CONTROL

In this chapter I introduce the low frequency part of the experimental setup. The stability of the measurement apparatus, signal recovery and the corresponding noise figures are explained and analyzed in a systematic way. I start with the signal description in the complex Fresnel plane and outline how noise and errors propagate. Then, the low noise amplification together with the respective noise spectrum is portrayed. As an example two low noise measurements of current and voltage with a femto ampère respectively sub-nano volt noise floor are introduced. In the following, I characterize the programmable voltage and current sources measuring their long time drift stability. The gain stability of the amplifier setup is subsequently improved in three steps. First, a PID controller stabilizes the room temperature amplifier, second the cryogenic HEMT amplifier is polarized using the Neel voltage source (DAC) and third a stable oscillator is taken as a Lock-in reference for homodyne detection and signal recovery. Finally a coaxial line is designed and tested connecting from the sample level to the HEMT amplifier to keep a flat pass band for amplification.

Quantum hardware reaches limits where a single wave function is confined and sensed at a very small length scale of only several tens of nanometers. Small changes in gate voltages and spurious noise signals can be detrimental for controling a quantum state since they create relatively big electric field effects at nano-metric scales ($|\mathbf{E}| \propto 1/|\mathbf{r}|$). Therefore, noise and stability characterization of an electronic setup for testing quantum hardware is crucial for reliable operation and coherence. Quantum coherence is directly related to temperature[2] and is a limiting factor for controlling quantum device operation. Quantum hardware is consequently often cooled down to very low temperatures more than 100 times colder than the interstellar space, around 10 mK, to facilitate coherent quantum operation. Optimized pulse engineering can then remove measured correlated errors to reduce the gate error rate and achieve fault tolerance in prototype qubit circuits[183]. Low temperature operation needs specialized and expensive equipment, which needs to be engineered for cryogenic temperatures as outlined subsequently. Figure 4.1 shows a blueprint of the cryogenic setup, with different frequency components for fast pulses in the radio frequency regime (MHz to 100 GHz) highlighted in blue. The lower frequency part of the setup or static control signals up to some MHz are shown as black lines. The following chapter describes signal recovery, amplification and noise floor characterization starting from low frequencies. Afterwards, the basis for higher radio frequency pulse control at cryogenic temperatures is introduced stepwise.

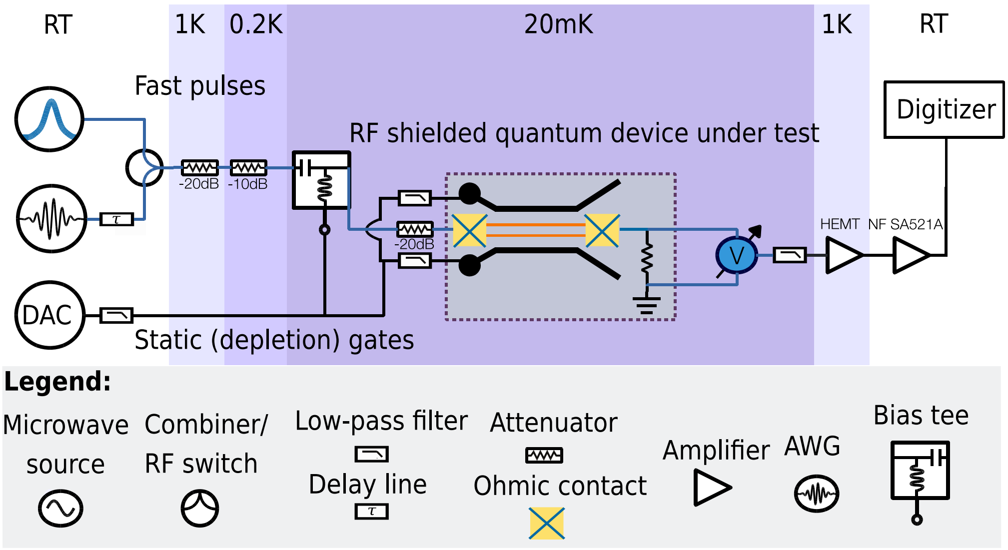

**Figure 4.1. | Blueprint of the cryogenic setup.** From left to right: Injection of signals as programmable wavelets (arbitrary wave function generator (AWG)) and Lorentzian-shaped pulses (pulse box) and static voltages (digital-to-analog converter (DAC)). The color code depicts the different cryogenic temperature stages inside the fridge. Input signals are conditioned (attenuated, delayed, filtered and combined) and applied at a shielded quantum device under test. The output voltage is then measured at low temperature and amplified at two stages using a low temperature amplifier (HEMT) and a room temperature amplifier (NF SA512A). The signal is finally digitized by different possible digital signal processing means for instance time-domain analog-to-digital converter (ADC), frequency spectrum analysis or Lock-In detection.

## 4.1 SIGNAL RECOVERY, NOISE DESCRIPTION AND MEASUREMENT

A physical process which generates a periodic signal is often approximated using an oscillator model. A wavelike description helps to quantify experimental accessible observables like amplitudes, phases, repetition rate or frequency together with their noise and stability[148]. A noise free signal is described as a sinusoidal, oscillating wave:

$$v(t) = V_0 cos(\omega_0 t + \phi), \tag{4.1}$$

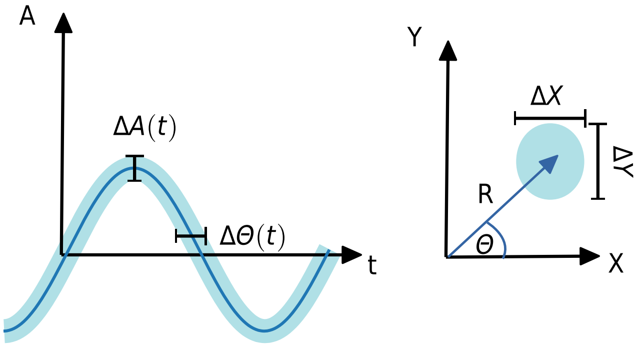

**Figure 4.2. | Signal representation.** Left side time-varying wavelet with amplitude $A(t)$, phase $\Theta(t)$ and corresponding amplitude $\Delta A(t)$ and phase error $\Delta\Theta(t)$. Right side complex signal phasor representation, with magnitude $R$, phase angle $\Theta$ and quadrature components $X$ and $Y$ with corresponding errors $\Delta X$ and $\Delta Y$.

with the $V_0 = \sqrt{2}V_{rms}$ its peak amplitude, $\omega_0 = 2\pi f_0$ its angular frequency and a phase offset $\phi$. An oscillating signal can be rewritten using Euler's formula as a vector **V** in the complex plain called a phasor or Fresnel vector:

$$\mathbf{V} = V_{rms}e^{i\Theta}, \tag{4.2}$$

with the root mean squared amplitude $V_{rms} = R$ given as the length (magnitude) of the signal vector. The signal can be expressed as an analytic signal $z(t)$ in order to ensure that the power of a signal at negative frequencies is zero. The analytic signal is also called pre-envelope in the RF community:

$$z(t) = v(t) + i\tilde{v}(t), \tag{4.3}$$

with the Hilbert transform $\tilde{v}(t) = \frac{1}{\pi}\int_{-\infty}^{\infty}\frac{v(t)}{\tau - t}\,dt$ of $v(t)$. The Hilbert transform is restoring the positive frequency components with a pre-factor two while shifting the negative ones by $\pi/2$ in phase, which therefore negates and subtracts them. The analytic signal of a cosine is then:

$$z(t) = cos(\omega_0 t) + isin(\omega_0 t) = e^{i\omega_0 t}, \tag{4.4}$$

known as the Euler formula leading to a complex exponential or phasor. An analytic signal is the natural extension of a phasor, since is not only limited to sinusoidal inputs and allows the amplitude and phase to vary in time. The analytic signal is useful to calculate modulations and convolutions of signals. A modulated signal $\underline{z}(t)$ using a local oscillator modulation at $w_{LO}$ as an envelope can then be written as a multiplication:

$$\underline{z}(t) = z(t)e^{-i\omega_{LO}t} = z_m(t)e^{i(\Phi(t)-\omega_{LO}t)} = I(t) + iQ(t), \tag{4.5}$$

where $z_m(t) = |z(t)|$ is the instantaneous amplitude envelope, $\Phi(t) = \arg(z(t))$ is the instantaneous phase. The resulting signal is called complex envelope or complex baseband. The real part of the complex envelope is the so-called in-phase component $I(t)$ and the imaginary part the quadrature phase component $Q(t)$. Analog frequency conversion of signals is often done using IQ mixing techniques. A high frequency signal modulated at a lower frequency can then be measured at the down-converted frequency or baseband $B$. The signal can be resolved alias-free when the sampling frequency $f_S$ is at least two times bigger than the base bandwidth $2B < f_S$ which is known as Shannon-Nyquist sampling theorem[154]. A common measurement of a local oscillator modulation is the lock-in detection where the modulation of the signal at $\omega_{LI}$ gives the magnitude $R$ and phase $\Theta$ of a measured signal as:

$$R(\omega_{LI}) = \sqrt{I^2 + Q^2} \qquad \text{(V)} \tag{4.6}$$

$$\Theta(\omega_{LI}) = arctan(I/Q). \qquad (^{\circ}) \quad (4.7)$$

Modern homodyne detection setups for lock-in amplification are based on digital mixing techniques. A lock-in amplifier can be built starting from a low noise front-end amplifier and a software defined radio where the RF signal processing - here the conversion to I and Q components - is implemented by means of software on the digitized data[115]. Quadrature components of a wave signal are governed by the Heissenberg uncertainty relation. Consequently, the measurement precision of the conjugate observables of a resonating wave can go down to the quantum limit given by their product area of:

$$\Delta X \ \cdot \Delta Y = \Delta I \cdot \Delta Q \geq 1/4 \qquad (4.8)$$

The quantum limit of sensitivity also applies in the same way for the measured I and Q components of a microwave signal[23]. The noise of an oscillating signal can be on the amplitude $\Delta\alpha(t)$ and the phase $\Delta\phi(t)$. Noise is experimentally characterized by its spectral distribution. In 1914 Einstein discussed on a meeting of the Swiss Physical Society in Basel a method for the determination of statistical values from quantities under irregular fluctuations. In this short note he introduced the first measurement of the noise spectrum using a Fourier transform[57]. The power spectral density associated with a random process $\mathbf{x}(t)$ can be derived from the Fourier transform of the autocorrelation function $R(\tau)$[131]:

$$S^{II}(\omega) = \int_{-\infty}^{\infty} R(t)e^{-i\omega t}\, dt \qquad (4.9)$$

$$R(\tau) = E\left(\mathbf{x}(t)\mathbf{x}(t+\tau)\right), \qquad (4.10)$$

where $R(\tau)$ is the auto-correlation function, and $S^{II}(\omega)$ the Fourier transform. The Fourier transform can only be integrated on a finite observation time in a real life measurement. Therefore it is convenient to introduce the truncated signal $x_T(t)$:

$$X_T(\omega) = \int_{-T/2}^{T/2} x(t)e^{-i\omega t}\,dt, \tag{4.11}$$

with the integration time $T$ setting the bandwidth of the spectral density measurement. The truncated signal then leads to the power spectral density using a measurement averaging $m$ times:

$$S^{II}(f) = \frac{1}{T}\,\langle|X_T(f)|\rangle_m\,, \tag{4.12}$$

with $f = \frac{\omega}{2\pi}$. The one-sided, positive frequency power spectral density is commonly measured in experiments and follows as:

$$S^{I}(f>0) = 2\cdot S^{II}(f) = \frac{2}{T}\,\langle|X_T(f)|\rangle_m \tag{4.13}$$

The noise of a signal is frequency dependent and characterized along its quantization axes as for instance here amplitude and phase. Signals are amplified and digitized to recover even low signal variations from the noise floor. A spectral voltage noise after an active element like an amplifier as shown in figure 4.3b often follows an inverse power law:

$$V_n(f) = A\cdot 1/f^n + V_{white} + \delta(f_i), \qquad (\mathrm{V}/\sqrt{\mathrm{Hz}}) \tag{4.14}$$

with exponent $n$, DC amplitude offset $A$, noise floor offset $V_{white}$ and noise peaks $\delta(f_i)$. The noise equivalent spectral power density of a typical room temperature operational voltage amplifier with no additional noisy input signal is then proportional to[78]:

$$V_n^2(f) = v_w^2\cdot f_w\cdot\int_{f_1}^{f_2} 1/f\,df \qquad (\mathrm{V}^2\,\mathrm{Hz}^{-1}) \tag{4.15}$$

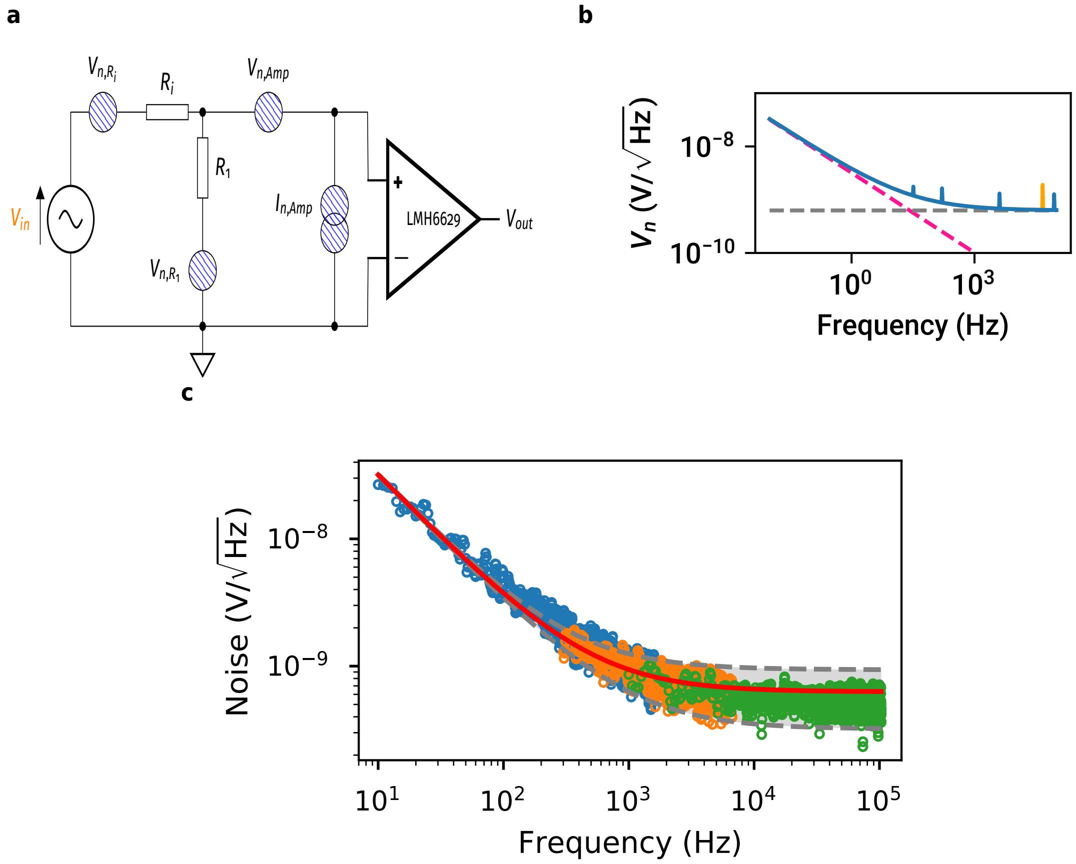

**Figure 4.3. | Noise level measurement of an operational amplifier. a**, Schematic of an operational amplifier and its typical noise sources. An oscillating input signal is applied at a resistive divider consisting of the device under test with input resistance $R_i$, a fixed resistor to ground $R_1$. The noise sources are given by the noise at the resistors $V_{n,R}$ and the current noise at the room temperature measurement amplifier input $I_{n,Amp}$ **b**, Spectral voltage noise density. Typical noise characteristic of a low noise operational voltage amplifier (e.g. Texas Instruments LMH6629) at room temperature of the order of $0.7\,\mathrm{nV}/\sqrt{\mathrm{Hz}}$ with a low frequency $1/f$ flicker noise (shown as pink dashed line) and a broad-band, white noise offset (constant shown as grey dashed line). If an oscillating signal (orange) injected or noise is collected, spectral sharp lines can be seen in the noise spectrum of the output signal $V_{S_0}$. **c**, Measured base noise level of the NF SA521-SA room temperature amplifier. The different colors for the data points correspond to three different bandwidths measured. Red line is the best inverse $1/f$ fit with one standard deviation as dashed black lines.

The constant background is called white noise $v_w$ and consists of frequency independent noise sources such as current shot noise and thermal Johnson-Nyquist noise. Johnson-Nyquist voltage noise on a resistor $R$ at temperature $T$ is defined via:

$$v_n = \sqrt{4k_B T R \Delta B}, \tag{4.16}$$

where $\Delta B$ is the measured bandwidth and $k_B$ is the Boltzmann constant (cf. 3). The flicker noise follows an inverse power law $1/f^n$. $1/f$ noise is called pink (-3dB per octave) or brown noise (-6dB per octave) dependent on the slope of the noise power spectrum in log-scale. The 1/f noise originates from irregular fluctuations of the output amplitude which become more probable on longer time scales which is also called flickering. Flicker noise can for instance arise from random or thermally excited charge movements in the channel of an active field effect transistor device. Faster irregular fluctuations with a fixed frequency lead to peaks $\delta(f_i)$ in the noise spectral density. The peaks can originate from oscillating sources such as noise at multiples of the switching power supply frequency, vibrations or ground loops. A bad ground reference or ground loop acts like an antenna which picks up stray fields. A single clean ground reference, noise cancelling for instance in a differential amplifier configuration and shielding can help to reject noise and perform low noise measurements[134]. Noise and uncertainties propagate along with the signal. The total noise amplitude of a signal adds up from the different independent noise vectors. As illustrated in the circuit scheme in figure 4.3a, there are three main contributions to the total (RMS) voltage amplitude noise $e_{total}$ of an amplifier:

$$e_{total} = \sqrt{V_n^2 + (I_n \cdot R_n)^2 + \left(\frac{k_B T_n}{e}\right)^2} \cdot A_V, \qquad (\mathrm{V}) \quad (4.17)$$

where $V_n$ is the voltage noise, $R_n$ is the Thevenin equivalent resistance of the circuit under test. In figure 4.3a for instance, this leads to the equivalent voltage $V_{th} = V_{in} \cdot \frac{R_1}{R_1+R_i}$ and the Thevenin resistance $\frac{1}{R_n} = \frac{1}{R_{th}} = \frac{1}{R_1+R_i}$. $I_n$ relates to the current noise of the amplifier, $T_n$ is thermal Johnson-Nyquist voltage noise (cf. equation 4.16) of the resistive elements in the circuit and $e$ is the elementary charge (cf. appendix 3). Both noise and signal are then amplified by a factor $A_V = \frac{V_{out}}{V_{in}}$ called the voltage gain of the amplifier. Then, the output signal $V_{out}$ propagates to the next setup stage. The gain $g$

of an amplifier can also be expressed on a logarithmic decibel scale relating the power of the amplified output signal to the input signal:

$$g = 10\log_{10}\left(\frac{P_{out}}{P_{in}}\right) = 20\log_{10}\left(A_V\right) \qquad \text{(dB)} \qquad (4.18)$$

An oscillating input signal as shown by the orange voltage peak in figure 4.3b needs to be recoverable from the blue noise floor curve of all noise sources. In the following electrical current and voltage measurements are described with the respective obtainable low noise levels.

### 4.1.1 *Femto ampère and nano volt measurements*

A current of a small level of fA can be measured using a current-to-voltage (IV) converter. An IV converter is for instance used to measure pinch-off current to voltage curves at point contacts or to measure conductance at a quantum dot sensor. IV converters for very sensitive current measurements with noise levels below $1\,\mathrm{fA}/\sqrt{\mathrm{Hz}}$ are often based on a transimpedance operational amplifiers. An ideal ampère meter circuit should have zero impedance to acquire all current applied. A transimpedance amplifier is an amplifier which acts like a sink for currents applied at the input, creating in the idealized case a zero input impedance. Circuits for femto ampère IV conversion can be built starting from a transimpedance operational amplifier like the TLC2201 ($0.6\,\mathrm{fA}/\sqrt{\mathrm{Hz}}$ used at the Institute) or an ADA4530-1 ($0.07\,\mathrm{fA}/\sqrt{\mathrm{Hz}}$ at $0.1\,\mathrm{Hz}$) at the input stage. The output voltage $V_{out}$ of a single stage inverting amplifier configuration is then proportional to the current via Ohm's law $V_{out} = -R_f \cdot I_{in}$, where the feedback resistor $R_f$ sets the gain and the inverting configuration leads to the minus sign. A full IV converter circuit design with good shielding, low leakage currents and switchable gain factor can then convert very small femto ampère current changes into voltages[180]. After the IV conversion, the voltage is measurable with a standard digital multimeter in the volt range. Electrometers based on high gain IV converters are normally designed with a very high valued feedback resistor ($R_f \approx$ GΩ range) limiting the bandwidth. The bandwidth $B$ of an amplifier circuit is normally given by the $-3\,\mathrm{dB}$ points forming a plateau at which the constant signal amplitude does not decrease more than a factor of $-3\,\mathrm{dB} = 1/\sqrt{2}$. Thus, the most sensitive IV converters are often used at low frequencies in the kHz range.

Voltage amplification is used next to IV converters for nano volt measurements at higher frequencies in the kHz to MHz range. We commonly use a load resistor to ground (or a resonator circuit) at low temperatures to acquire low noise voltages for instance from a current flowing in a quantum conductor. Nano volt sensitive detection circuits in the kHz to MHz range are built starting with very low noise operational amplifiers with noise levels below $1\,\mathrm{nV}/\sqrt{\mathrm{Hz}}$[78]. Next to the noise level, it is important to optimize also the signal-to-noise ratio (SNR) and the gain bandwidth product:

$$GBWP = A_V \cdot B, \tag{4.19}$$

given by the voltage gain $A_V$ and the $-3\,\mathrm{dB}$ bandwidth $B$ in MHz. An example of a high gain amplifier circuit design is based on the LMH2669 ($0.69\,\mathrm{nV}/\sqrt{\mathrm{Hz}}$)[164]. The voltage amplifier board has a total gain of $A_V = 100000$, a white noise level around $1\,\mathrm{nV}$ and a bandwidth of around $10\,\mathrm{MHz}$ limited by the high gain settings of the first stage LMH2669 amplifier $A_{V1} = 100$. A low noise room temperature amplifier can then be used to amplify low voltages commonly ranging from nV to $100\,\mu\mathrm{V}$ from quantum device channels to detect at a digitizer.

Very low noise level measurements with a noise spectral density below $\mathrm{fA}/\sqrt{\mathrm{Hz}}$ or $\mathrm{nV}/\sqrt{\mathrm{Hz}}$ are special in the sense, that a lot of care has to be taken regarding the power supply noise, good shielding from interfering stray noise fields or and the elimination of ground loops[134]. Ground connections should form a star configuration starting from the device under test. The star center is here for instance the fridge ground plane or the amplifiers ground reference as depicted in the schematic 4.4. A star grounding technique means that the DAC is floating and connected to the device under test. Then, a noise spectrum analyzer is used to measure the noise level. If the obtained noise spectrum is not on the specified level, there needs to be a noise source which couples into the measurement. A good practice is then to decouple everything from the mains supply, for instance as a first check by switching off and unplugging devices until the base noise level of the amplifier of nano volts or femto amperes is obtained. Once a problem or a ground loop is detected, possible improvements can be isolation transformers, better regulated power supplies, isolation of the data communication and decoupling of sensitive measurement instruments like low noise amplifiers from switching power supplies such as the data analysis PC. It can also be worth following an application note with detailed grounding, shielding and power supply schematics[110]. Modern regulators in low noise power supplies have a high power supply ripple rejection (LT3045 $PSRR = -120\,\mathrm{dB}$, $NSD = 2\,\mathrm{nV}/\sqrt{\mathrm{Hz}}$) and can help to provide clean power to the very noise sensitive measurement parts[134]. Signal recovery can be optimized by tuning the signal to noise ratio, filtering out only the wanted signal using for instance a homodyne lock-in detection and adapting the integration time and the number of averages of the measurement. Equivalently to the amplitude, the phase $\phi(t)$ of a signal can be investigated.

### 4.1.2 *Timing jitter*

The timing stability of a periodic RF signal is described by it's phase noise $\Delta\phi(t)$ at the carrier frequency. The timing jitter or standard deviation of the timing uncertainty

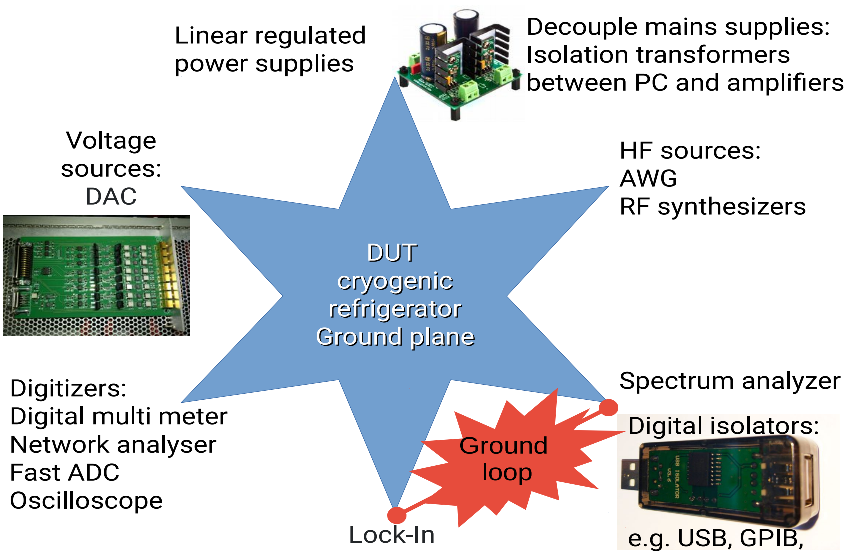

**Figure 4.4. | Star grounding technique. Mind map of a typical electronic setup for low noise measurements.** The device under test and its amplifier is connected to the noise spectrum analyzer. Power is taken from a mains supply which is decoupled using an isolation transformer. Power supplies for voltage sources and amplifiers are linear and low noise regulated in order to not introduce switching noise. Noisy equipment needs to be decoupled and ground loops between instruments can be resolved using isolators. Extra measurement equipment like digitizers or HF sources are connected to the ground plane and switched on one by one to keep track of changes in the noise level of the DUT on the noise spectrum analyzer.

$\sigma_\tau$ can be obtained as the integral of the phase noise spectral density. The timing jitter $\sigma_\tau$ is defined as[148]:

$$\sigma_\tau = \sqrt{\frac{1}{\omega_0^2}\mathcal{E}\left([\phi(t+\tau)-\phi(t)]^2\right)}, \qquad \text{(s)} \quad (4.20)$$

with angular frequency $w_0$, phase $\Phi(t)$ and $\mathcal{E}(x)$ the expectation value. Timing and phase noise is important for signal acquisition and stable operation at higher frequencies. Modulations and precise analog signal processing directly suffer from a bad phase synchronization. Phase stability is also important for Leviton pulse generation. Therefore, I also introduce a phase locking setup developed during the thesis project in the subsequent chapter 5. The precision and stability of high frequency signals (mostly up to the GHz range) is a major challenge in analog quantum circuits. The control of the pulse form, jitter and drift stability influence quite directly the infidelities and incoherence[183] of a quantum device. Analog noise analysis and the determination of the corresponding noise time-scales have a high impact even before a feedback or calibration procedure[91] using benchmarking data can compensate or correct towards an optimum calibration point. The following describes measurements and improvements of the noise and stability characteristics during the thesis project.

## 4.2 STABILITY AND NOISE CHARACTERIZATION

Many experiments in particle physics, metrology, quantum simulation with trapped ions, solid state physics and others need stable, low-noise power distribution. The systematic stabilization and investigation of all amplifying stages of a cryogenic setup is very important for long-time measurements such as repeatedly measured communication protocols, device benchmarking or teleportation of quantum gates[38]. A solid-state memory qubit requires a programmable voltage source later on also referred to as DAC for setting gate voltages to tune and keep a constant level scheme with a:

— tunable range of $-3.3V$ to $+3.3V$
— resolution $>$ 12bit
— noise level in the $\mathrm{nV}/\sqrt{\mathrm{Hz}}$ range or below
— stability on the µV range corresponding to a long-time drift below 1 ppm/°C
— sampling rate DC to several MHz for voltage change.
— internal communication time $< 10\,\mu\mathrm{s}$ for setting new bit commands to the analog output

The stability requirements are quite strict, to keep the charge state of, for instance a quantum dot fixed over a long time and rapidly ramp voltage gates to other positions or states in the charge stability diagram. The DAC developed in-house at the Institute on the basis of the NI real-time input-output (RIO) platform (FPGA Xilinx Spartan 3 or Zynq 7 series) fulfills the requirements above. The analog voltage output board

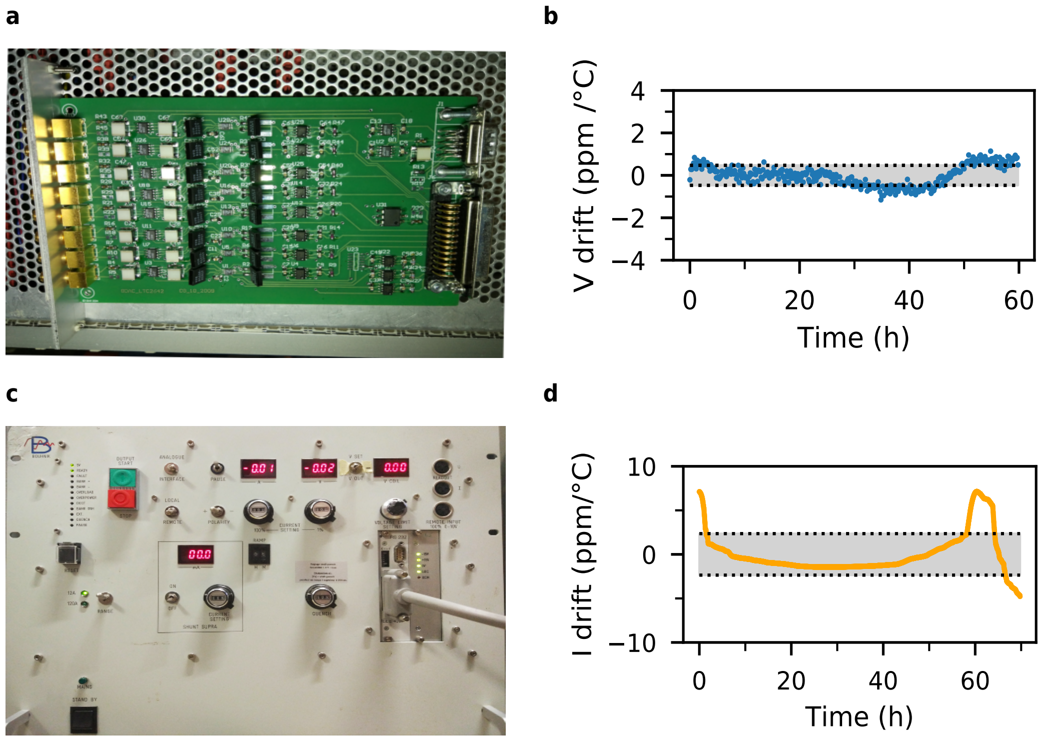

**Figure 4.5. | Long-term stability of the amplitude of the programmable voltage and current sources. a**, Programmable voltage source. Analog PCB daughter board with eight DAC channels mountable in a 19 inch rack. **b**, Voltage amplitude stability of the DAC source measured in blue over 60 hours, the standard deviation of the drift $\Delta(V_{drift}) < \pm 0.5\,\text{ppm}/°\text{C}$ is marked as a grey area in between the dashed black lines. **c**, Programmable current source. Bouhnik current source with 12 A and 120 A range for supplying a stable current to a coil for magnetic field control. **d**, Current amplitude stability of the Bouhnik magnet power supply measured over 70 hours (orange curve), the standard deviation of the drift $\Delta(I_{drift}) < \pm 2.4\,\text{ppm}/°\text{C}$ is marked as a grey area in between the dashed black lines.

with eight DAC output channels is shown in figure 4.5a. Some key components for the performance of the DAC are an ovenized temperature-compensated voltage reference (LTZ1000), a 16-bit DAC (LTC2642) for DC to 50 MHz operation, and precision foil resistors (Vishay Z-series). Long-time drift stability of signals in a setup are represented by a relative signal shift in percent or parts per million. The long time drift stability of the DAC voltage amplitude is measured for characterization over a weekend (60h) at a mean voltage of $V_{mean} = 0.927\,\text{V}$. The measured stability over 60 hours of less than $1\,\text{ppm}/°\text{C} = 1\,\mu\text{V}\,°\text{C}^{-1}$ of the DAC is shown in 4.5b. The white noise level of the DAC is below $20\,\mathrm{nV}/\sqrt{\mathrm{Hz}}$ as measured with the signal analyzer (HP 35670A) directly at the output channel of the DAC. The measured noise and long-time drift stability specifications, compare well or are even better than other widely used programmable voltage sources like the Yokogawa GS200 or the DecaDAC developed in Harvard/Copenhagen. Likewise, the Bouhnik magnet supply delivers a stable current of $I_{mean} = 1.1\,\mathrm{A}$ with a drift of less than $\Delta(I_{drift}) < \pm 2.4\,\mathrm{ppm}/°\mathrm{C}$ measured at the multimeter (K2000) over 70 hours. The measured current drift is in good agreement with the specifications of the DANFYSIK current transducer used inside the magnet power supply for the proportional-integral-derivative (PID) current feedback.

A stabilized low noise voltage source is commonly used to polarize gates of quantum devices, to stabilize ion traps or more generally to input signals. Moreover, the stable, low-noise voltage source can provide a small current and is very useful to stabilize the set-point of ultra-low noise HEMT amplifiers for voltage measurements or current-to-voltage (IV) converters. During my thesis project I want to measure very small signals for instance due to coherent current oscillations detected at the outputs of an electronic Mach Zehnder interferometer. The noise level of such signals is often at the noise level of a standard labratory preamplifier. Thus, an important effort has to be done in order to develop low-noise, low-temperature and also temperature-stable electronics to perform the measurements. Nonlinear elements like amplifiers can be temperature stabilized using a PID controller.

The NF SA-421-F5 voltage amplifier has a low-noise operational amplifier at the input stage (LMH6629 $0.69\,\mathrm{nV}/\sqrt{\mathrm{Hz}}$). It was noticed during the measurements that its gain is not drift-stable and changes with temperature. A Peltier thermo-electric element connected to the amplifier is used to stabilize the voltage amplifier's temperature. The heat can be evacuated using a fan and a heat sink as shown in figure 4.6a. The heat sink is screwed to the amplifier using plastic screws to reduce noise on the ground plane of the amplifier. The ground reference of the amplifier is electrically iso-

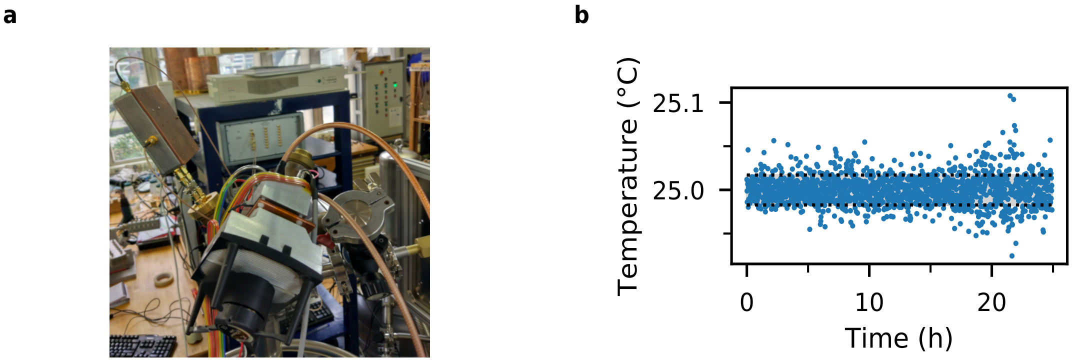

**Figure 4.6. | Long-term temperature stability of active components.**
**a**, PID thermo-electric control setup for stabilization of the low noise amplification chain. **b**, Temperature stability measured at the room temperature amplifier.

lated from the heat sink using the plastic screws. The temperature drift of the amplifier can be compensated well below a level of $< 0.1\,°\mathrm{C}$. The temperature stability is shown in figure 4.6b during one day of measurements. The HEMT amplifier is powered up using the stable voltage source and a restive divider using precision foil resistors. The low temperature HEMT amplifier is then connected to the temperature-compensated room temperature amplifier. The total gain of the amplification chain $g_{max} = 70\,\mathrm{dB}$ can be stabilized with less than 0.1% drift as measured in figure 4.7b.

The small remaining drift is mainly given by the drift of the oscillator of the lock-in amplifier. The oscillator's frequency stability can limit the down-conversion efficiency and is directly seen as an amplitude error on the low frequency base-band signal. The DSP 7625 lock-in amplifier has a typical gain stability ±0.3 %. The gain stability can be improved by using an external more stable local oscillator (Stanford Research DS360) to attain the stability $\Delta(g) < \pm 0.013\,\%$ shown as grey shaded area between the black dashed lines in figure 4.7b. Higher resolution and more temperature stable measurements can additionally be done using an 8.5 digit digital multimeter (HP 3458A) in AC acquisition mode[160]. The motivation for improving low noise amplification in cryogenic setups is also that the noise levels in current setups limiting quantum device

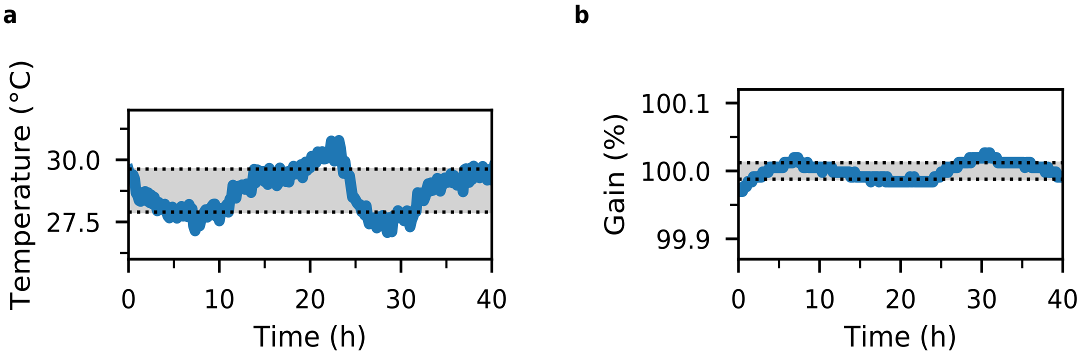

**Figure 4.7. | Long-term stability and temperature drifts of the measurement setup.** **a**, Ambient temperature measured in the laboratory at the lock-in amplifier for gain stability characterization. **b**, Gain stability with standard deviation of $\Delta(g) < \pm 0.013\,\%$ after temperature PID control and power supply by Neel DAC for the amplification chain consisting of HEMT amplifier and NF room temperature amplifier.

operation are well defined and measured. The following describes measurement and design strategies how to characterize and improve the noise limit.

## 4.3 LOW NOISE AMPLIFICATION FOR CRYOGENIC SETUPS

The white noise level of the gate defined quantum dots in a cryogenic quantum setup is of the order of $1\,\mu\mathrm{V}/\sqrt{\mathrm{Hz}}$[11,64,76]. Good commercial room temperature electronics has a noise level in the $\mathrm{nV}/\sqrt{\mathrm{Hz}}$ to hundreds of $\mathrm{pV}/\sqrt{\mathrm{Hz}}$ range[78] as outlined above in subsection 4.1.1. Low noise devices are normally powered up by low noise regulators or use active noise-cancellation by an amplifier feedback loop. The geometrical gate capacitance of small quantum dots is of the order of tens of aF. The nano-metric small dimensions imply that single defects or changes in the confinement potential configuration close-by can create strong electric field effects. Spurious charge noise needs to be investigated and precisely controlled. The noise level of solid state qubits is generally very sensitive to two level system fluctuations in close proximity to the readout line before amplification. Two-level fluctuations in the underlying dielec-

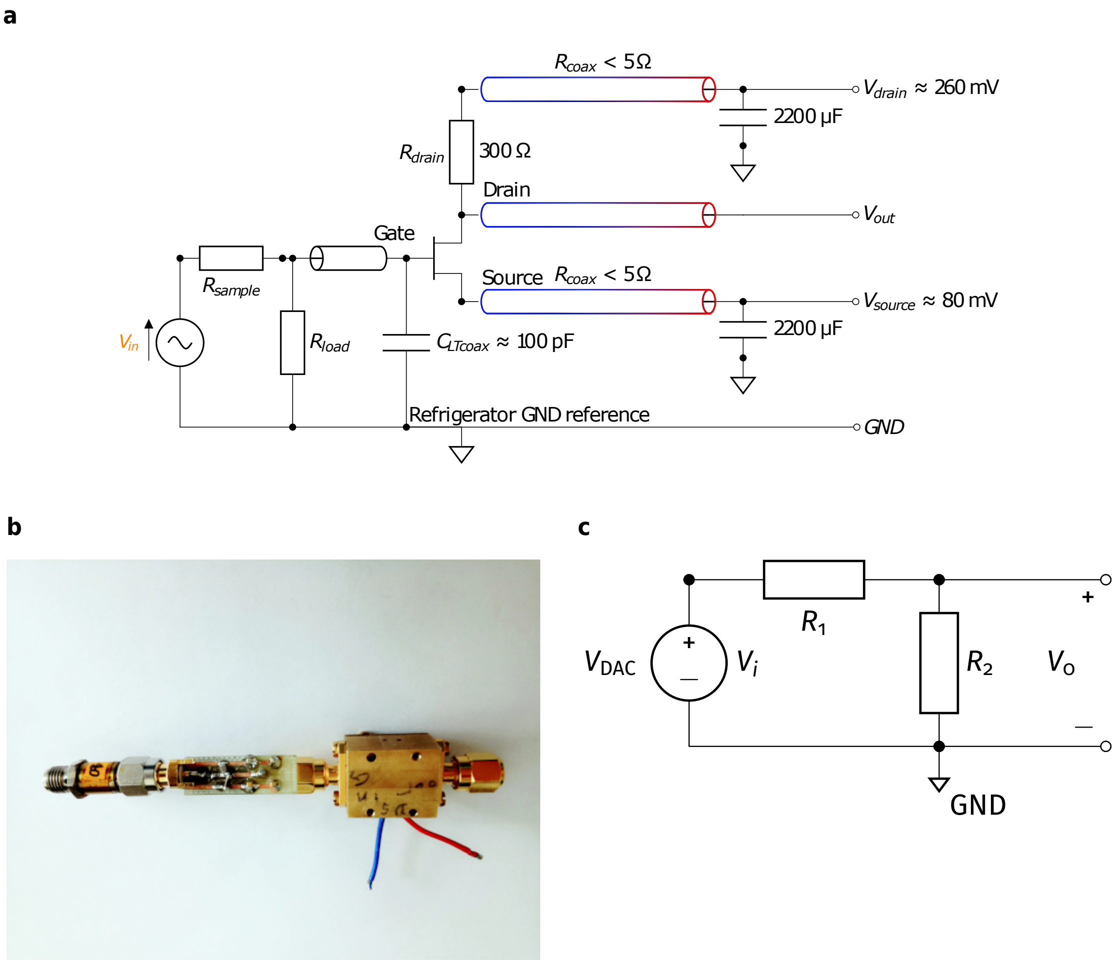

**Figure 4.8. | Low Noise HEMT Ampflifier. a**, HEMT amplifier circuit diagram. An attenuated input voltage is injected to the sample. A load resistor forming a voltage divider with the sample acquires a part of the sample voltage. The voltage on the load resistor is then sensed at the gate of the polarized HEMT amplifier. The HEMT amplifier is connected to room temperature using low-resistance coaxial lines (gradient from 1 K blue to 300 K red). $V_{drain}$ and $V_{sourse}$ are the filtered polarization voltages with respect to GND, $V_{out}$ the output signal. **b**, HEMT low temperature amplifier. The Signal is injected from a cold attenuator -40 dB to the device under test. The test device is a PCB with a resistive divider $R_{sample} = 10\,\mathrm{k}\Omega$, $R_{load} = 4.7\,\mathrm{k}\Omega$ and a capacitance $C_{coax} = 150\,\mathrm{pF}$ resembling the coaxial cable from the cold finger to the amplifier mounted at the higher temperature stage here 1K. **c**, Polarization voltage divider of the low temperature amplifier setup. A DAC voltage is applied to a voltage divider (Vishay precision Z foil resistors). $V_{drain}$ a division of 10:1 $R_1 = 1\,\mathrm{k}\Omega$, $R_2 = 100\,\Omega$, and 50:1 for $V_{source}$ $R_1 = 5\,\mathrm{k}\Omega$, $R_2 = 100\,\Omega$. The set voltage is then filtered with a capacitor combination $C_{filter} = 2200\,\mu\mathrm{F}$ using electrolytic and ceramic capacitors.

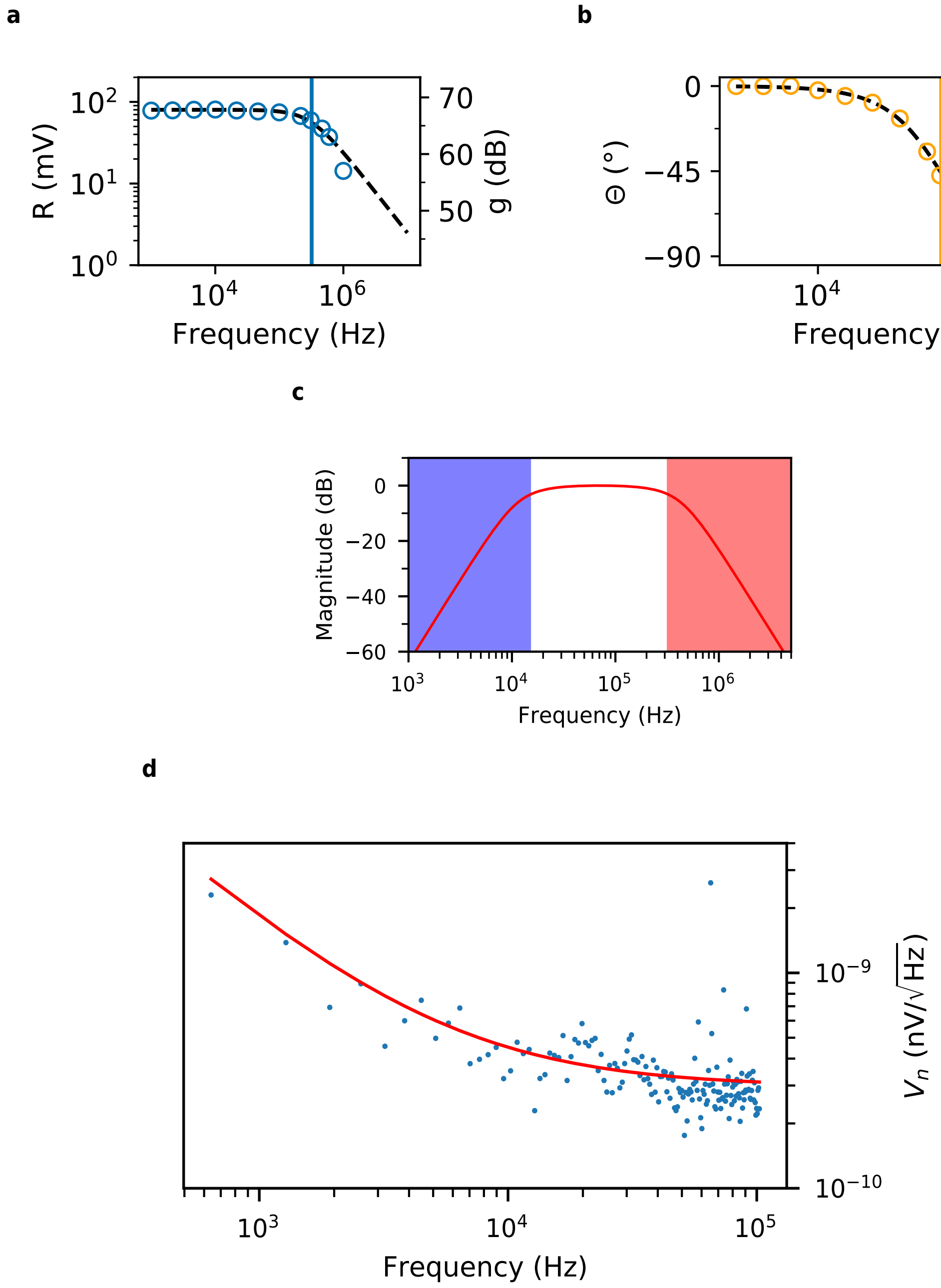

**Figure 4.9. | Noise spectral density of the amplifier chain.** **a**, HEMT low temperature amplifier bandwidth Magnitude *R* measured with the lock-in amplifier. **b**, HEMT low temperature amplifier phase relation *Θ* measurement. **c**, Combined pass band of the bias tee's stop band (SHF BT40, shaded blue) and the HEMT amplifier stop band (shaded red). **d**, HEMT low noise preamplifier noise spectral density at 4K.

tric close to the resonator lines lead to randomly changing energy-relaxation times of superconducting qubits[96]. Random individual charging and discharging of defects in the gate dielectric of a field effect transistor device can block or unblock areas of the transistors gate area in a similar way. Two-level systems changing the conductance can give rise to so-called flicker or telegraph noise in the active conducting channel with an $1/f$ frequency dependence[114]. Defects in atomically sharp interfaces of AlGaAs HEMTs are reduced. Using a HEMT with a low defect density and increasing the gate source capacitance $C_{gs}$ to average out fluctuations can to this end reduce the noise level of a cryogenic pre-amplifier down to $200\,\mathrm{pV}/\sqrt{\mathrm{Hz}}$[84]. Material control down to the single defect and ultra low noise cryo-electronic control is one of the outstanding challenges for improving and understanding the operation of solid-state quantum devices. Noise spectroscopy using the cryogenic HEMT connected to a scanning tunneling microscope tip can map out the noise origin on a sub-nanometric scale to investigate for instance high temperature superconductors[12]. The common set-point for operation of the cryogenic HEMT amplifier is at $I_{DS} = 1\,\mathrm{mA}$ and $V_{DS} = 100\,\mathrm{mV}$[51], which allows putting the amplifier even at the 1 K stage of a dilution fridge. We do not see heating effects due to the amplifier in our setup since the power consumption at the operation point is low (order of 100 µW). The low power consumption, low noise and possible high frequency operation is a big advantage compared to other commonly used cryogenic amplifiers. Commercial low noise cryogenic amplifiers working with a similar bandwidth can also be based on SiGe transistor technology[53]. The advantages of SiGe cryo-amplifiers are the possibility to remove common mode noise in a differential configuration a higher gain and the possibile integration into BiCMOS devices[177]. SiGe BiCMOS transistors are to some extent a natural extension of CMOS bringing high-speed signal conditioning to CMOS logic. The drawbacks are that cryogenic SiGe heterojunction transistors do not provide such a low noise and power consumption as

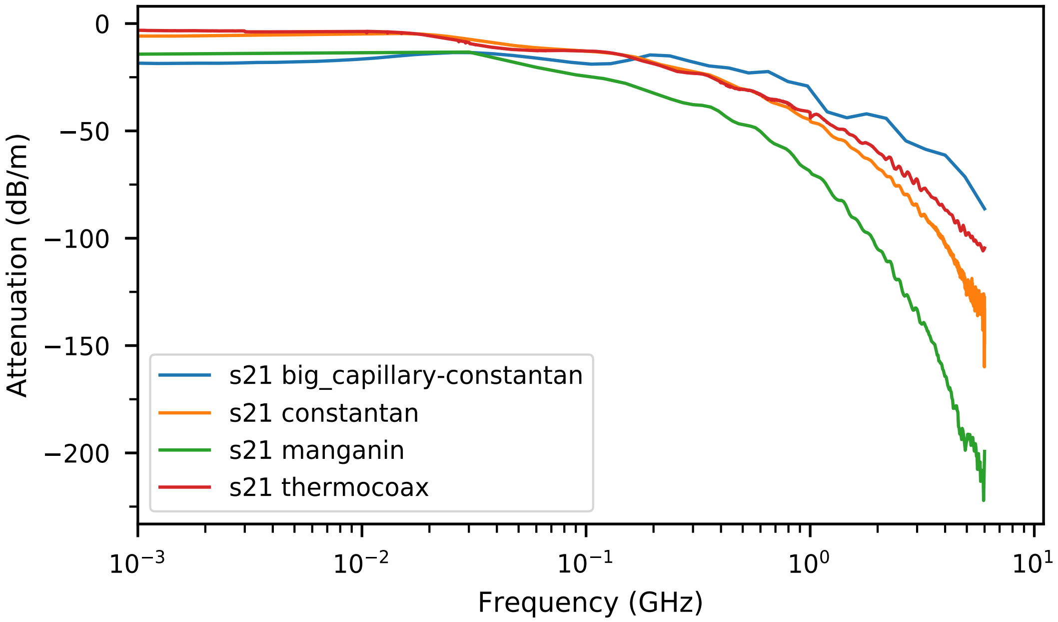

**Figure 4.10. | Test of different coaxial lines at low temperature.** Connection between sample and low temperature amplifier. Transmission measurement of different material combinations and diameters for best transmission and filtering as summarized in table 4.1. Blue curve shows the coaxial constantan wire with diameter $d_c = 70\,\mu\mathrm{m}$ and copper nickel capillary diameter $D_d = 400\,\mu\mathrm{m}$ chosen for the connection.

the GaAs HEMT devices tested here. Power, noise and bandwidth considerations can be first steps towards building a cryogenic controller for quantum hardware[10].

The low noise HEMT amplifier is used to detect voltage fluctuations at a load resistance close to the sample. The schematic of the amplifier setup is shown in figure 4.8. An input voltage is injected to the device under test using a cold attenuator of $-40\,\mathrm{dB}$ shown in figure 4.8b. A load resistor forming a voltage divider with the sample under test acquires a part of this voltage. The voltage on the load resistor is then sensed at the gate of the polarized HEMT amplifier. The HEMT amplifier is polarized using the DAC where $V_{drain}$ and $V_{sourse}$ are the filtered polarization voltages with respect to GND. A DAC voltage is applied to a voltage divider (Vishay precision Z foil resistors) with a division of 10:1 $R_1 = 1\,\mathrm{k}\Omega$, $R_2 = 100\,\Omega$ at $V_{drain}$, and 50:1 $R_1 = 5\,\mathrm{k}\Omega$,

$R_2 = 100\,\Omega$ at $V_{source}$ as depicted in figure 4.8c. The set voltage is then filtered with a capacitor combination $C_{filter} = 2200\,\mu\text{F}$ using electrolytic and ceramic capacitors. The HEMT amplifier $V_{out}$ is connected to room temperature using low-resistance coaxial lines (gradient from 1 K blue to 300 K red). Figure 4.9d shows the measurement of the voltage noise spectral density down to a white noise level of $0.2\,\text{nV}/\sqrt{\text{Hz}}$ using a cold attenuator at the input. The cryogenic amplifier then connects to a room temperature amplifier (NF SA421-F5) with a white noise level of $0.7\,\text{nV}/\sqrt{\text{Hz}}$ measured in figure 4.9d. The load circuit with an impedance in the range of the resistance quantum $R_K = 12.9\,\text{k}\Omega$ sets the gain bandwidth and with that the baseband for the measurement of the incoming high frequency signal. The load circuit and the amplifier noise spectrum are characterized at a liquid Helium temperature as shown in figure 4.8. The black dashed line shows a simulation of the data with the approximate parameters of the sample and the load circuit: $R_{sample} = 10\,\text{k}\Omega$, $R_{load} = 4.7\,\text{k}\Omega$, $C_{CoaxToAmp} = 150\,\text{pF}$. The sample and load resistors $R_{sample} \approx 10\,\text{k}\Omega$ and the coaxial cable needed to connect from the load resistance to the amplifier form an RC filter with a 3dB cut-off frequency 320 kHz (marked as a vertical blue line in figure 4.9a). This limits the upper operation frequency of the amplifier chain to approximately 300 kHz. The resulting combined pass band consisting of the stop band of the bias tees (SHF BT40) and the amplifier stop band is plotted in figure 4.9c. To optimize the pass band, we fabricated several low temperature coaxial lines and tested the connection from the PCB board directly to the low temperature HEMT amplifier. The connection between the sample and the higher temperature ultra low noise amplifier at 1 K should be thermally isolated. The bandwidth of the device under test connected to the amplification chain is then limited by the capacitance of this coaxial line. Figure 4.10 shows the transmission behavior for different inner conductor materials and capillary diameters. The measurement of the transmission of the different coaxial lines is shown in figure 4.10. The coaxial line (blue line in figure 4.10) with the highest kHz impedance $\lim_{\omega \to 0} Re(Z(\omega))$ for ther-

| Conductor | Dielectric | $d_c$ | $D_d$ (µm) | $\epsilon_{eff}$ | $L$ (m) | $R$ ($\frac{\Omega}{\mathrm{m}}$) | $A$ ($\frac{\mathrm{dB}}{\mathrm{m}}$) | $C$ ($\frac{\mathrm{pF}}{\mathrm{m}}$) |
|---|---|---|---|---|---|---|---|---|
| Constantan | Air | 100 | 200 | 3.2 | 0.58 | 63.8 | -138 | 259 |
| Thermocoax | $Al_2O_3$ | 150 | 200 | 2.1 | 0.56 | 50.5 | -111 | 402 |
| Constantan | Air | 70 | 400 | 2.4 | 0.29 | 252.4 | -86 | 76 |
| Manganin | Air | 100 | 200 | 3.7 | 0.30 | 189.8 | -210 | 295 |
| Manganin | Capton | 100 | 400 | 2.6 | 0.29 | 193.8 | -69 | 103 |
| Manganin | Capton Grease | 100 | 400 | 3.4 | 0.29 | 193.8 | -69 | 135 |

**Table 4.1. | Coaxial cable design for low temperatures.** Connection between sample and low temperature amplifier. Measured values for different types of tested low temperature coaxial lines. Tested were different conductor alloys, diameters, dielectrics and different diameters of the copper-nickel shielding tubes. All shielding tubes were semi-rigid copper-nickel, the connectors for the tests were standard SMA connectors adding around 10 pF each.

mal isolation but good transmission properties at higher frequencies due to the low capacitance per meter is chosen with a constantan core diameter of $d_c = 70\,\mu\mathrm{m}$ and a copper-nickel capillary diameter of $D_d = 400\,\mu\mathrm{m}$. The amplifier has a flat gain up to 300 kHz measured at 4 K using the constantan coaxial line. The other material combinations tested for building a low temperature coaxial line are summarized in table 4.1.

Alternatively, the sample load can be implemented in a resonator circuit to acquire signals at higher frequencies in the MHz range[12,49]. In our case, the high frequency voltage signals propagating through the quantum conductors are already converted down at the sample level before entering the HEMT amplifier input to a base-band signal (inside the pass band $\approx 100\,\mathrm{kHz}$). The base-band signal in our setup is acquired at a flat phase pass band of the amplifier chain as measured in figure 4.8b. We amplify the base-band signal at the modulation frequency $\omega_{LI}$ then by a second stage amplifier (NF SA-421-F5) at room temperature. The second stage amplifier's output signal is finally digitized using a homodyne detection (DSP lock-in 7280). The next chapter introduces the high frequency part of the cryogenic pulse control setup.

*"The noise is the signal."*

– Rolf Landauer

# 5

# ULTRA-FAST PULSE CONTROL AT CRYOGENIC TEMPERATURES

High frequency pulse control for embedded devices at cryogenic temperatures is a major challenge for coherent quantum operation. Important parts of the setup for high frequency pulse control together with sampling at cryogenic temperatures developed during this thesis are presented in the following. I start to introduce the thermal radiation limit given by the black body spectrum and the line attenuation. Then I describe and characterize several low pass filtering techniques. Optimized filtering can then lead to a noise limit dominated by the lowest temperature stage. In the following, I outline transmission line design rules for cryogenic temperatures starting with coaxial lines, connectors, down to the sample holder together with the PCB. The RF setup is then characterized in transmission. After the bandwidth characterization, I describe ultra-fast sampling at cryogenic temperatures 20 mK and analyze phase drifts of the Fourier components of the produced pulse train. Finally, I present time-resolved measurements of an electron wave packet. These measurements have been made possible by combining all the technical development realized during the PhD project.

## 5.1 CRYOGENIC QUANTUM ELECTRONIC SETUP

Examples of quantum-enabled devices used at low cryogenic temperatures well below 1 K include single electron tunnelling devices[187], superconducting qubits[48], single atom[125] and molecular[32] devices and spin systems[7]. Low temperature operation is also a requirement for phase-coherent measurements of electron wave packets. It is important to keep both the thermal excitations and the noise at the quantum electronic device under test as low as possible. Therefore, the sample is mounted inside of a dilution refrigerator where the temperature at the sample level can be well controlled and cooled down to the order of 10 mK. Low-temperature electronic measurements need optimized thermalization to limit the needed cooling power and additionally, noise filtering of the input signals[165]. The Wiedemann-Franz law tells us that the ratio of thermal and electrical conductivity is proportional to the temperature. Thus, conducting interconnects must be electrically lossy, limiting the bandwidth and power carrying ability, in order to keep a good separation between room temperature and the cryogenic device temperature[44]. Thermal power management also implies that injecting signals using conducting lines down to low temperatures is always a compromise between attenuation, filtering and thermalization. Engineering a thermal noise limit of a cryogenic setup is particularly important for larger scale quantum hardware[99], where large scale means that it involves many different functional, power consuming units to be cooled. Consequently, guide lines of cryogenic quantum engineering are discussed.

The lower limit of thermal noise in interconnection lines, DC and RF, is estimated using thermal Johnson-Nyquist noise and Planck's law of radiation in order to minimize the noise and thermal radiation inside the cryostat[67,120]. The low frequency (DC) noise limit of a resistive element at temperature $T$ is given by the Johnson-Nyquist noise defining the variance of (current) signal fluctuations at the resistor $R$ as:

$$\left\langle (\Delta i)^2 \right\rangle = 4k_B T \cdot B/R, \tag{5.1}$$

where $B$ is the detection bandwidth.

The high frequency limit of the noise spectrum is determined by thermal noise inside a closed transmission line. A transmission line can be described as a black body radiator going from a hot temperature to the base temperature with no additional input radiation. Planck's law describes the spectral density of electromagnetic radiation $\rho$ emitted by a black-body at thermal equilibrium at given temperature $T$ as:

$$\rho(\omega, T)\mathrm{d}\omega = \frac{\hbar\omega^3}{\pi^2 c^3} \frac{1}{\mathrm{e}^{\frac{\hbar\omega}{k_B T}} - 1} \mathrm{d}\omega, \tag{5.2}$$

where $c$ is the speed of light (cf. table A.2). Planck's radiation law gives a continuous energy density spectrum of oscillating modes with frequency $\omega$, where each mode has quantized energy. The occupation $\overline{n}(E)$ of the thermal modes at equilibrium is bosonic and follows Bose-Einstein statistics:

$$\overline{n}(E) = \frac{1}{\mathrm{e}^{\beta(E-\mu)} - 1}, \tag{5.3}$$

with $\beta = 1/k_B T$ and the chemical potential $\mu$. The thermal radiation in a line from the hot, room temperature environment down to low cryogenic temperatures needs to be attenuated. The required frequency dependent attenuation factor $\mathcal{A}(f)$ obtained by

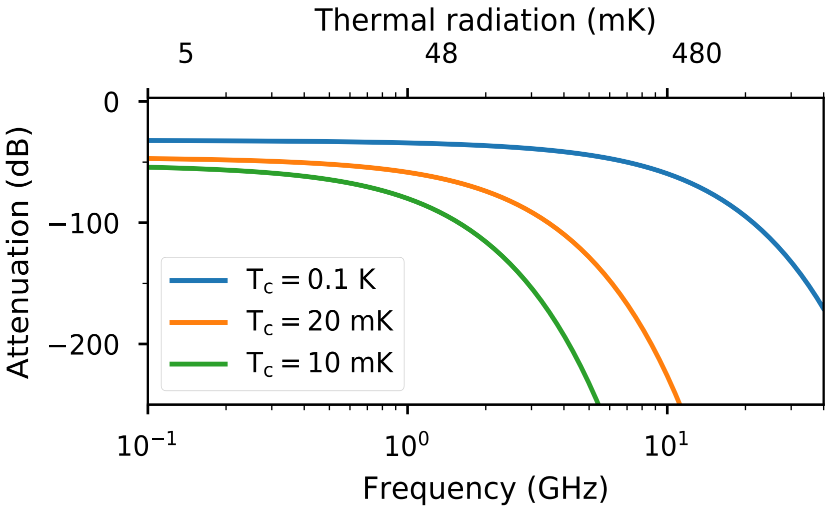

**Figure 5.1. | Thermal noise limit of a cryogenic quantum measurement setup.** Thermal radiation and attenuation. Black-body spectrum with attenuation and low-pass filtering for mK cryogenic fridges. A closed fridge with a black body spectrum thermalized at 4 K is assumed. The continous lines correspond to the required attenuation to reach a cold black body spectrum of at 100 mK (blue), 20 mK (orange), 10 mK (green).

filtering of the lines between different temperature stages can be estimated[67] using an occupation ratio of bosonic modes (5.3):

$$\mathcal{A}(f) = \frac{\mathrm{e}^{\frac{hf}{k_B T_h}} - 1}{\mathrm{e}^{\frac{hf}{k_B T_c}} - 1}, \tag{5.4}$$

where $T_c$ is the corresponding cold temperature stage of the experiment and $T_h$ is the hot side source radiation to be attenuated.

Thermal radiation at a frequency of $f = 10\,\mathrm{GHz}$ already corresponds to a temperature of the electronic system of approximately $T_{el} = \frac{hf}{k_B} = 480\,\mathrm{mK}$. Accordingly, high frequencies from a black body spectrum at higher temperatures need to be (low-pass) filtered when going to a lower temperature stage. Whereas, a cold cryogenic environment of $T_c = 100\,\mathrm{mK}$ requires only a moderate attenuation of $-44\,\mathrm{dB}$ starting from $T_h = 4\,\mathrm{K}$, the requirements get more restricted at a low temperature like $T_c = 10\,\mathrm{mK}$, as shown in figure 5.1. Then, a low-pass filter of several $-100\,\mathrm{dB}$ of attenuation is needed starting already in the gigahertz range up to the infra-red. If the implementation of low-pass filtering is adequate, the cold stage is only weakly affected by the black-body radiation of the hotter temperature stages[165]. An ideal **low-pass filter** for low temperature quantum measurements:

*absorbs all high frequency radiation in the vicinity of the conductor using for instance an effective (metallic) absorber so that no millimeter or micrometer wavelength radiation can propagate.*

There are several possibilities to implement effective low-pass filtering in cryogenic quantum measurement setups: Metallic powder or ECCOSORB filters[123], silver epoxy filters[151], circuit boards with surface mount components like the commercially available QDevil filter box[101] or Ion trap cryogenic low pass filters (Stahl electronics Type KA-Fil 2a[159]) and also resistive thermocoax lines[28] are commonly used[8]. A good low-pass filter can for example be made, when wires are embedded in insulating capton tape and fixed tightly applying pressure between two flat gold plates in order to remove the space for free wave propagation. A very similar filtering effect exists if the shielding capillaries of the conducting lines are tightly squeezed. The squeezing of the absorbing metal shielding removes the free space for wave propagation and can give a high attenuation of $-150\,\mathrm{dB}$ per $50\,\mathrm{cm}$[67]. We apply a combined filtering technique in the setup for the DC wires as shown at the squeezed copper shielding tube in figure 5.5a. Second, all wires are put in a copper nickel tube which is filled with a two part castable silicone load absorber (ECCOSORB CRS-117). The ECCOSORB filter then corresponds to a high frequency attenuation of around $-100\,\mathrm{dB}$ per meter[116] starting from gigahertz frequencies measured in figure 5.2b. Along with heavy low-pass filtering around $-60\,\mathrm{dB}$ of broadband filtering is useful to come close to the black body radiation limit below $20\,\mathrm{mK}$. The noise temperature directly gives a guide line how to distribute the attenuation over the different temperature stages as described subsequently.

## 5.2 CRYOGENIC SETUP, AMPLIFICATION AND NOISE

The spectral voltage noise density limit of a cryostat with attenuation $-20\,\mathrm{dB}$ at $10\,\mathrm{mK}$, $-10\,\mathrm{dB}$ at $1\,\mathrm{K}$, $-10\,\mathrm{dB}$ at $4\,\mathrm{K}$ and $-20\,\mathrm{dB}$ at room temperature is depicted in figure 5.2. The thermal occupation shows in particular that well-dosed attenuation and filtering of lines[116] between the different temperature stages is important to keep a low temperature and a low noise level in a cryostat. Additionally to the filtering described above, a surface mount RC filter stage for all DC lines (with $R = 1.2\,\mathrm{k}\Omega$ and $C = 47\,\mathrm{nF}$) on a thin Kapton PCB is thermalized inside a gold-plated, shielded case as shown in figure 5.2. The filter stage is then fixed at the cold mixing chamber plate of the refrigerator. Finally, all DC lines can additionally be filtered close to the sample chip using surface mount components. The last filtering can be sample-specific and directly at the PCB carrying the device under test. The careful filtering procedure shows that low-temperature cryogenics goes along with a big effort in engineering to access quantum effects at low temperatures.

In the following I go from the DC part to the higher radio frequencies (RF). Coaxial RF lines are used to inject quantum-controlled high frequency radiation. Figure 5.1 suggests that a broadband attenuation of above $-50\,\mathrm{dB}$ is useful to attenuate thermal radiation of higher temperature stages to lower stages. The signal to noise compromise for RF line filtering is frequently to attenuate the signals with around $-60\,\mathrm{dB}$ distributed over each RF line to reach a single photon level in quantum electrodynamics experiments[20]. By choosing an attenuation of $-60\,\mathrm{dB}$ one ensures on the one hand that the thermal occupation of photons is attenuated and of the order of $10^{-3}$ at the sample level. On the other hand, it is still possible to input power using standard

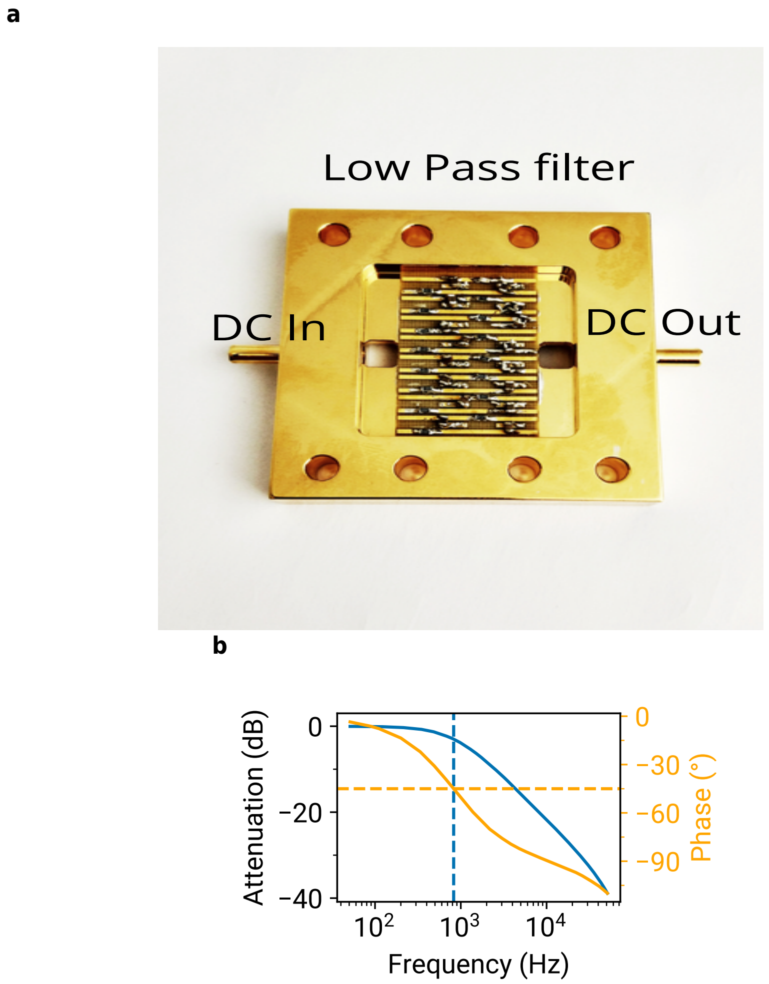

**Figure 5.2. | Cryogenic low pass filtering.** **a**, Filter box with screw holes to fix at a cold plate. A PCB with surface mounted components ($R = 1.2\,\mathrm{k\Omega}$ $C = 47\,\mathrm{nF}$) soldered on strip-lines thermalized at the mixing chamber plate. **b**, Measured filtering characteristics. Blue curve attenuation of two DC lines interconnected at the cold sample chip. Orange curve frequency dependent phase shift. Dashed lines indicate the -3dB point at the cut-off frequency of $825\,\mathrm{Hz}$.

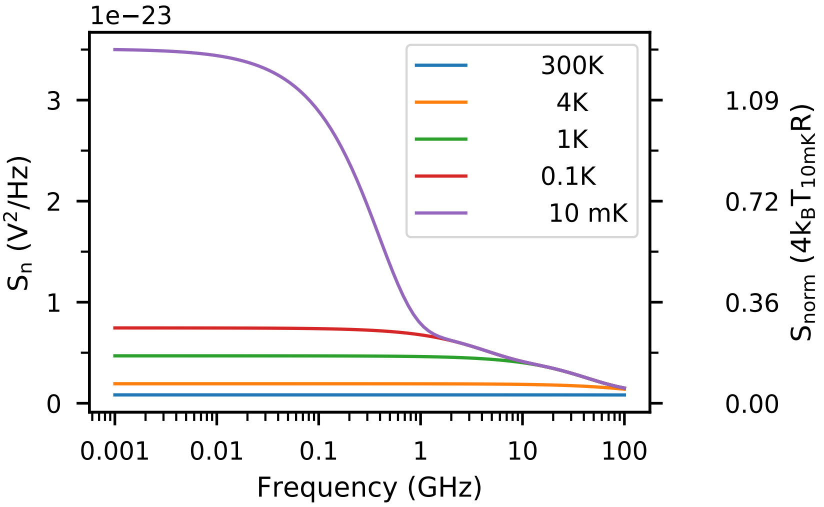

**Figure 5.3. | Thermal noise limit of a cryogenic transmission line.** RF line attenuation and thermal limit of the spectral noise power density. Broad-band attenuators of (-20, -10, -10, -20) dB distributed at (4, 1, 0.1, 10m) K.

microwave sources from room temperature. The thermal noise inside of a cryogenic cryostat should in the end be close to the Johnson-Nyquist noise limit of the transmission line at base temperature. This lower thermal noise limit of the coaxial RF lines attenuated at the different temperature stages $T_n$ can be calculated using equation 5.1 and 5.2[120]:

$$S_n = \sum_k A_k \cdot R_k^2 \cdot \left\langle (\Delta i)^2 \right\rangle \cdot \rho(\omega, T_k), \tag{5.5}$$

with the attenuation $A_k$ and resistance $R_k$ ( left axis $R_k = 50\,\Omega$; $R_k$ is a normalization constant on the right axis) at the temperature stage $T_k$. In this case the $-60\,\mathrm{dB}$ are distributed over four stages using attenuators of (-20, -10, -10, -20)dB at (4, 1, 0.1, 10m) K. The noise summed over all temperature stages using $-60\,\mathrm{dB}$ raises in this case the noise temperature at base temperature to around 13 mK (shown as purple line in figure 5.2 at $T_c = 10\,\mathrm{mK}$).

High frequency operation is essential for fast quantum control and optimized fidelity. The next section describes the transmission line design.

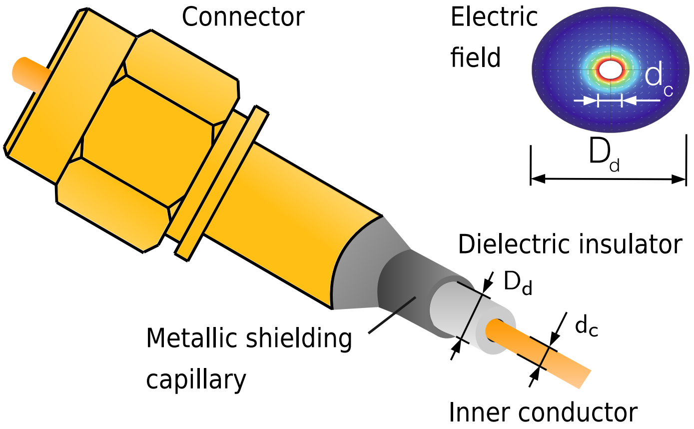

**Figure 5.4. | Coaxial line.** Coaxial line with inner conductor, shielding capillary, dielectric and connector. Top right field profile simulated using COMSOL[43].

## 5.3 CRYOGENIC MICROWAVE ENGINEERING

A low-loss, high frequency transfer of data using fast interconnects at low temperatures is needed for implementing quantum communication beyond the chip-scale in a solid-state quantum information processor. Subsequently the main improvements of the high-frequency parts of the setup are outlined. High-frequency radiation in cryogenic measurement setups is frequently transmitted using coaxial RF lines. Coaxial lines consist out of a connector, a metallic shielding capillary often a stainless steel tube, a dielectric insulator and an inner conductor wire as shown in figure 5.4. Important parameters of a coaxial line like the impedance $Z_0$, the cut-off frequency $f_c$ and the capacitance $C$ can be described via[139]:

$$Z_0 = R = \frac{1}{2\pi}\frac{\mu_0\mu_r}{\epsilon_0\epsilon_r} ln\left(\frac{D_d}{d_c}\right) \tag{5.6}$$

$$f_c = \frac{c}{\pi\left(\frac{D_d+d_c}{2}\right)\sqrt{\mu_r\epsilon_r}} \tag{5.7}$$

$$C = \frac{2\pi\epsilon_r}{ln\left(\frac{D_d}{d_c}\right)} \tag{5.8}$$

| Connector type | $D_d$ (mm) | $d_c$ (mm) | Dielectric | Use | Limit $f_c$ |
|---|---|---|---|---|---|
| BNC | $\approx$ 8.1 mm * | $\approx$ 3 mm * | PTFE | Supply voltage | 4 GHz |
| SMA | 4.4 mm | 1.27 mm | PTFE | Gates | 18 GHz |
| Super SMA | 3.5 mm | 1.08 mm | PTFE | Frequency comb | 26.5 GHz |
| K connector | 2.92 mm | 1.27 mm | air | RF lines | 40 GHz |
| Mini SMP | $\approx$ 2.15 mm * | 0.3 mm | air | Sample holder | 65 GHz |
| 1 mm | 1 mm | 0.43 mm | air | Fast scope | 110 GHz |

**Table 5.1. | Coaxial connectors and frequency range.** Engineering specifications for different types and sizes of connectors used during measurements.

using the diameter of the conductor $d_c$, the outer diameter of the dielectric insulator $D_d$ and the dielectric's permittivity $\epsilon_R$. A coaxial cable has an upper frequency cut off above $f_c$ due to wave guide losses to other, non-propagating modes. A transmission line with coaxial profile transmits waves in the dominant transverse electrical (TEM) mode shown as inset in figure 5.4. This TEM mode has a radial symmetric electric field dependence as simulated with COMSOL[43]. The transmission performance of the coaxial cable can be disturbed by the next accessible not radially symmetrical mode ($TE_{11}$)[122] above the high frequency limit $f_c$. Table 5.1 shows different types of connectors used in the measurement setup and their high frequency limit. Currently the RF setup is limited at cryogenic temperatures to around 40 GHz due to the K connector (2.92mm).

The high frequency attenuation of different standard material combinations for coaxial cables including Niobium superconducting coaxial lines measured at low temperatures are published in table 1 of [103]. A recently developed alternative to coaxial cables are superconducting transmission lines on flexible polyacrylamide substrates to connect the 4K stage to the lowest temperature mK stage[47,166]. Flexible superconducting cryogenic interconnects have the advantage that they can be more densely packaged. They also have a low transmission loss and provide a very good thermal isolation. The transmission of the current beta test generation[47] can go up to around 22 GHz.

In our setup we use silver plated stainless steel coaxes (component number: SC-219/50-SSS-SS)[40] with K connectors for the injection lines for having even better high frequency transmission properties. Figure 5.7a shows then the improved transmission through the whole cryogenic setup. The RF lines are connected in a loop configuration from input one over the PCB with a coplanar waveguide chip back to input two. The same transmission loop throughput testing is also performed for the other line combinations. The transmission measurement compares well to the specifications of a 3m long coaxial line (CoaxCorp Part number SC-219/50-SSS-SS)[40]. Figure 5.5 shows the parts of the lowest temperature measurement stage. A 3D cavity for microwaves shown in figure 5.5a is used to shield the sample from unwanted external noisy stray fields. Filtered twisted DC line pairs are glued to the bottom side of the sample holder cavity with silver epoxy for good thermal anchoring. The twisted pairs are then soldered to golden spring-loaded pins (solder cup pogo pins). Once the twisted pair lines and the spring loaded-pins are installed, the DC voltages can be applied on the bottom side of the PCB shown in figure 5.5b. Four RF lines are fed from the top part through the cover of the cavity to mini SMP connectors. The printed circuit board, the mini SMP connectors, the RF lines, the RF attenuators and the mounting of the sample are specifically microwave-engineered for high frequencies up to 40 GHz[6]. Furthermore, all parts are compatible with low-temperature, low-noise quantum measurements and also magnetic fields. The new PCB features eight new DC lines, a better dielectric insulation using a Rogers dielectric (RO4350B) and an improved mechanical crafting quality as shown in figure 5.5b. It is possible to adapt the lines using surface mount components soldered on the PCB (combinations of R, L and C up to 0805 size). The sample holder boards can be produced at a low price. All components and mini SMP connectors are commercial standard components. The rapid prototyping ap-

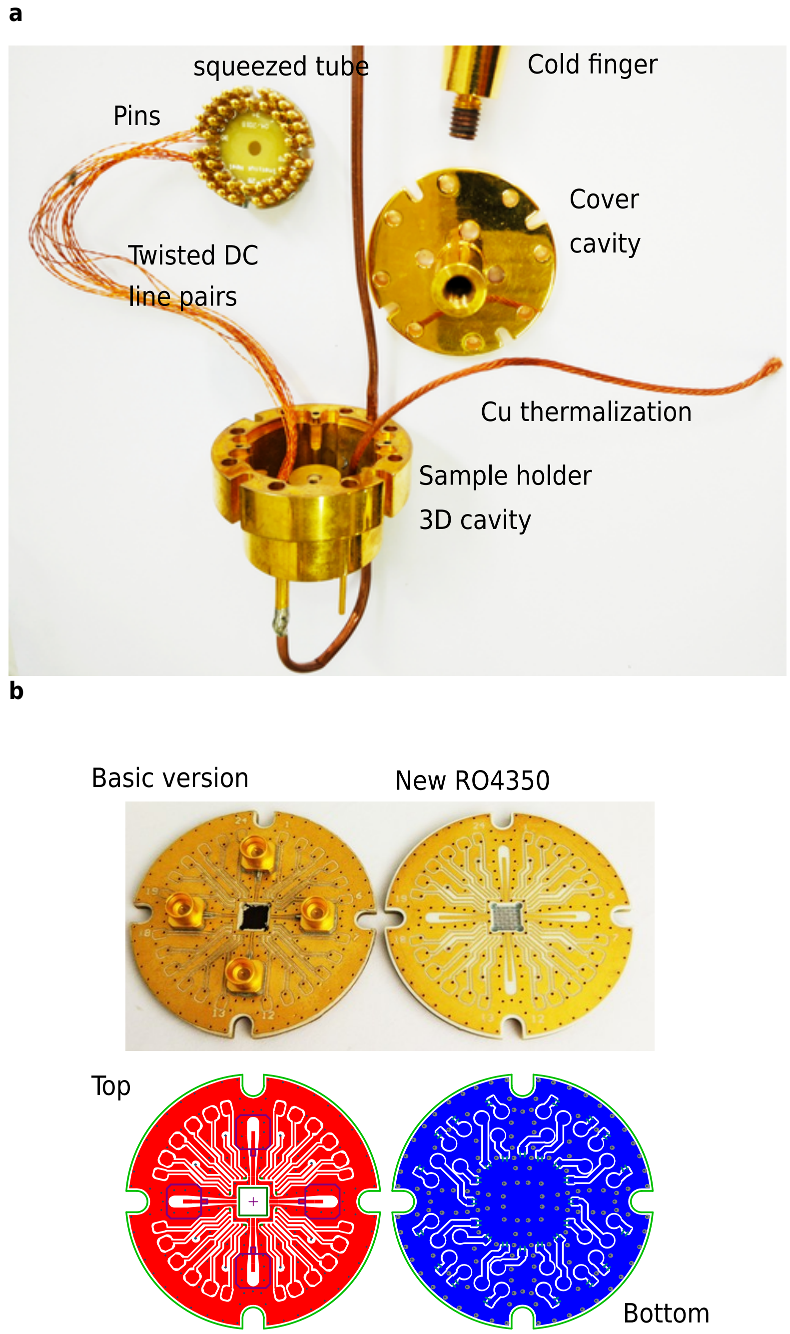

**Figure 5.5. | Cryogenic microwave sample holder. a**, Microwave cavity holder for placing the sample interposer board. Top cover with holes for SMP connectors to inject RF signals. DC lines are fed into the 3D cavity from the bottom using a squeezed copper capillary. They are then thermally anchored using a copper braid and silver epoxy glue. Golden pins with a spring mechanism connect the DC lines to the bottom pads of the pluggable printed ciruit board. **b**, Printed circuit interposer boards. 32 DC lines and 4 mini-SMP connectors for high frequencies. Bottom part top (red) and bottom (blue) layer of Gerber design file for PCB fabrication. Top layer RO4350b dielectric and four waveguides with SMP connectors for RF operation and 24 solder pads. Bottom layer FR4 dielectric for DC lines and 32 solder pad connections for surface mount components.

proach makes it very convenient to test resonator circuits, bias-tees, voltage dividers, and line filters at low temperatures. Simple prototype circuits can be built directly at the sample level on both sides of the PCB chip. A coplanar transmission line with a tapered coplanar waveguide on a GaAs test wafer (from $S_0, W_0 = (125, 200)\mu\mathrm{m}$ to $S_1, W_1 = (10, 10)\mu\mathrm{m}$ as shown in figure 3.2b) is connected to the wave guides on the PCB with up to four bond wires in parallel. The transmission of the new sample holder design and the old is shown in figure 5.7. The resonance at around 18 GHz is due to the SMA to mini-SMP semi-rigid coaxial cable used to connect from the vector network analyzer to the mini SMP connector (cf. table 5.1). Impedance matching, three parallel bond wires and the use of mini SMP and K connectors lead to an improved transmission signal at high frequencies of the new PCB chip.

The main aim is to optimize the sample environment for high frequencies in comparison to the modular interposer PCB approaches based on a FR4 dielectric[42]. The sample holder is well suited for quantum circuit measurements at high frequencies, with similar high frequency capacities as sample holders for superconducting resonator circuits[6].

Additionally, we also also try to keep DC gates and some room for adaptations on the PCB compared to sample holders for superconducting circuits[6]. Future integration of large-scale qubit chips will need very high bandwidth data transfer. We think that the way to widen the input/output data bottle neck could be hybrid opto-electronic technology at the quantum to classical interface. Some examples of the advanced interfacing technology are high-frequency flip-chip bonding[63], cryogenic setups featuring a high number of connections[99], industrial connector types and control at cryogenic temperatures[42]. Possible high band-width connections could be based on spring-loaded multi-coax connectors[144], densely packed spring probe connectors[4] or even higher bandwidth fibre based technology[133]. Figure 4.1 shows a blueprint of the setup with the corresponding temperature stages and filtering.

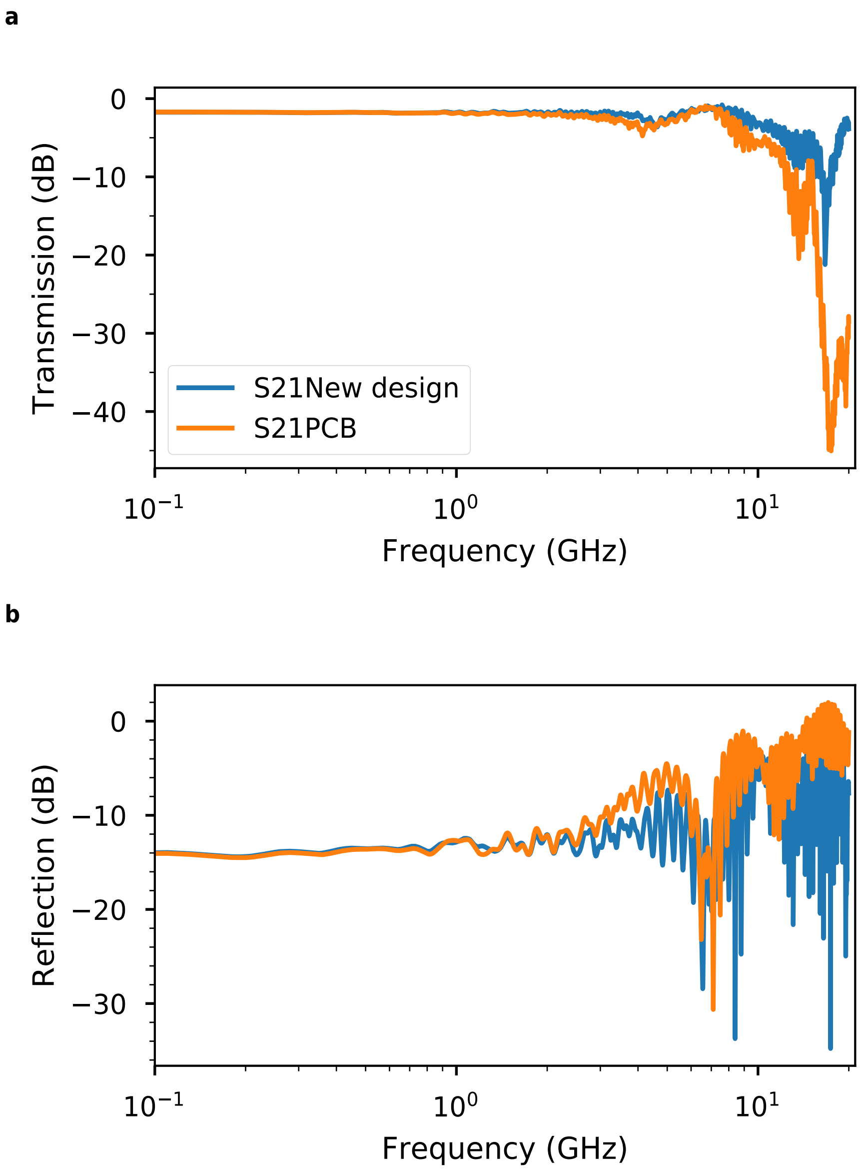

**Figure 5.6. | Transmission of the PCB. a**, RF PCB transmission. Transmission of the PCB using a coplanar waveguide test chip. **b**, RF PCB transmission. Reflection S11 of the PCB using a coplanar waveguide test chip.

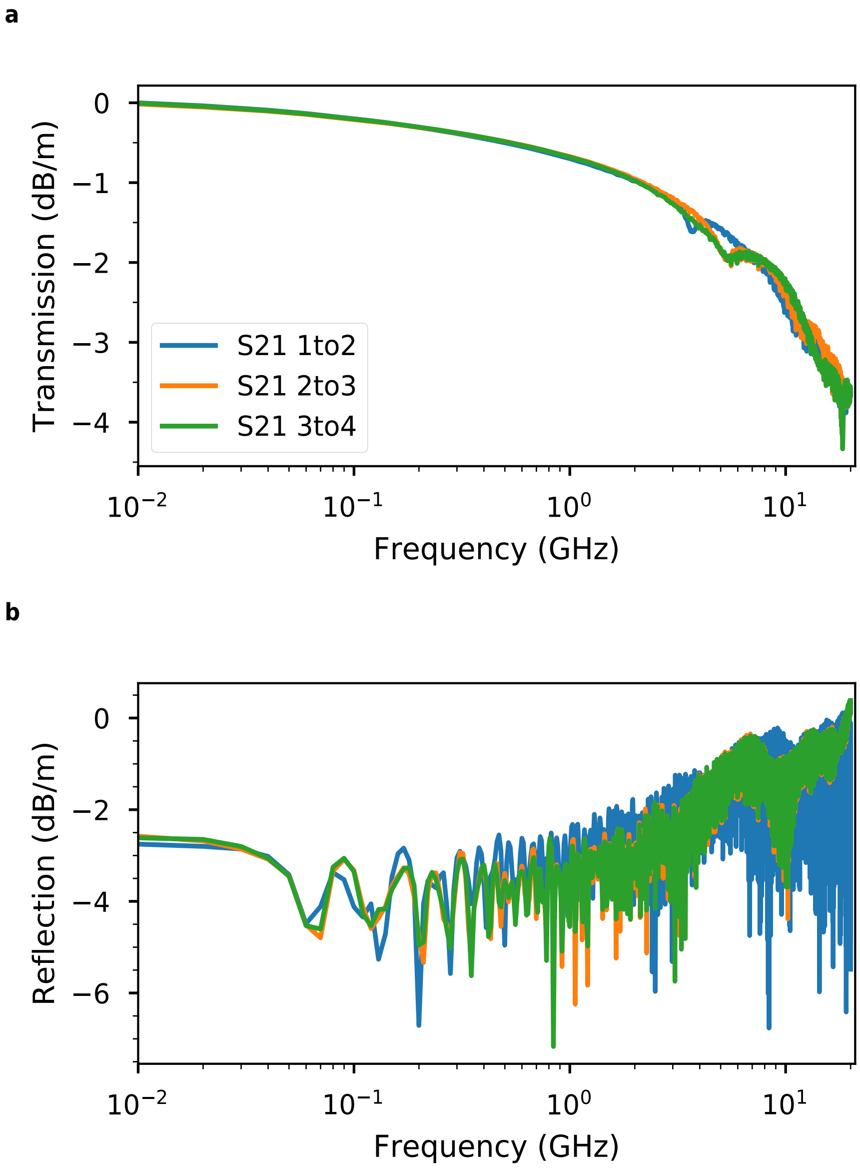

**Figure 5.7. | Transmission of the RF setup. a**, Transmission of the 4 RF lines. SC-219/50-SSS-SS. **b**, Reflection S11 network analysis of the 4 RF lines with a total length of $\approx 6\,\mathrm{m}$. Silver-plated stainless steel coaxial line part number SC-219/50-SSS-SS.

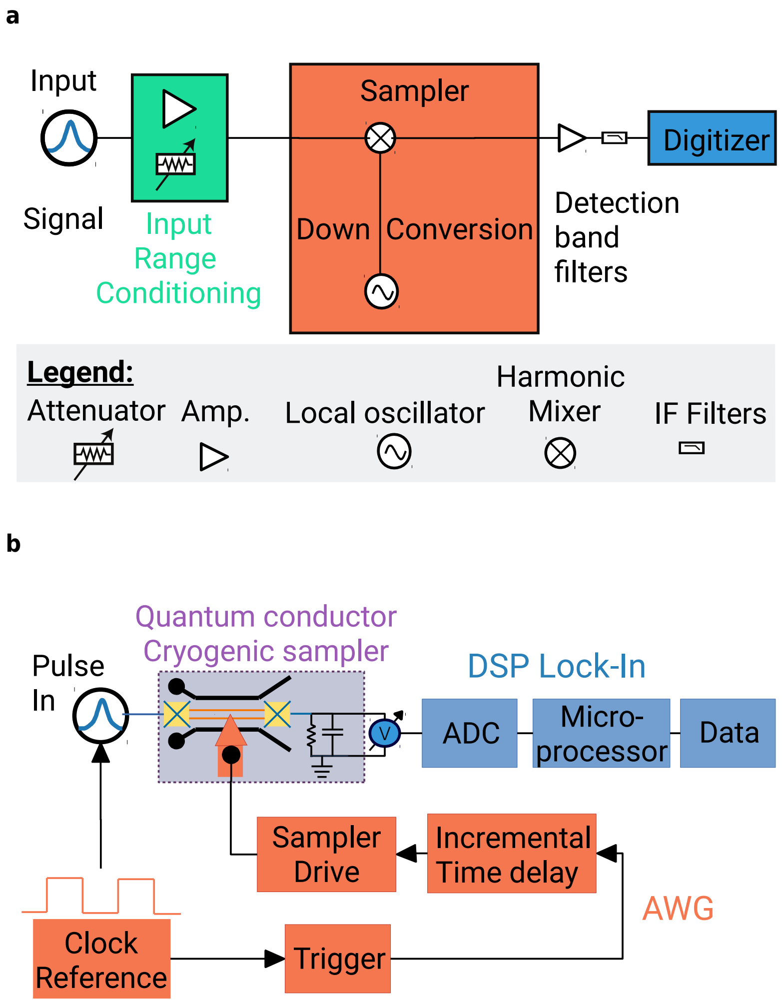

**Figure 5.8. | Sampling setups comparison. a**, Sampling using a down-conversion at room temperature. Intermediate frequency down-conversion using an analog mixer and a local oscillator used in signal analyzers. **b**, Sampling using a point contact at cryogenic temperatures. sampling and synchronization

Signals can be injected as programmable wavelets using an AWG or a frequency synthesizer for Lorentzian-shaped pulses. A DAC is used to apply static voltages and AC voltages up to MHz frequencies. The Input signals are conditioned attenuated, delayed, filtered and combined. Finally all input signals are applied at a shielded quantum device under test. The output voltage is then measured at low temperature and amplified at two stages using a low temperature amplifier (HEMT) and a room temperature amplifier (NF SA512A). The output signal is finally digitized and processed using different possible digital signal processing means. Examples for signal processing would be for instance time-domain ADC traces, frequency spectrum analysis or Lock-In detection. The next section describes the sampling technique for detection of ultra-fast time traces.

## 5.4 SAMPLING AT CRYOGENIC TEMPERATURES

Historically, sampling was developed for data acquisition of signal time traces at room temperature using an oscilloscope. Electronic sampling needs ultra-fast pulses and precise time delays. The high frequency limit of time trace acquisition is achieved by optoelectronic sampling on sub-ps timescales[167]. Optoelectronic voltage sampling uses a pulsed laser striking a photo-conductive semiconductor switch[156] to create pulsers and samplers. The average power of the pump laser for the switch opening (commonly $>$ mW) is a limiting factor for the low temperature operation of ultra-fast light-controlled switches, since the cooling power of a standard dilution refrigerator at the lowest temperature stage (commonly $<$ mW) needs to be sufficient. Thus, we start by investigating voltage-controlled switching at low cryogenic temperature in this project, which is much more power-efficient. In modern sampling oscilloscopes a fast pulse in the pico-second range is generated and used to open and close a fast switch[88] often a Schottky diode bridge. The pulse's energy is used to momentarily turn on the

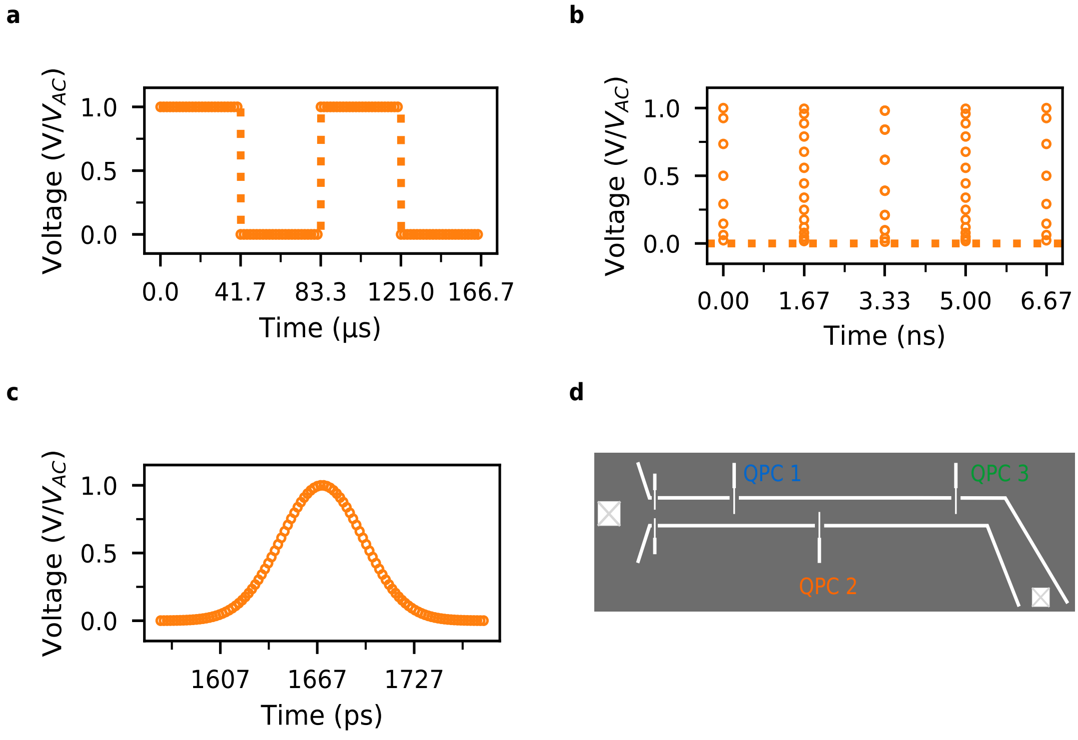

**Figure 5.9. | Sampler drive pulse sequence AWG. a**, Sampler drive square modulation with period $T_{period} = 83.3\,\mu s = \frac{1}{12\,kHz}$. **b**, Pulse repetition on the first half of the duty cycle $T_{rep} = 1.66\,ns = \frac{1}{600\,MHz}$. **c**, Single waveform point (AWG Tekronix 7000 series) resulting in a measured Gaussian sampler drive pulse. **d**, Scheme of the three different sampler QPCs used in the experiment (colors refering to figure 5.14a).

Schottky diode. The ultra-fast sampler and pulser can be integrated into one circuit based on a high frequency material like InP. Sampling detection of signals can in the following be converted to a lower frequency, which is accessible by ADCs. Figure 5.12 shows a scheme of a typical signal analysis. An input signal is amplified or attenuated to a suitable range. Then a sampler is used to convert the high frequency signal to a band where the signal can be digitized using an ADC. An analog signal modulation for down-conversion is used if the input signal is too high in frequency for a direct acquisition. The detection band is formed by a filter and amplification stage directly in front of the ADC.

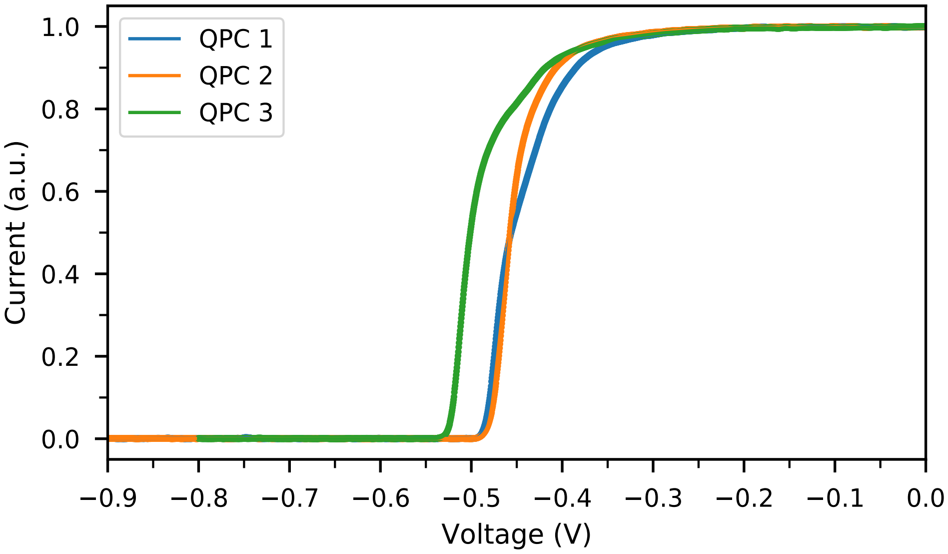

**Figure 5.11. | QPC current to voltage characteristics.** Pinch-off curves of the different sampling point contacts.

Figure 5.8b shows how the sampling is implemented at low cryogenic temperatures. Pulses are injected into a quantum conductor, which can be sampled by opening momentarily an RF QPC switch. The QPC sampler is driven by a time delayed sampler drive pulse produced by an AWG (Tektronix AWG7000 series 24GS/s) as shown in figure 5.9. The sampler drive waveform consists out of single Gaussian pulses shown in figure 5.9c every 1.66 ns (cf. figure 5.9b) using a 12 kHz duty cycle for detection. The sampler drive sequence is modulated at a frequency which can be used for Lock-In detection (12kHz) as shown in figure 5.9a). Figure 5.13 shows how the sharp non-linearity of the QPC IV curve helps to create a high bandwidth sampler. The quantum point contacts have characteristic IV curves as measured in figure 5.11 for the three sampler QPCs. The sampler drive applies a Gaussian pulse with a FWHM of 70 ps as measured in figure 5.13a (e.g. LeCroy WaveExpert 100H). The Gaussian pulse can be detuned by a DC offset using a bias-tee (SHP 65GHz) with respect to the closed position of the quantum point contact ($V_{pinch} \approx -0.5\,\mathrm{V}$). The product of the conduc-

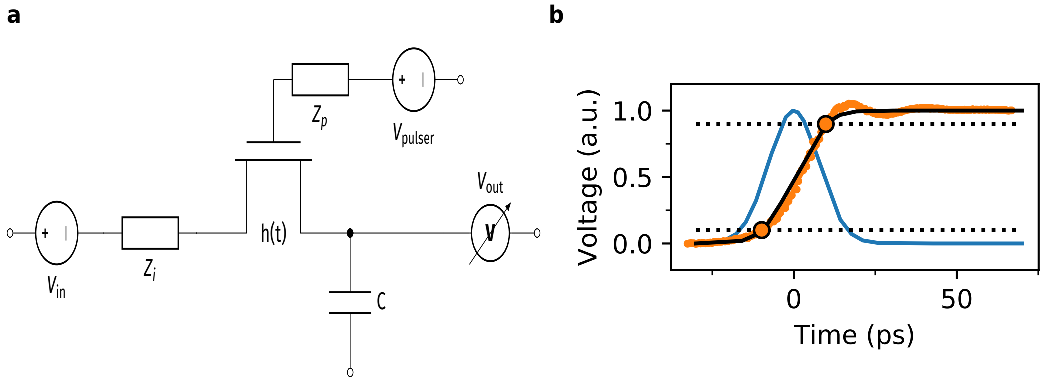

**Figure 5.12. | Sampling switch and rise time. a**, Circuit scheme of a FET sampling switch. **b**, TDR pulser and pulse width. Measured TDR pulse; rise time marked at the 10% and 90% level. Rise time $t_R = (20 \pm 1)$ ps (data points at the crossing with the black dotted lines), unit step (black solid line) and corresponding aperture function (blue solid line) derived from the unit step response of an idealized error function step.

tance function and the Gaussian pulse can be optimized to obtain a sharp conductance fraction shown in red in figure 5.13. Offsetting the pulse with respect to the pinch off of the QPC opens the quantum conductor only on a short time-scale and sharpens the Gaussian pulse. The sampled output voltage $V_{sample}$ of a field effect switch follows the relation[85]:

$$V_{sample}(t) = \int_{-\infty}^{\infty} V_{in}(\tau) h(\tau - t_S)\, \mathrm{d}\tau \tag{5.9}$$

where the input voltage is convoluted by the aperture function $h(\tau)$. The sampling aperture function $h(t)$ is a Dirac delta-like peak in time domain $\lim_{B\to\infty} h(t) = \delta(t)$ only if the sampler has an infinite bandwidth $B$. The naturally limited bandwidth of a sampling switch leads to a broadened aperture function. The aperture's time domain behaviour can be modelled with a transfer function model, which can in the simplest case be a single pole RC filter. Experimentally, the aperture function of a switch $h(t)$ opening at $t_S$ can be found by applying a sharp square pulse step $V_{in}(t) = \Theta(t)$ (Heaviside function):

$$V_{sample}(t_S) = \int_{-\infty}^{\infty} V_{in}(\tau) h(\tau - t_S)\, \mathrm{d}\tau = \int_{-\infty}^{\infty} \Theta(t) h(\tau - t_S)\, \mathrm{d}\tau \tag{5.10}$$

The derivative of the sampled output voltage $V'_{sample}(t_S)$ is given as:

$$\frac{\mathrm{d}}{\mathrm{d}t_S} V_{sample}(t_S) = \frac{\mathrm{d}}{\mathrm{d}t_S} \int_{-\infty}^{+\infty} \Theta(t) h(\tau - t_S)\,\mathrm{d}\tau = h(-t_S), \tag{5.11}$$

leading to the aperture function

$$h(t_S) = \frac{\mathrm{d}}{\mathrm{d}t_S} V_{sample}(-t_S). \tag{5.12}$$

If the voltage amplitude step is smeared out Gaussian-like the time domain spectrum analysis is called time domain reflectometry. The voltage step gets broadened if the rise time of the sampling switch is slower than the injected rising pulse edge. The $10 - 90\%$ rise time $t_R$ of a time domain reflectometer (TDR) step function pulse relates to the bandwidth B of the device under test via:

$$t_R = \frac{4}{\sigma(\omega)} erf^{-1}(0.8) \approx \frac{0.3394}{f_c}, \tag{5.13}$$

where $\mathrm{erf}\,(t)$ is the error function defined in A.6 assuming a system with a Gaussian response. The bandwidth $B$ up to the cut-off frequency $f_c$ can then be estimated using the extracted TDR pulse's rise time via:

$$B \approx \frac{0.35}{t_R}. \tag{5.14}$$

The slowest part (or lowest bandwidth part) of the setup under test dominates:

$$B_{tot} = \frac{1}{\sqrt{1/B_{probe}^2 + 1/B_{osci}^2}} \tag{5.15}$$

the rise time by:

$$t_{R,tot} = \sqrt{t_{Ri}^2 + t_{R_2}^2}. \tag{5.16}$$

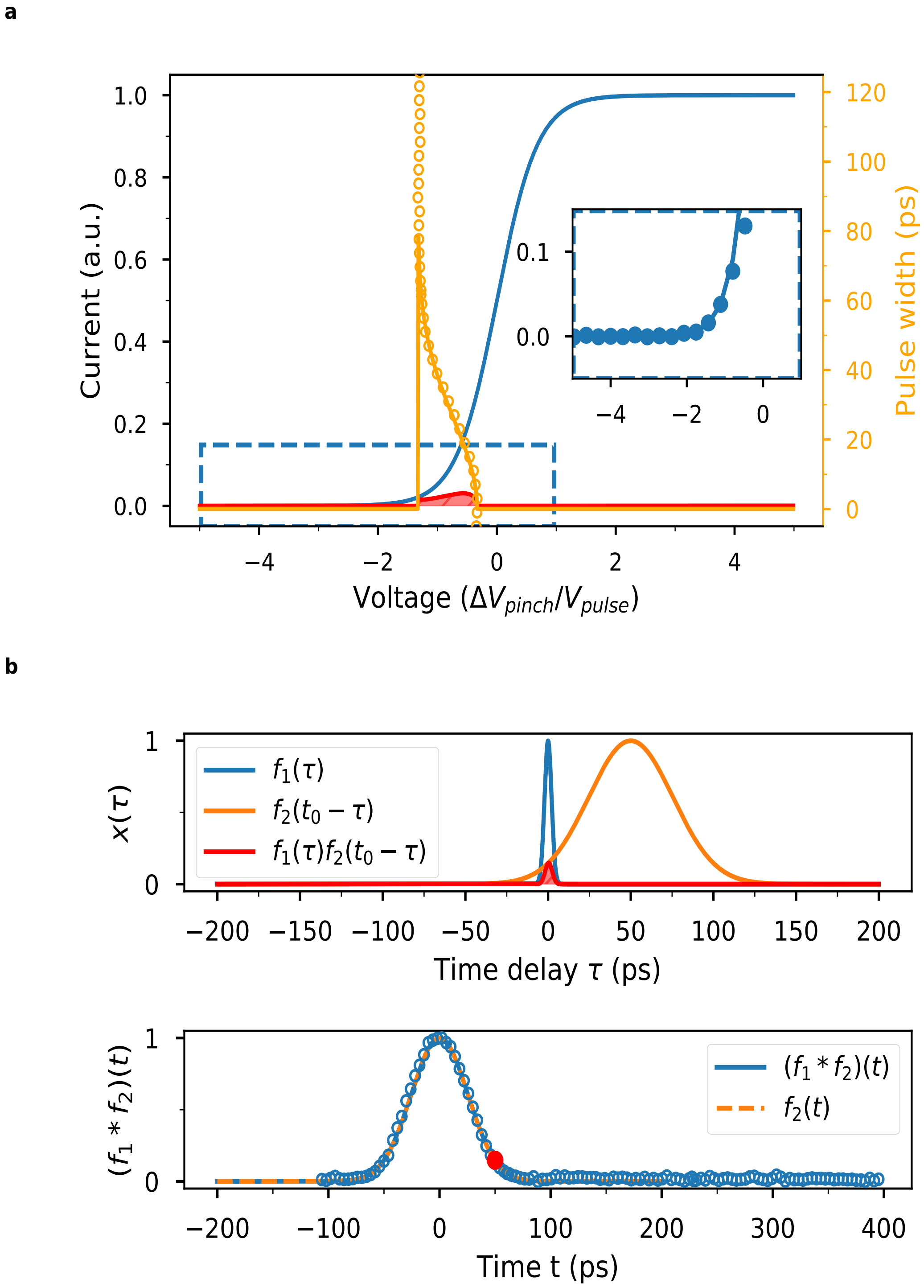

**Figure 5.13. | Pulser setpoint and convolution at QPC sampler.** **a**, The sampler drive pulse (here a Gaussian with FWHM = 60ps) is shifted with respect to the middle of the QPC step function fit by -1.33·$V_{pulse}$ its amplitude. Only the top part of the Gaussian pulse (orange) opens the QPC (blue). Red area shows the product of the pulse and the QPC switch response function, creating an optimized current fraction used for the sampling. Inset: measured QPC current voltage characteristics with pinch-off voltage $V_{pinch} = -0.69\,\mathrm{V}$ in units of the pulser driver amplitude $V_{pulse} = 10\,\mathrm{mV}$. **b**, Convolution $(f_1 * f_2)(t)$ of the incoming pulse $f_2$ and the small aperture pulse $f_1$.

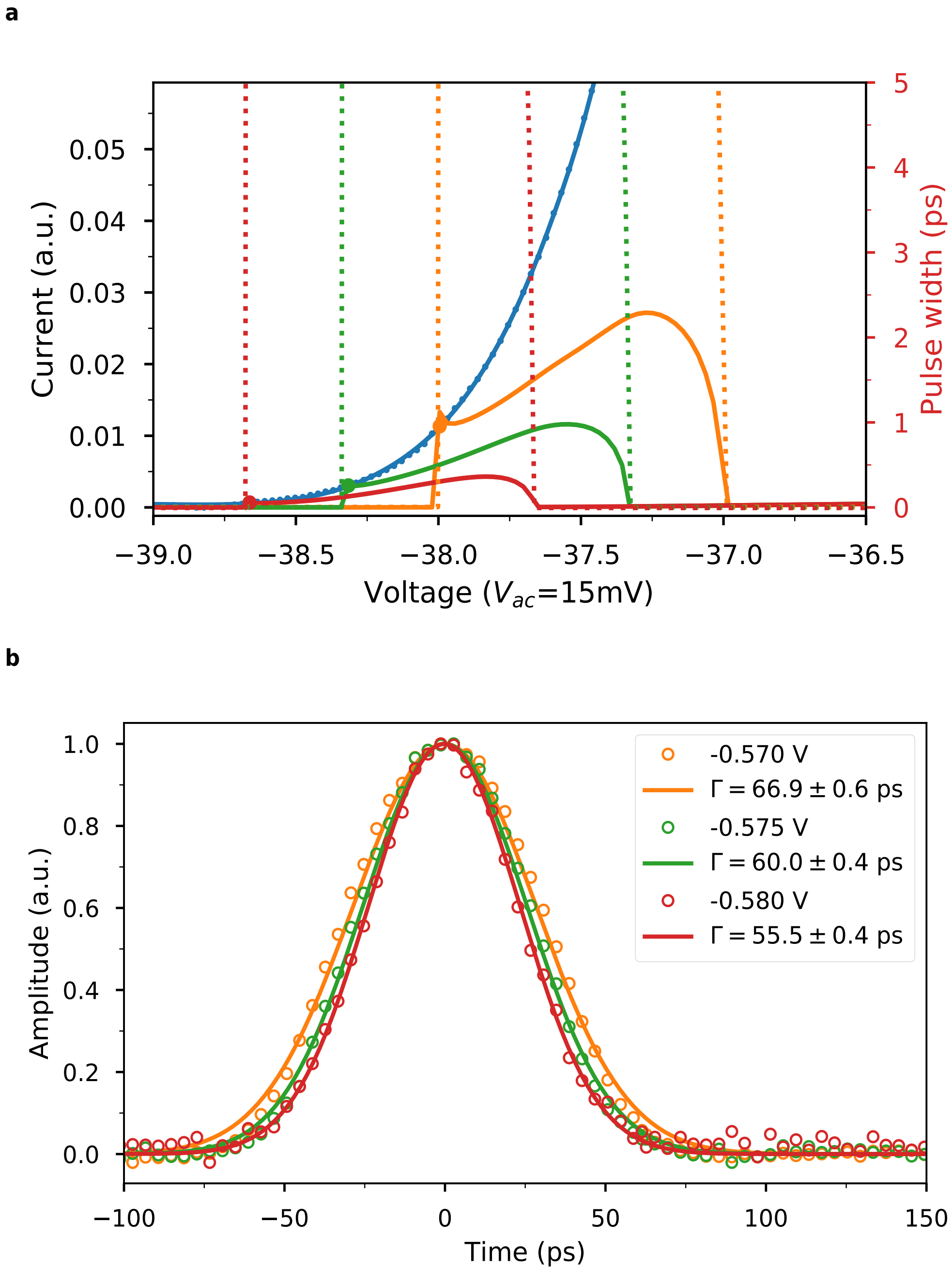

**Figure 5.14. | QPC 1 setpoints and sampled pulse. a**, Measured DC current to voltage characteristics. **b**, Time-resolved Gaussian voltage pulse setting the DC offset more negative to the pinch-off (orange, green red voltage setpoints).

A TDR pulse can also be used to check the transmission line impedance to the sampling switch at low temperatures and to calibrate picosecond time delays. Using the IV non-linearity at an optimized set-point, leads to a sampling which can resolve higher frequencies than the maximum sampling rate of the pulser (AWG 24GS/s). The bandwidth of the sampler is tested at low temperatures and can for example resolve a 24 GHz sine wave or the sharpest Gaussian pulse $\Gamma = 70\,\text{ps}$ we can generate with the AWG. Thus, the analog bandwidth of the QPC switch is very likely exceeding 40 GHz as portrayed in figure 5.13. The small aperture function $f_1(t)$ is derived from the product (red area) of QPC step function fit (blue solid line) and the incoming Gaussian AWG pulse $f_2(t)$ (orange solid line). The current to voltage characteristics or pinch-off curves for the three QPCs are shown in figure 5.11. Figure 5.13b shows then the convolution $(f_1 * f_2)(t)$ of the aperture function $f_1(t)$ and the incoming Gaussian $f_2(t)$ assuming a Gaussian response $h(t)$ in equation 5.10. The limitation to test this sampling setup is more on the injection side given by the dispersion of 1.5 m coaxial RF line down to low temperatures shown in figure 5.2. Figure 5.14 shows how the different voltage set points on the QPC current to voltage curve (blue line) can lead to sharpening of the Gaussian sampler drive pulse. Optimizing the sampling aperture via the DC offset of the QPC 1 sampler drive with respect to the pinched (fully closed) point contact leads to different pulse widths shown in figure 5.14a. The measured pulse width decreases from a Gaussian with $\Gamma = (66.9 \pm 0.6)\,\text{ps}$ (orange points and line) to $\Gamma = (60.0 \pm 0.4)\,\text{ps}$ (green curve) and $\Gamma = (55.5 \pm 0.4)\,\text{ps}$ (red curve). A possible interpretation is that the fraction of the sampler drive pulse shown in figure 5.14a decreases also in a similar way leading to a very small current fraction from orange solid line ($f_1 * f_2 < 2.5\,\text{ps}$), ($f_1 * f_2 < 1\,\text{ps}$) green line and finally red line ($f_1 * f_2 < 0.5\,\text{ps}$) using the convolution product:

$$f_1 * f_2 = (I(V) * G^{-1}(-V_{DC} + V))/I_{norm}, \tag{5.17}$$

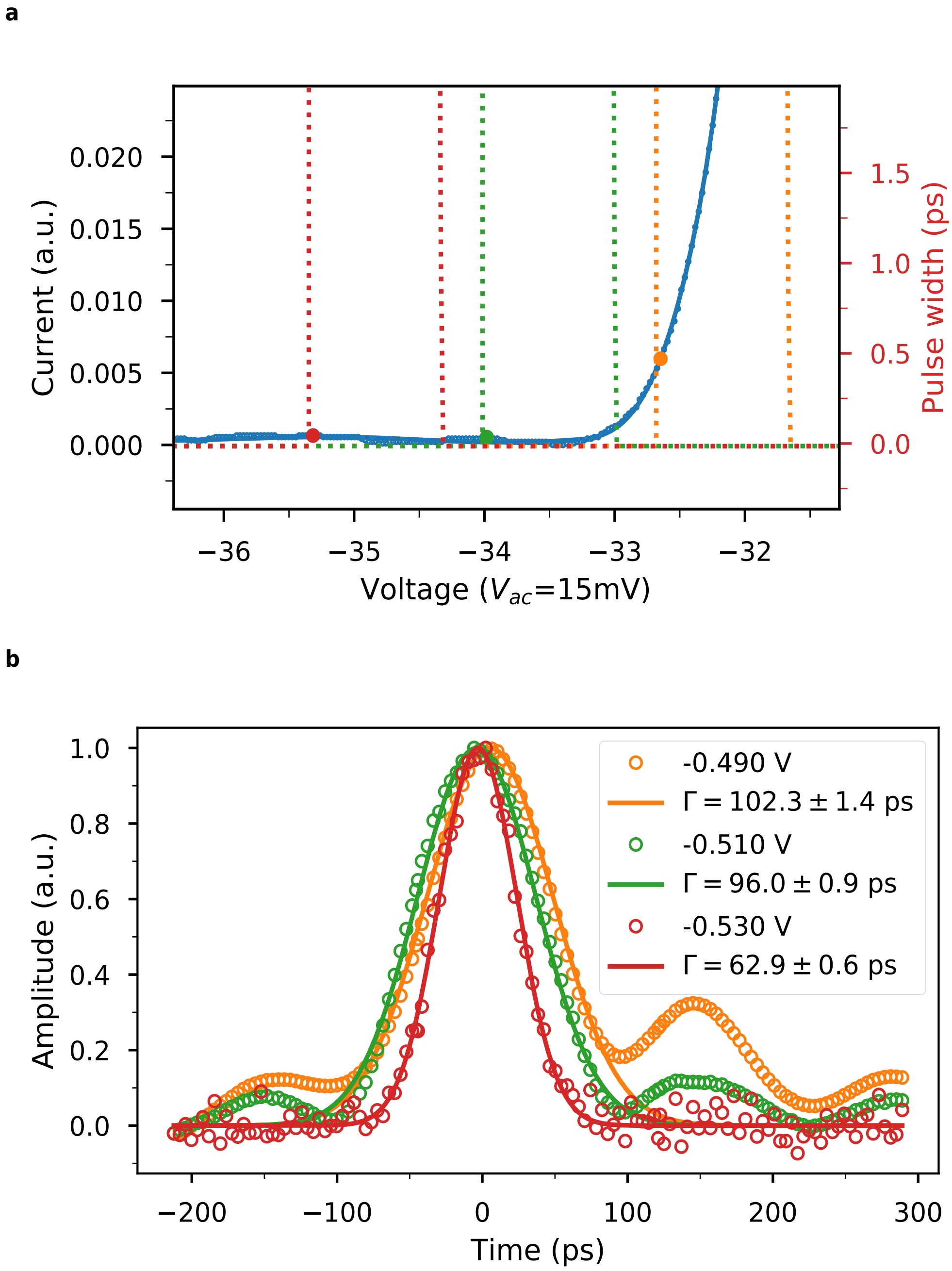

**Figure 5.15. | QPC 2 setpoints and sampled pulse. a**, QPC 2 conductance trace. **b**, QPC2 Time trace setting the DC offset more negative to the pinch-off (orange, green red voltage setpoints).

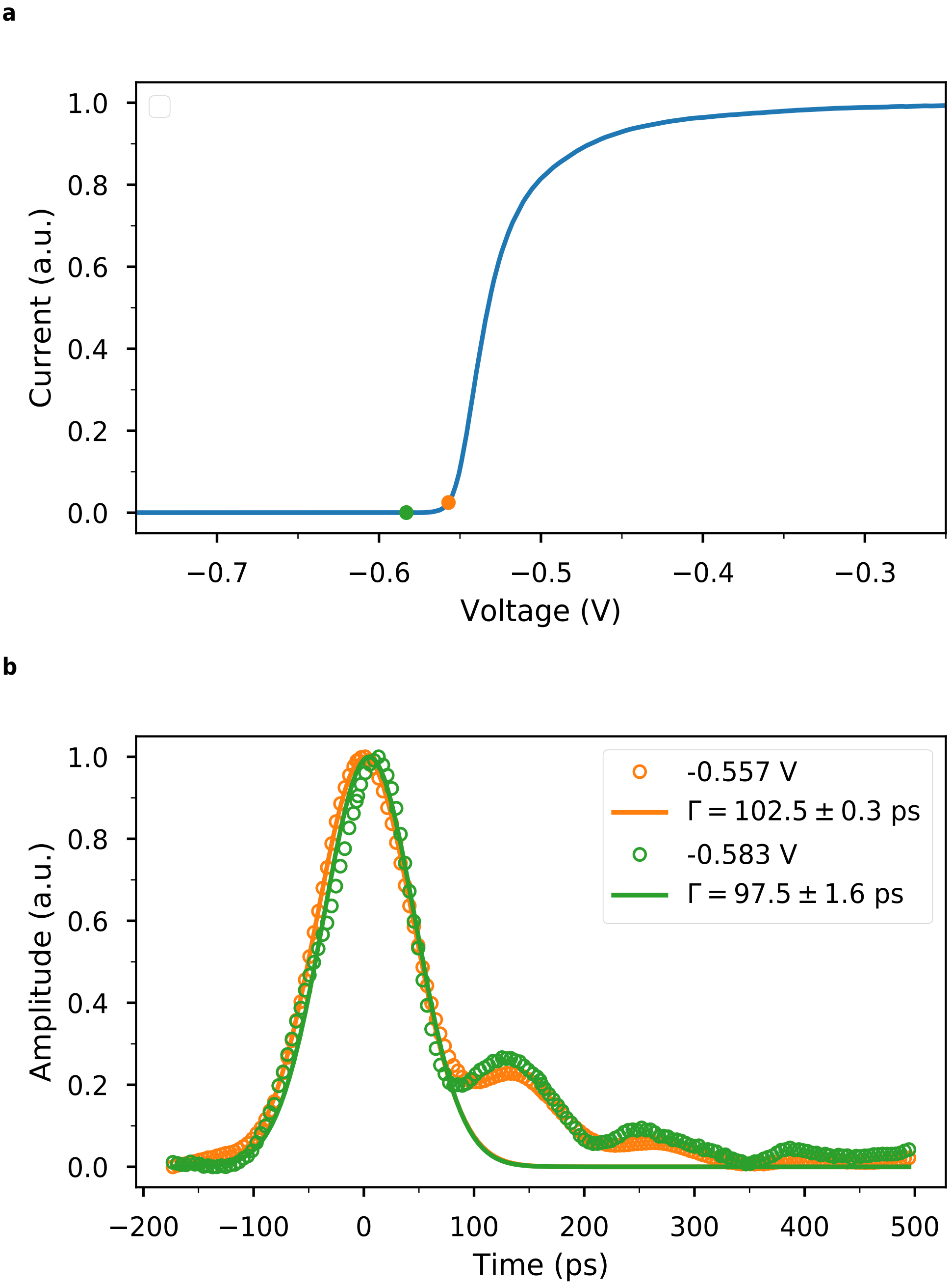

**Figure 5.16. | QPC 3 setpoints and sampled pulse. a**, QPC 3 conductance curve **b**, QPC 3 time trace setting the DC offset more negative to the pinch-off (orange, green voltage setpoints).

with

$$G^{-1}(V) = \sqrt{-\log\left(V\right)} \cdot 2\sigma \tag{5.18}$$

the inverted Gaussian sampler driver (AWG) pulse, with width $\sigma$ and the measured QPC $I(V)$ curve. The same qualitatitve analysis is then also shown for QPC2 and QPC3 in figure 5.15 respectively 5.16. Optimizing the set-point at the pinch-off curve leads to two observed behaviors: first the sharpening of the pulse qualitatively explained by the minimized aperture and incoming pulse product and second filtering or suppression of the side features of the Gaussian AWG pulses. Subsequently, we try to shape the pulses in a way that we have a specific waveform sampled in the quantum conductor.

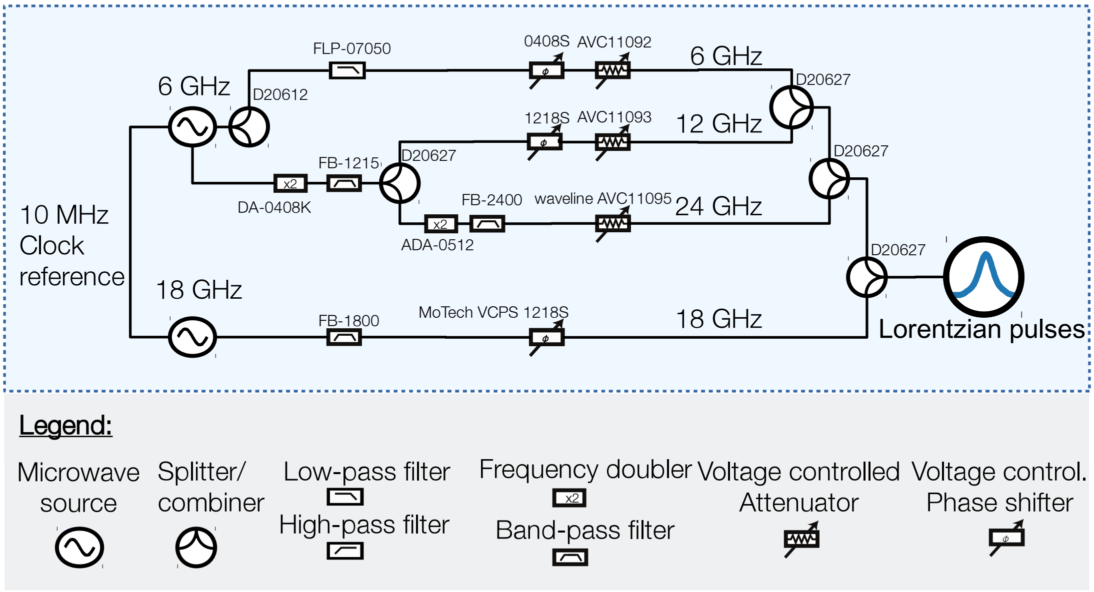

**Figure 5.17. | Fourier synthesis setup of a Lorentzian pulse train .** Two RF sources are locked to the same reference and synced using a double phase-locked loop (PLL) as shown in section 5.5. Power splitters (D20612, D20627) split the source signals. Frequency doublers (DA-0408K, ADA-0512) are used to create, the higher harmonics, 12 and 24 GHz respectively. Filters (FLP-07050, FB-1215, FB-1800, FB-2400), voltage controlled phase shifters (MoTech) and attenuators (waveline AVC1109*) shape and shift the single harmonic waves before being combined to a Lorentzian-shaped pulse train.

As we are interested in generating Lorentzian pulse trains rather than Gaussian, I now describe a newly developed RF setup that allows to generate at will Lorentzian voltage pulses as superposition of harmonics. The two source sine waves (6GHz and 18GHz) are produced using two referenced microwave sources. Power splitters (D20612, D20627) split up the 6GHz source signals in three paths. Frequency doublers are used to create 12 and 24 GHz. Every frequency branch is filtered to reject reflections interfering from other paths using a low pass filter and several band-pass filters. Every sinusoidal wave can be controlled in phase and amplitude by voltage-controlled phase shifters and attenuators. Three power combiners lead together all four sources to form a Leviton pulse train as also shown in the blueprint 5.17.

Shaping the output pulse train frequency by frequency using manually set DAC voltages leads to a Leviton waveform at room temperature. The next experimental challenge is to tune the pulse sequence to pre-compensate for the phase and amplitude dispersion in the RF lines down to low temperatures (cf. figure 5.2). A Leviton pump-probe detection in a quantum conductor can be done using the cryogenic sampling technique shown in figure 5.8b. The first Leviton pulses sampled at low temperatures are shown in figure 5.18. The solid line shows a fit of a sum of the Fourier components (6,12,18 GHz) shown as dashed lines. A Lorentzian pulse train fit is used to extract the full pulse width at half maximum Γ via:

$$\Psi(t) = c + \sum_{k=0}^{n} \cdot \frac{A}{1 + \left[\left(t - (t_0 \cdot \frac{1}{6}k)\right) / (\frac{1}{2} \cdot \Gamma)\right]^2}, \tag{5.19}$$

where $A$ is the amplitude, $c$ is the constant offset of the whole pulse train, and $k$ relates to the $k^{th}$ Lorentzian pulse in the pulse train. The blue line corresponds then to a least square fit of 5.19 with $A = 1.41 \pm 0.02$, $c = -0.61 \pm 0.03$, $\Gamma = (76 \pm 2)$ ps. The pulses produced by the setup shown in figure 5.17 are limited in their pulse width $\Gamma = (76 \pm 2)$ ps by the highest accessible harmonic contributing to the pulse train and their phase stability due to a slow phase drift over several hours. Thus, the pulse shape and stability is investigated and improved subsequently.

## 5.5 PHASE LOCKED PULSE GENERATION FOR ELECTRONIC QUANTUM CONTROL

Very short electronic pulses can be generated using Fourier synthesis of high frequency (GHz range) sine waves. Fast arbitrary waveform generators use similar analog signal superposition, so-called interleaving techniques to create pulses down to picosecond time scales.

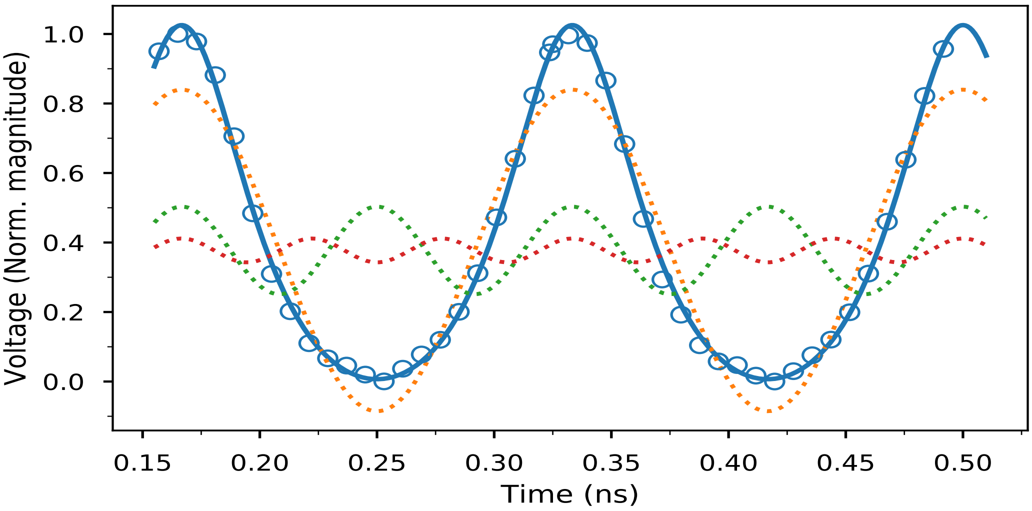

**Figure 5.18. | Leviton pulse sequence measured time-resolved in a quantum conductor.** Solid line shows a fit to the sampled data points using a sum of the four Fourier components. The Fourier components are shown as dashed line sine waves with 6,12,18 GHz.

An electronic wavepacket with a Lorentzian waveform in time domain also called Leviton can be synthesized using for instance the harmonic set of: 6 GHz, 12 GHz, 18 GHz and 24 GHz as shown in the simulation in figure 5.19. Figure 5.19c shows the Fourier transform of the superposition with peaks (marked as red crosses) at the injected frequencies. If the superposition of sine waves is not phase locked and synchronized, the Fourier components drift independently in time and the waveform can change its form as shown in figure 5.20. After two hours of measurements the pulse train maxima drift 16 ps, on several hours the phase relation between the two sources drifts away and the pulses show side bands (green curve). Active feed-back phase locked loops which track and compensate phase changes can be used to keep the phase during several hours of measurement as shown in figure 5.22. A double phase locked generation of an ultra-low jitter reference clock signal generator and two voltage controlled oscillators which are phase-locked to the reference are developed and tested. The modular

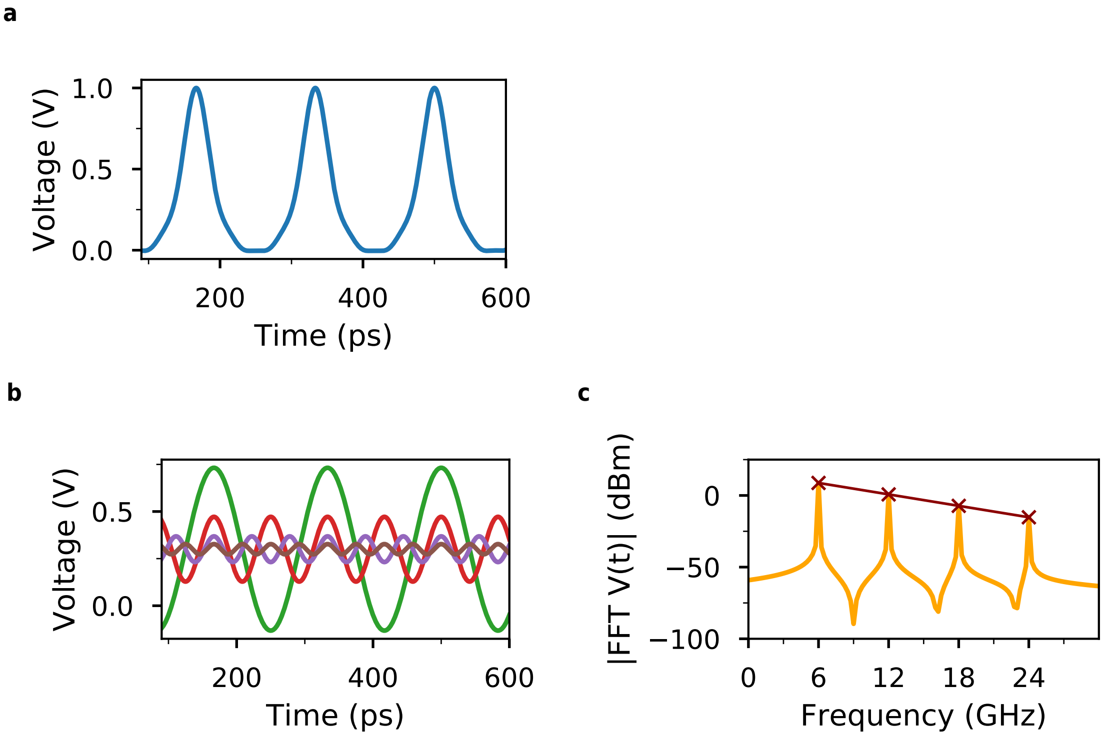

**Figure 5.19. | Fourier synthesis of Lorentzian pulses.** **a**, Voltage signal simulation in time domain for a Leviton pulse train excitation (blue line) with $\text{FWHM} = 44\,\text{ps}$. **b**, Here example with a sum of $(6, 12, 18, 24)$ GHz harmonic cosine waves with amplitude $(8.75, 0.75, -7.25, -15.25)$ dBm shown as continous lines. **c**, Absolute of the Fourier transform of the Leviton pulse train above resulting in a sum of peaks at the frequencies of the cosine waves (orange line). The exponential amplitude scaling (linear in the dBm log scale $m = -8/6\,\text{dbm}/\text{GHz}$) of the cosine Fourier components is depicted in red with crosses showing the peak positions.

setup using embedded chips can output a synchronized high frequency microwave signal up to 19 GHz.

Figure 5.21 shows the green clock generator board (Texas Instruments LMK04832EVM) and the two blue RF synthesizer boards with phase synchronization (Texas Instruments LMX2595EVM). The clock generator board takes a clock reference input and can output up to 14 different frequency clocks which are dual phase locked to a clock reference input. The different differential clock outputs have an ultra-low timing jitter (<50 fs) and can be delayed in time to time-synchronize complete measurement

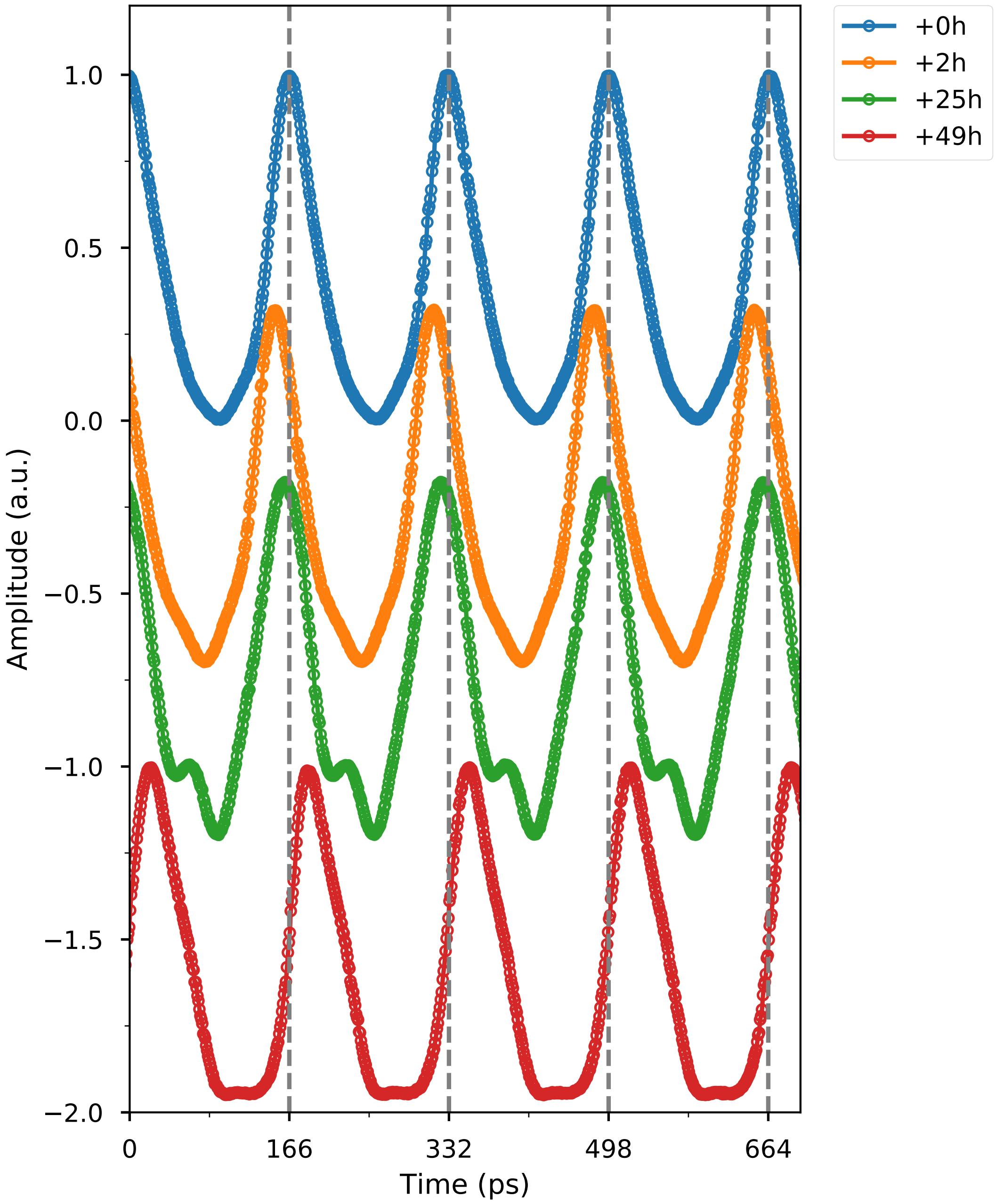

**Figure 5.20. | Time drift of the first version Leviton Fourier synthesis.** Setup as shown in the blueprint (cf. 5.17). Blue data points original pulse shape, orange curve drift after 2h, green curve 25h and red after 49h of measurements respectively.

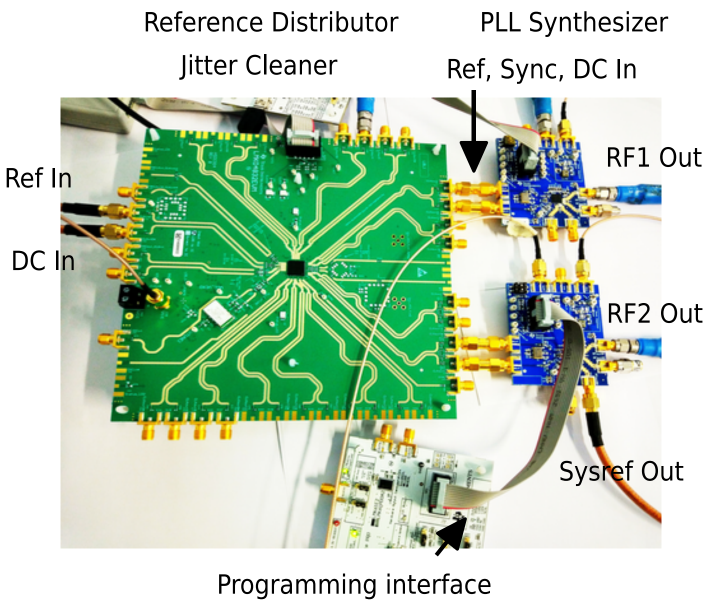

**Figure 5.21. | Modular prototype for clock generation, phase locking and programmable frequency generation using embedded devices.** Clock distribution and PLL frequency locking modules for GHz wave synthesis. Green PCB clock generator LMK04832EVM with a very low timing jitter and two blue PCBs connecting to 19 GHz programmable RF PLL synthesizer modules LMX2595EVM.

setups with up to 14 different clocks per board. A prototype programmable picosecond pulse control setup is tested using two RF synthesizers. The RF modules take the differential reference from the clock generator and output at phase locked high frequency microwave. Generating the source microwaves in this configuration ensures very low waveform jitter and low phase drifts. The two RF synthesizers can be run in phase-locked mode a full day with only a small drift of few pico-seconds ($< 5\,\text{ps}$) as measured in figure 5.22. The remaining small drift is in the same direction for both sources and can be explained by thermal drifts since neither the clock generator nor the RF synthesizers are temperature regulated.

Digital phase locking of clock signals is currently only possible with a sub-ps jitter at room temperature and active research at cryogenic temperatures[77]. The high precision

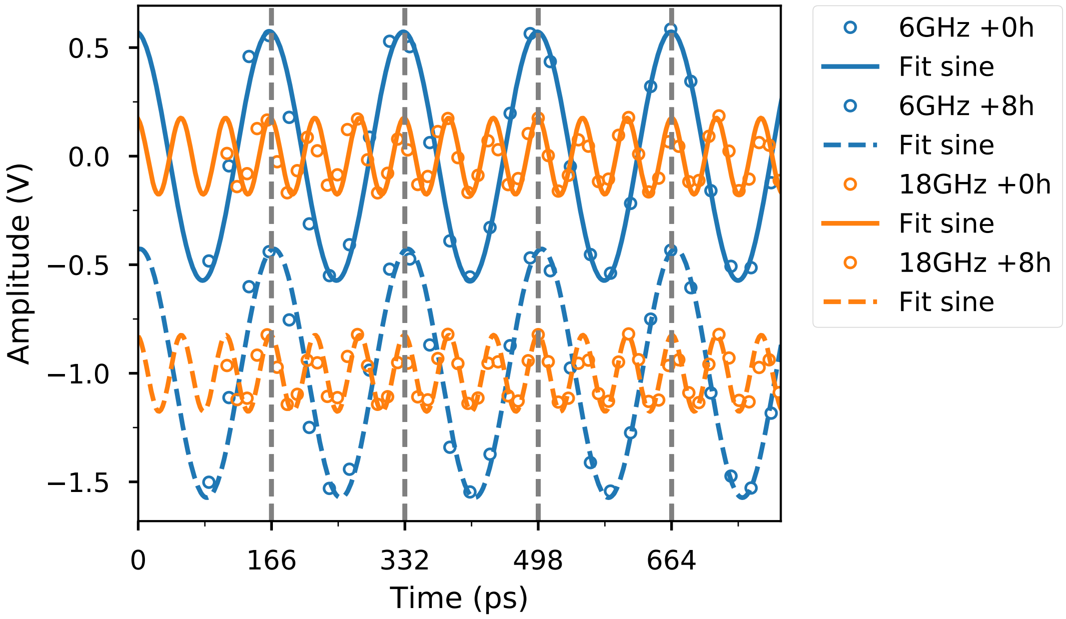

**Figure 5.22. | Synchronization measurements modular prototype for clock generation** Phase synchronized two-channel microwave source. Blue curves 6 GHz sine waves measured in the morning (solid lines +0h) and evening (dashed lines +8h) respectively. Orange curves 18 GHz sine waves. Time drift of a 18 GHz sine wave during 8 hours of around 3ps. Time drift of a 6 GHz sine wave of around 4ps.

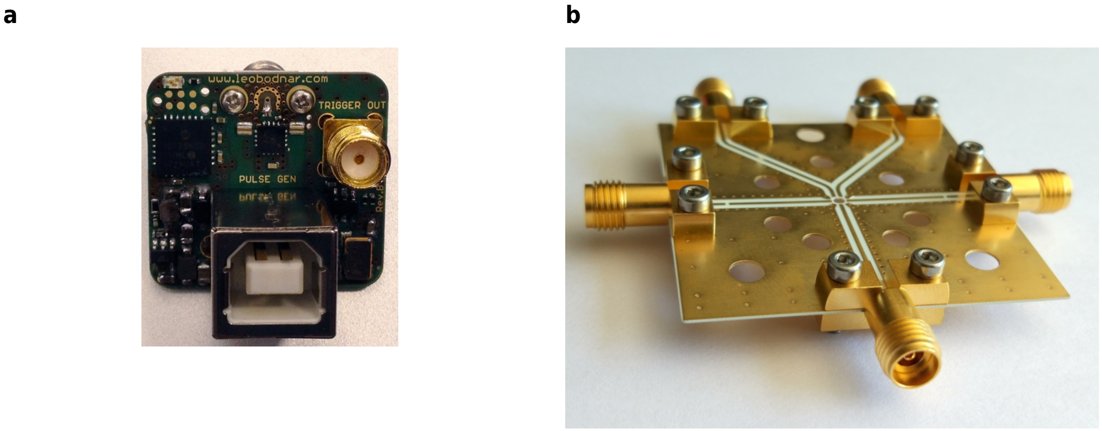

**Figure 5.23. | 50GHz switch and pulser.** Components used to synchronize and switch out a single Leviton pulse out of a Fourier synthesized pulse train. **a**, Fast pulser to be synched. **b**, Switch PCB design.

of solid-state electronics at room temperature implies also that the synchronization and supply stage of a cryogenic setup including for instance quantum computer prototypes is outside of the base temperature part or quantum data layer. Subsequently I introduce a setup to switch out a single pulse out of the Leviton pulse train for having control over a single pulse. A fast synced pulser (Leo Bodnar electronics 2.92 mm pulser) with a rise-time of less then 25 ps is used subsequently to cut single pulses out of the Lorentzian pulse train. A 50 GHz bandwidth switch (Avago AMC2008) is connected to the comb generator output using a PCB with K connectors designed in house. Figure 5.23 shows the USB pulser with trigger output/synch input and the SPDT (single pole double through) switch. The PCB is designed using a low loss high frequency dielectric (RO4350B), a coplanar waveguide with dimensions matched to the K connectors. The groundplane is additionally perforated with via holes with different sizes and spacings to create reflections and a substrate integrated waveguide with the highest operating frequency $c/f_c = \lambda_c > 8p > 16d$ estimated conservatively using the via pitch $p$ and the diameter $d$ of the via hole[157].

The next challenging tasks is to bring fast, synchronized and low noise control with high frequency harmonic content down to low temperatures. An approach based on a frequency comb is developed in the following chapter in order to go even beyond the electronic pulse control with pulse widths down to $\Gamma \approx 70\,\text{ps}$ at low temperatures shown in this chapter.

*"In research, both problem finding and problem solving are important. Surprisingly often, problem finding is more important than problem solving."*

– Michael Nielsen

# 6

# COMB GENERATED LEVITONS

Measurements and pulse control can be stabilized or referenced in frequency space using a comb generator. This chapter introduces an approach to produce a Lorentzian pulse train - so called Levitons - based on a microwave frequency comb generator. After introducing Fourier synthesis of waveforms in the microwave regime, I show how to combine frequency harmonics to generate Lorentzian or Delta-like pulse trains. Subsequently, I take the analytical result for Lorentzian pulse train generation and introduce a setup that allows to shape the pulse according to a Lorentzian Fourier spectrum in amplitude. Finally, I analyze and describe phase tuning and jitter together with the first characterization of the comb generator setup.

In 1822, Joseph Fourier at this time researcher in Grenoble found a method how to write functions as an infinite sum of harmonics. Since then, signals are commonly described using Fourier analysis. Every (absolutely integrable) waveform can be described using a Fourier transform or an infinite Fourier series. A periodic signal

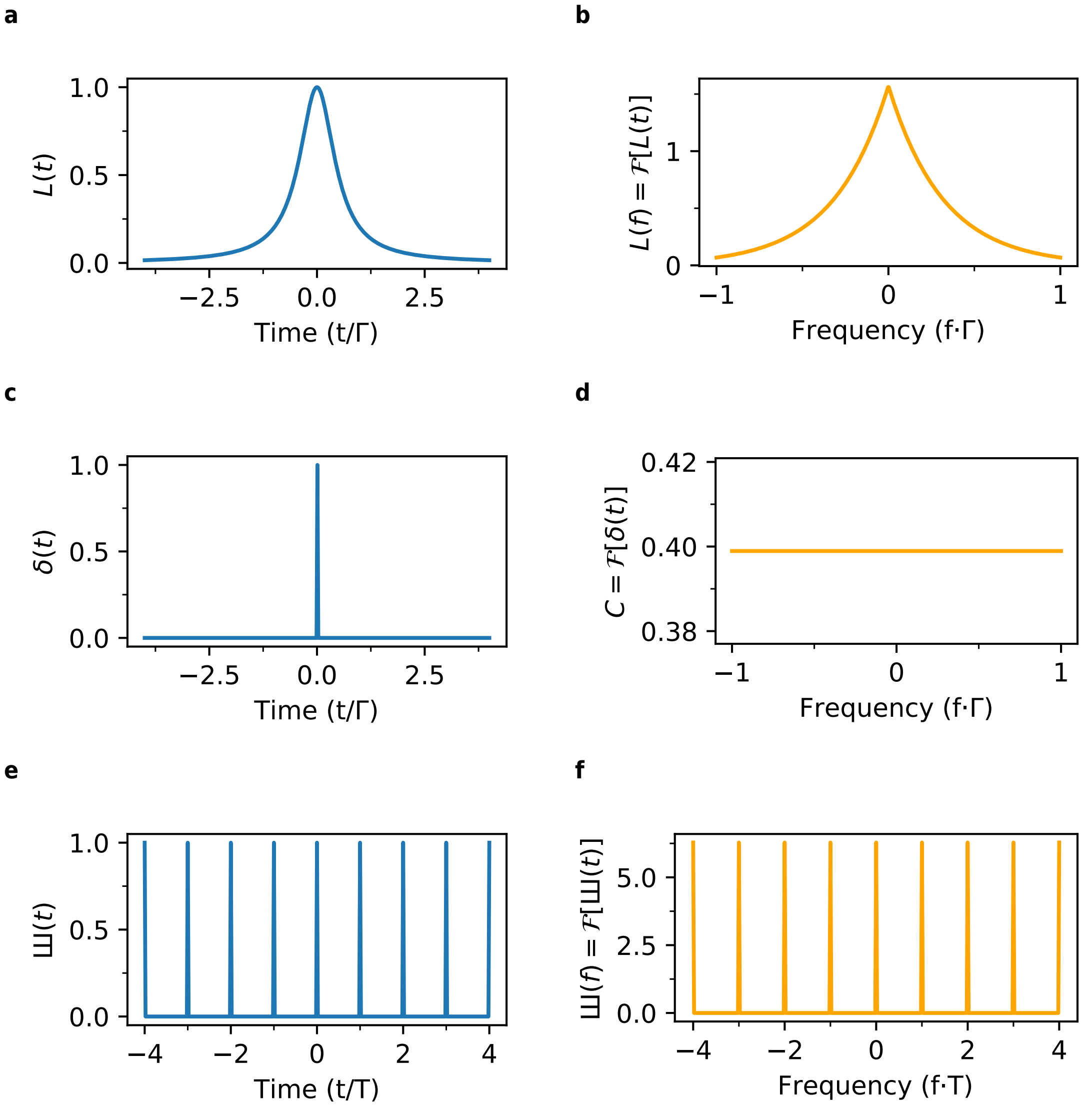

**Figure 6.1. | Fourier transform pairs. a**, Lorentzian pulse. Lorentzian pulse with full width half maximum $\Gamma$ or Cauchy distribution in time domain. **b**, Fourier transform of a Lorentzian pulse. Decaying exponential in the frequency domain with a decay proportional to $\mathrm{e}^{-|\Gamma|\cdot f}$. **c**, Dirac delta distribution. Peak with full width half maximum $\Gamma \to 0$. **d**, Fourier transform of a Dirac pulse. A constant $C$ in the frequency domain. **e**, Time trace of a Dirac comb. A comb of equally spaced Dirac pulses repeated with period $T$. **f**, Fourier transform of a Dirac comb. A comb in frequency space with spacing $1/T$.

$v(t) = v(t+nT), n \in \mathbb{Z}$ with period $T$ can be expressed by the Fourier series:

$$v(t) = \frac{a_0}{2} + \sum_{n=1}^{\infty} a_n \cos\left(2\pi\frac{nt}{T}\right) + b_n \sin\left(2\pi\frac{nt}{T}\right), \tag{6.1}$$

where the Fourier components $a_n$ for the even cosine part and $b_n$ for the odd sine part can be calculated as:

$$a_n = \frac{2}{T} \int_0^T v(t) \cos\left(2\pi \frac{nt}{T}\right) \mathrm{d}t \tag{6.2}$$

$$b_n = \frac{2}{T} \int_0^T v(t) \sin\left(2\pi \frac{nt}{T}\right) \mathrm{d}t. \tag{6.3}$$

In the more general case, if the signal is aperiodic ( $T \rightarrow \infty$, cf. appendix A.4), the integral expression the so-called Fourier transform is used:

$$\mathcal{F}\left[v(t)\right](f) = \int_{-\infty}^{\infty} v(t) \mathrm{e}^{-(2\pi i f t)} \, \mathrm{d}t \tag{6.4}$$

The following summarizes the most important pulse shapes and their Fourier transform pairs to create a Lorentzian pulse train. Figure 6.1 shows the time- and frequency domain spectra of important pulse forms.

A Lorentzian pulse follows a Cauchy distribution (cf. appendix A.5). Figure 6.1a shows a Lorentzian pulse $L(t)$ centered at zero $t_0 = 0$ with normalized amplitude $A = 1$ and time-spread $\Gamma = 1$:

$$L(t) = \frac{1}{1 + \frac{4t^2}{\Gamma^2}}, \quad \mathcal{F}\left[L(t)\right](f) = 1/2\pi\Gamma \mathrm{e}^{-\pi\Gamma f}. \tag{6.5}$$

A Lorentzian pulse has an exponential amplitude dependence in the frequency space $L(f) \propto \mathrm{e}^{-\Gamma \cdot f}$ as shown in figure 6.1b. The Lorentzian pulse approaches a Dirac delta distribution $\delta(t)$ in the limiting case of $\Gamma \rightarrow 0$ 6.1c. Then, the frequency spectrum is constant as shown in figure 6.1d. All plots are normalized in amplitude to the time domain spectrum, the frequency domain amplitude follows then from the Fourier integral (equation 6.4). An ideal frequency comb $\text{Ш}(t)$ is a periodic train of Dirac pulses. A Dirac comb with spacing $T$ between the pulses has as a Fourier transform which is also a Dirac comb $\text{Ш}(f)$ with spacing $1/T$ as shown in figure 6.1f. These Fourier transform properties can be used to calculate the limits of an optimal Lorentzian pulse

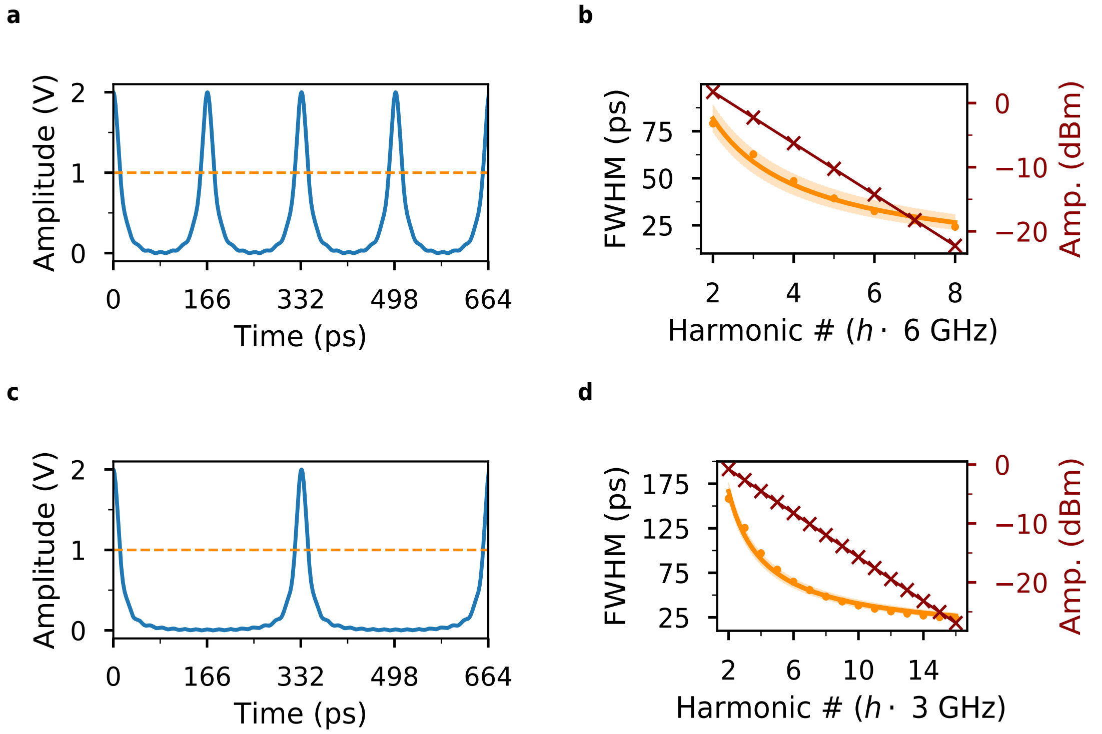

**Figure 6.2. | Lorentzian-shaped comb simulation for different base frequencies. a**, Lorentzian train at base frequency $f_{base} = 6\,\text{GHz}$, $h = 8$. **b**, Right axis exponential amplitude (red crosses) and left axis pulse width (orange points) with fit line $h^n \cdot b$. Shaded orange areas depict the standard error of the orange fit curve. **c**, Levitons at base frequency $f_{base} = 3\,\text{GHz}$, $h = 16$. **d**, Amplitude pulse width relation at 3 GHz.

train. In the following, I will analyze frequency combs with a base frequency of 3GHz and 6GHz, which is similar to what has been used in the previous chapter for the low temperature measurements.

## 6.1 FOURIER SYNTHESIS OF PULSE TRAINS

Analytically, a Leviton pulse train signal can be synthesized starting from a comb pulse train, with an exponential decaying amplitude envelope in frequency space. Figure 6.2 shows different kind of pulse trains generated using frequency harmonics with a constant identical phase offset and different amplitude scaling. A pulse train using

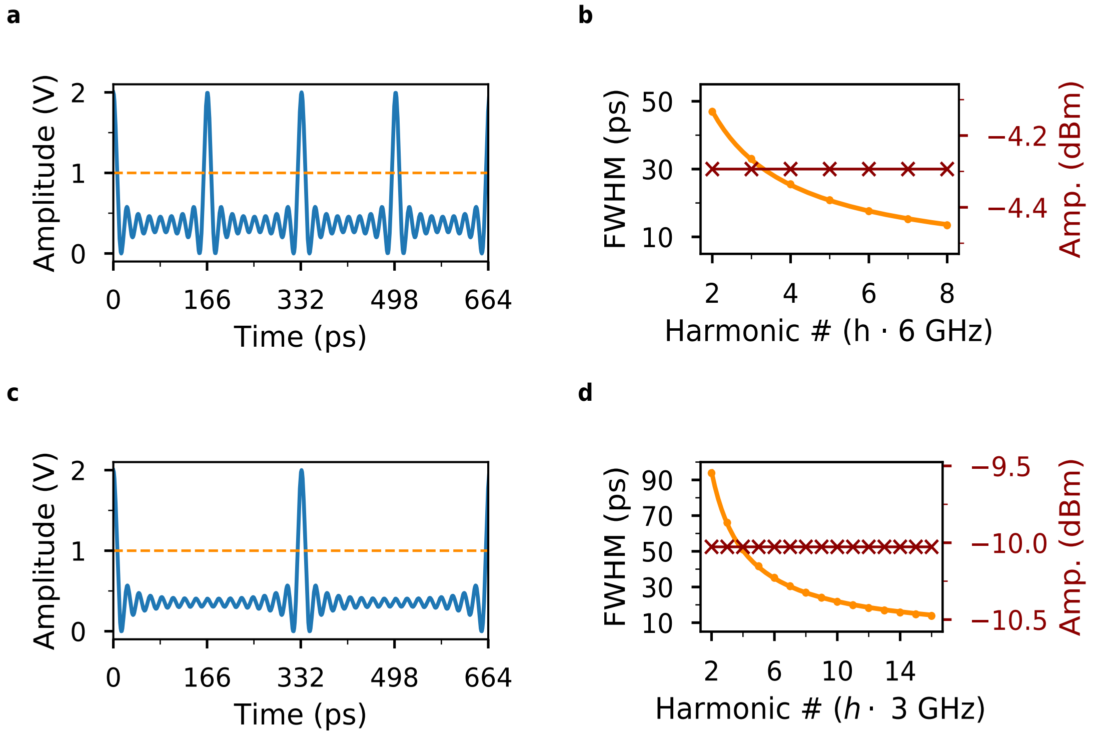

**Figure 6.3. | Delta peak-shaped comb simulation at different base frequencies. a**, Delta peaklike train at base frequency $f_{base} = 6\,\text{GHz}$, $h = 8$. **b**, Constant amplitude and pulse width scaling at $f_{base} = 6\,\text{GHz}$. **c**, Delta pulse train at base frequency $f_{base} = 3\,\text{GHz}$, $h = 16$ **d**, Constant amplitude and pulse width scaling at $f_{base} = 3\,\text{GHz}$.

a sum of eight harmonics is shown in figure 6.2a. The amplitude difference between each of the harmonics (6,12,18,24,30,36,42,48) GHz is set to 4dBm as shown in the red curve in figure 6.2b. The red curve of the amplitudes has a slope of 4dBm/6GHz. The frequency dependent pulse width $\Gamma$ (FWHM) can be well described using a power law:

$$\Gamma = h^n \cdot b \tag{6.6}$$

where $h \in \mathbb{Z}_{>1}$ is the highest harmonic inside the pulse, $n < 0$ is the negative exponent and $b$ is the offset (in a log-log plot) given by the FWHM of the first two combined harmonics. The orange curve in figure 6.2b shows the trend of the full width half maximum of the pulses going down with the highest harmonic h following an inverse power law. The orange shaded areas show the standard error of the power law fit.

Starting with a 3 GHz base frequency as shown in figure 6.2c with a 2dBm/3GHz slope of attenuation shows a very similar pulse width fit as for the case of 6 GHz. The main difference is that a lower base frequency implies that more harmonics need to be summed up to obtain a similar small pulse width (cf. figure 6.2d). For the Lorentzian-like pulse trains in figures 6.2b and 6.2d the fits are given as $n_{l6} = -0.81 \pm 0.05$ and $b_{l6} = (144 \pm 8)$ps at 6 GHz base frequency ($h \cdot 6\,$GHz) and $n_{l3} = -0.88 \pm 0.02$ and $b_{l3} = (307 \pm 12)$ps at base 3 GHz base frequency. The amplitude scaling between the harmonic cosine waves to obtain a Lorentzian pulse train needs to be exponential (linear in dBm scale). Figure 6.3 shows a pulse train using a combination of constant amplitude cosine waves, then approximating delta-like pulses. The points in figures 6.3d and 6.3b are already bigger than the confidence interval of the power-law fit. The fits of the pulse width of the delta-like pulse trains are given as $n_{d6} = -0.894 \pm 0.006$ and $b_{d6} = (87.5 \pm 0.6)$ps at 6 GHz base frequency ($h \cdot 6\,$GHz) and $n_{d3} = -0.909 \pm 0.006$ and $b_{d3} = (177.6 \pm 1.2)$ps at 3 GHz base frequency. The more harmonics are used, the more precisely the pulse width decay can be described by an analytical power law. The constant amplitude cosine wave combinations have a faster decay and approach a delta-shaped pulse train. The osillations in the wings come from the limited high harmonic frequency content, an ideal delta pulse would have an infinite bandwidth in Fourier space. The simulations are limited up to 50 GHz, which is also the frequency bandwidth accessible with commercial coaxial lines and connectors currently installed at low temperatures in our setup. I introduce a source for producing electronic equidistant spaced pulses a so called comb generator in the following.

## 6.2 MICROWAVE COMB GENERATOR

I use a microwave comb generator with a multi GHz bandwidth (marki microwave NLTL 6026) to create frequency harmonics for shaping a Lorentzian pulse train. Microwave frequency combs are often fabricated using monolithic III-V semiconductor technology for instance on GaAs wafers. The chip design can contain a coplanar waveguide transmission line where the center conductor is connected to ground by distributed reverse-biased Schottky diodes acting as shunt varactors[21]. An electronic non-linear transmission line leads to sharpening of the rising and falling edges of injected pulses in the time domain[1]. The principle of pulse sharpening is frequently used to create pico-second rise-time pulsers for ultra-wide band electronic sampling or harmonic generation[143]. In the frequency domain, the power of the injected base harmonic is distributed over the higher harmonic multiples via:

$$f_{comb} = \sum_{n} f_{base} \cdot n \tag{6.7}$$

The output has peaks at equidistant frequency spacings given by the base frequency $f_{base}$ up to around 70 GHz. The phases of the output harmonics are locked to the input frequency like in a multiplier. An optical frequency comb spanning a large multi THz bandwidth is the most precise ruler for frequency measurements[184] and enhances spectroscopy[138]. First, the output Fourier components of the comb generator are analyzed.

The time-resolved pulse output of the microwave frequency comb (marki NLTL-6026) is measured in figure 6.4 at an input frequency $f_{base} = 3\,\text{GHz}$. The blue data points show the pulse train and the red line is the integral over the waveform, forming steps of flux per pulse. Figure 6.4b shows the Fast Fourier Transform (FFT) of the acquired data. The measured pulse shape is not Lorentzian-like since the amplitude of the dif-

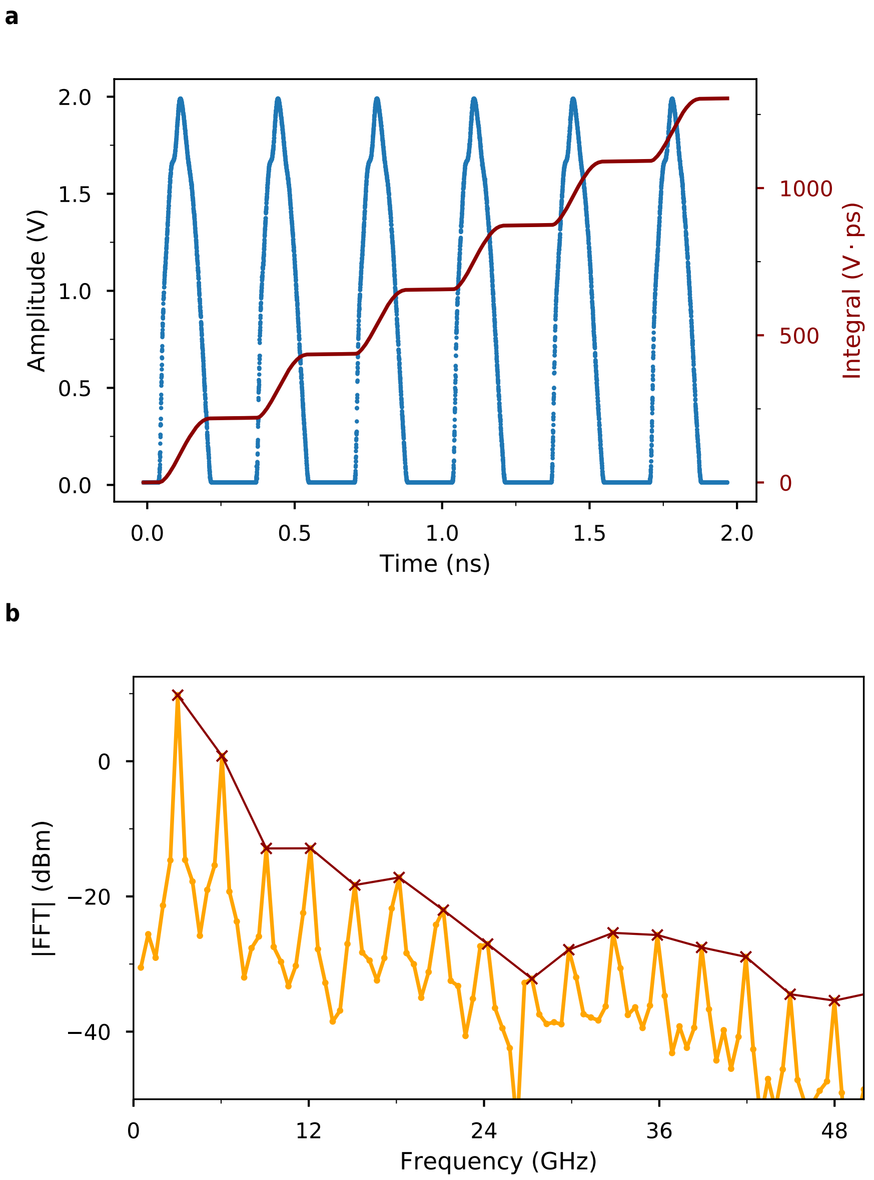

**Figure 6.4. | Comb generator and FFT spectrum. a**, Time trace of the frequency comb output at base frequency $f_{base} = 3\,\text{GHz}$. Red line shows the flux integral of the pulse sequence. **b**, Fast Fourier Transform spectrum of the comb generator output. Red crosses depict the amplitude peaks spaced by the base repetition rate $f_{base} = 3\,\text{GHz}$.

ferent harmonic do not decay linearly on the dBm scale. Harmonics up to 48 GHz contribute to the pulse as shown in the Fourier spectrum (cf. figure 6.4b). A complementary way to analyze the signal is the expansion of the pulse sequence in harmonic

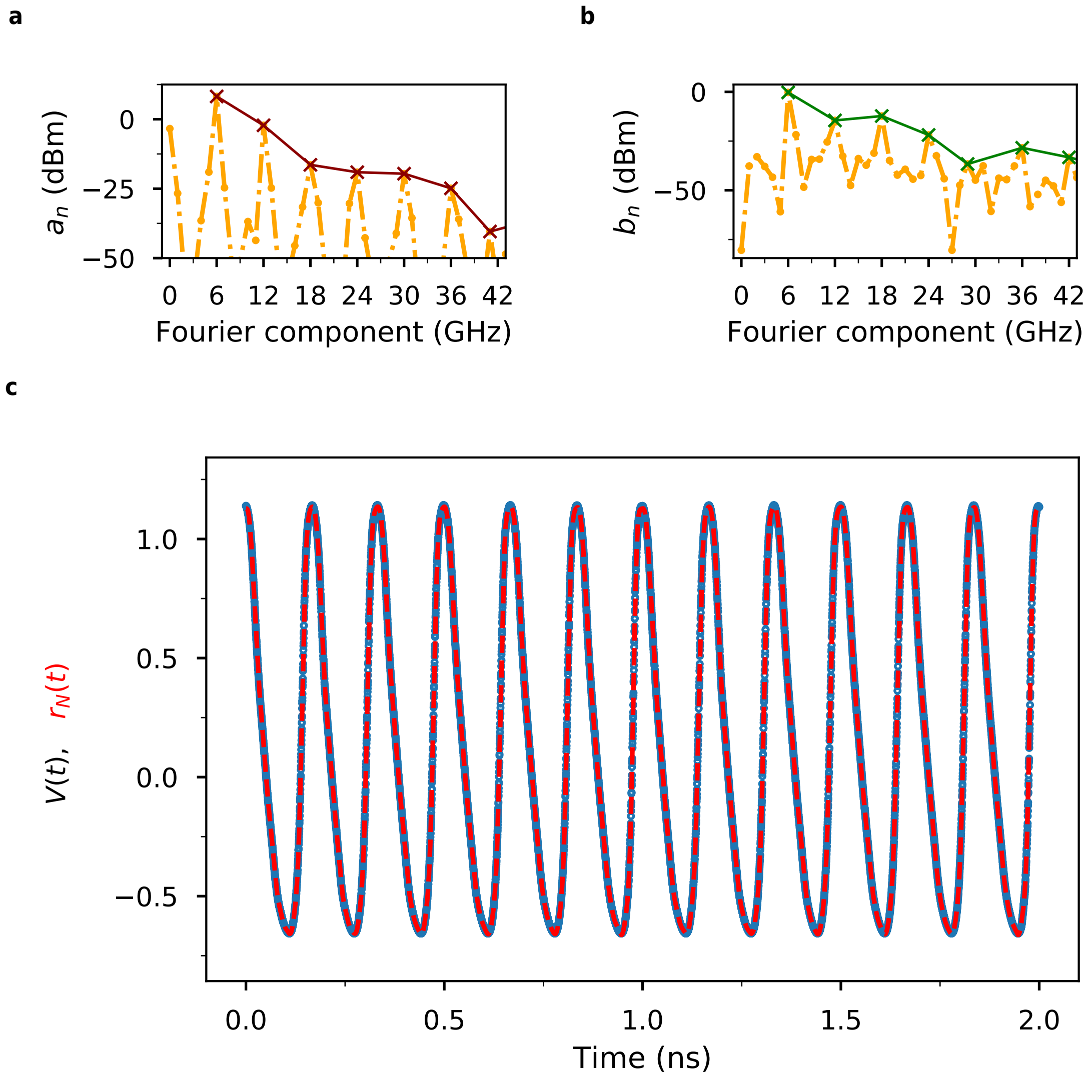

**Figure 6.5. | Fourier series analysis of the measured frequeny comb output with 6GHz base frequency. a**, Fourier components of even $a_n$, and **b**, odd $b_n$ parts. Brown and green crosses show the peak positions with frequency spacing $f_{base} = 6\,\text{GHz}$. **c**, Reconstruction $r_N(t)$ using the calculated $a_n$ and $b_n$ components for $N = 50$ of the measured time trace $V(t)$ (blue data points) shown as a red dashed line.

Fourier series components. Figure 6.5 shows the Fourier components of the even cosine part $a_n$ and the odd sine part $b_n$ of the comb generator output with an frequency input of $f_{base} = 6\,\text{GHz}$. The middle part of figure 6.5 shows the first 50 Fourier components used for the reconstruction, where the even cosine waves are shown in brown and the odd sine parts in green. The reconstruction using the sum of all 50 waves is then shown on the right side as dashed red line overlapping with the measured blue time trace data points. The advantage of the time-periodic series analysis is that the extracted dBm value at the known repetition/base frequency can directly be used for pulse shaping. The Fourier components $a_n$ and $b_n$ plotted on the left side of figure 6.5 provide all the information to reconstruct the complete waveform via:

$$r_N(t) = \frac{a_0}{2} + \sum_{n=1}^{N} A_n \cos(2\pi n t/T + \phi_n), \tag{6.8}$$

with phase offset $\phi_n = \tan^{-1}(-b_n/a_n)$ and amplitude $A_n = \sqrt{a_n^2 + b_n^2}$ shown as red dashed line for $N = 50$ in figure 6.5. The Fourier components at the harmonic frequencies can then be used to estimate the signal conditioning needed to form a perfect Lorentzian shaped pulse train as follows. The microwave comb generator output has a non-linear dispersion. The output characteristics of the comb generator (marki NLTL 6026) are shown in figure 6.6. A non-linear dispersion means that for every different frequency input and also for different input powers the output power of the harmonics is slightly different and needs to be compensated in amplitude and phase matched to form a specific pulse train. The advantage of using a frequency comb fed from a single base frequency is the inherent locked phase relation of the output harmonics given by the comb generator's fixed dispersion. Figure 6.6 shows the comb generator output for 3 GHz and 6 GHz base frequency input with the maximal pulse amplitude of 2 V (just below the saturation of the scope LeCroy WaveExpert 100H). The output amplitudes follow already quite closely an exponential trend and the output pulses look Lorentzian-shaped for a high frequency input like 6 GHz as shown with green crosses. At lower input frequency, for instance at 3 GHz input shown as blue lines with crosses, the dispersion gets more complicated. Some frequencies tend to be more attenuated than others as can be seen for instance at the dip at 27 GHz. Additionally to

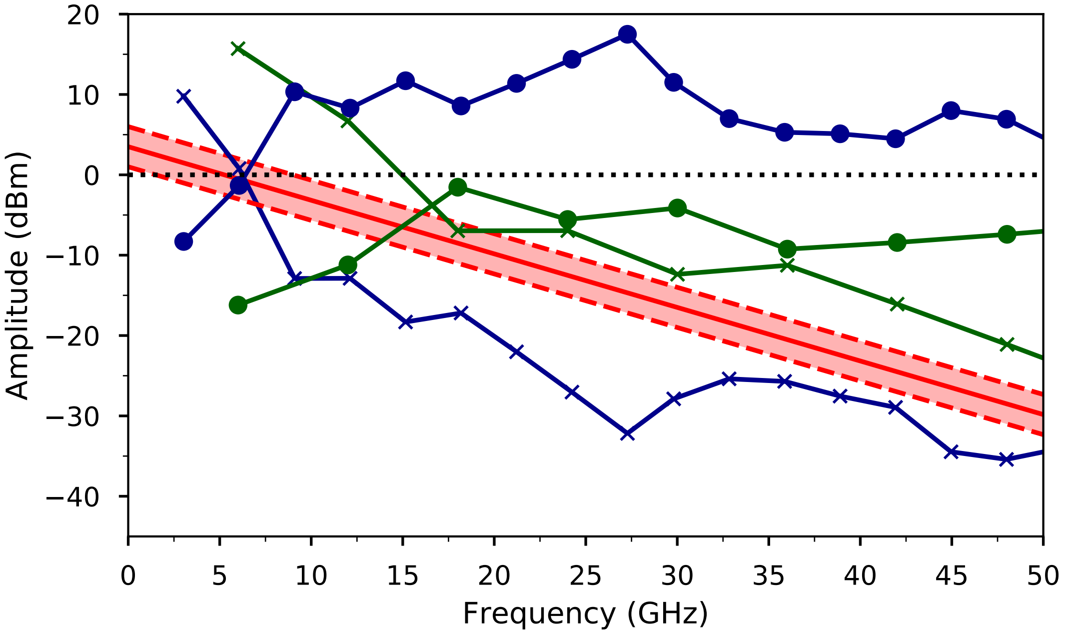

**Figure 6.6. | Frequency dependent amplitude output of the microwave frequency comb generator and compensation.** Comb generator output for 3 GHz (blue crosses) and 6 GHz (green crosses) with an output amplitude of 2 V. The needed compensation of the output amplitude is then shown with green (6 GHz) respectively blue (3 GHz) points to arrive at the linear target amplitude (red line) with the shaded area marking a target area of ±2.5 dB.

the comb's output dispersion, the high frequency output signals of the generator need to be splitted, phase- and amplitude-corrected, combined and sent down to a sample at low cryogenic temperatures using coaxial lines. The compensation needed to arrive at an exponential frequency output dispersion (red target line and area in dB scale) is shown with the blue and green points. The amplitudes and phases are compensated and tuned in a pulse shaping setup.

The jitter of the pulse generated by the comb generator is low. Figure 6.8 shows the measured jitter $\sigma_\tau = 1.72\,\mathrm{ps}$ of the output waveform at 18 GHz input. The low jitter of the frequency comb generator results from the multiplied phase noise of the microwave source and can be improved by suppressing the phase noise with an active feedback loop[127]. Phase drifts can then only be acquired from other active amplifica-

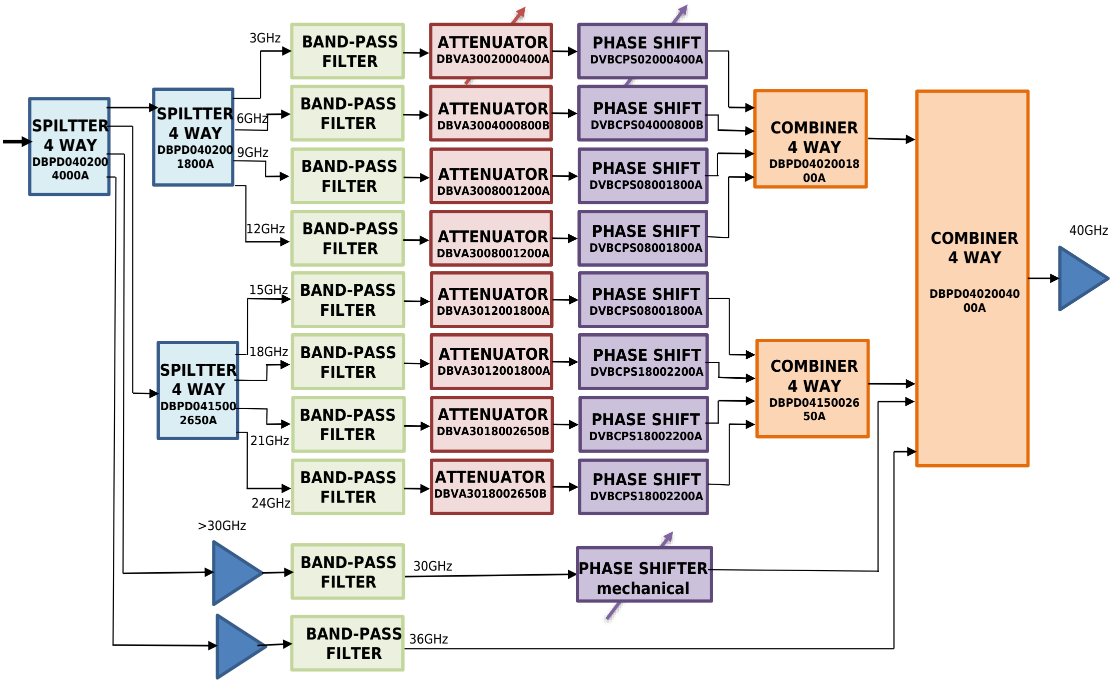

**Figure 6.7. | Comb pulse shaping setup.** Comb generator output at 3 GHz. Splitters (Pasternack) split the source signal into the ten harmonics. Bandpass filters for each frequency isolate the harmonic, voltage controlled phase shifters (Quotana) and attenuators (Quotana) shape and shift the single harmonic waves before being combined (Pasternack) and amplified to form a Leviton pulse train.

tion or phase shifters put into the pulse setup afterwards. Phase detection becomes more challenging for frequencies higher than 18 GHz, since digital electronics needs to operate at very high bit rates for phase detection and delay. Thus, a solution is to implement mechanical delay lines for higher frequencies (> 20 GHz). Moreover, the setups are built and tested at present to get some insight how to tune the phase of high frequency harmonics in a stable way. The next chapter summarizes the current status of the project and gives an outlook to possible future steps.

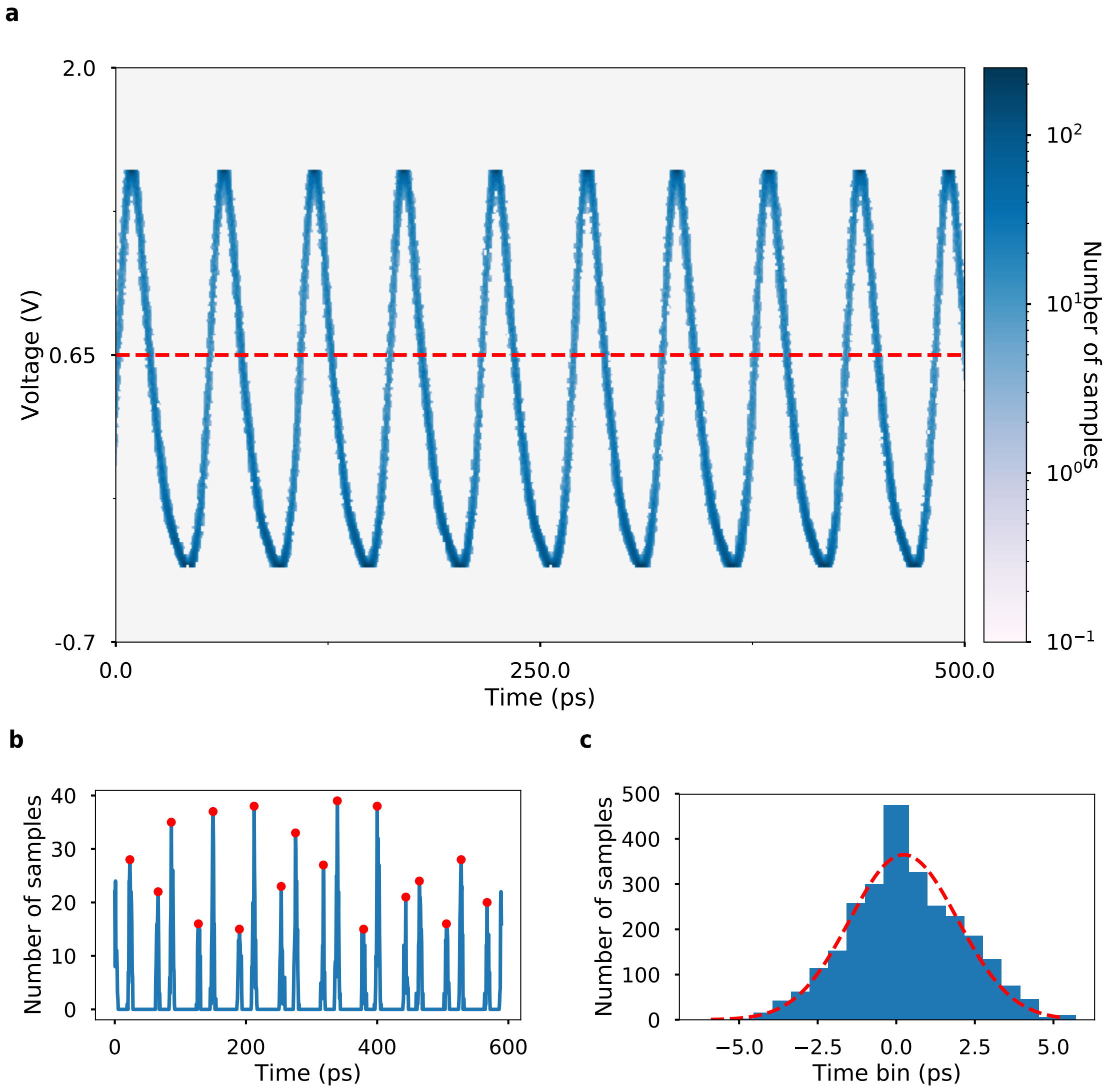

**Figure 6.8. | Comb generator jitter analysis. a**, Repeated acquisition (256) of the comb generator output with a repetition of $f_{base} = 18\,\mathrm{GHz}$ with FWHM $\Gamma = 33.6(4)\,\mathrm{ps}$. **b**, Cut through the data at $V = 0.65\,\mathrm{V}$ with peak positions marked by a red circle. **c**, Distribution of the sampling counts around the peaks. A Gaussian fit is shown as red dashed line and used to extract the root mean squared jitter of $1.72(1)\,\mathrm{ps}$.

*“It is not your fault, that the world is how it is.*
*It will only be your fault if it stays like this.” :*
*” Es ist nicht deine Schuld, dass die Welt ist*
*wie sie ist. Es wäre nur deine Schuld, wenn sie*
*so bleibt. ”*

– Farin Urlaub

# 7

# SUMMARY AND OUTLOOK

The subsequent chapter summarizes the current status of the project and gives a specific outlook for possible next steps. In chapter 3 I have presented design consideration and fabrication steps to optimize electronic pulse control at cryogenic temperatures. Measurements and setups with low noise and high sensitivity of sub femto ampère and nano volt up to MHz frequencies were introduced in chapter 4. Alongside, noise figures and long-term stability of the setup parts were discussed and characterized stepwise. In chapter 5 I presented a control setup for pico second pulse control of pulses sent to cryogenic temperatures. This pulse control setup has then be used to sample a Lorentzian pulse train representing the basis wavefunction of Levitons with a pulse width of $\Gamma = (76 \pm 2)\,\mathrm{ps}$ inside of a quantum conductor. The limits of the experimental control setup were analyzed subsequently. Next to the high number of nano-engineered gates required (>20), the current project features also two experimental challenges, low drift (< picosecond time-scales) and small pulse widths $\Gamma \approx 70\,\mathrm{ps}$. Thus, I elaborated on microwave source synchronization to keep the Fourier components of the produced Leviton pulse train in phase and presented the blueprint of a setup to select a single pulse out of the pulse train. Both experimental challenges can be tackled using a comb generator setup. In order to overcome the problems of phase locking and to decrease the pulse width towards only few picoseconds, I introduced comb-generated pulse trains in chapter 6. The chapter starts with the analytical analysis of pulse synthesis and the limits given by the Lorentzian pulse form and the highest harmonic Fourier component. I then presented the microwave comb generator output data at different base frequencies. Pulses down to 33 ps can be measured with a high phase stability using the comb generator. Based on these results, I started designing and building up a pulse shaping setup. The advantage of using a single microwave source with a comb generator is that the drift and the phase noise is minimized, due to the intrisic locking to the input source. The new pulse shaping setup can be tuned for phase offsets and amplitude differences so that the dispersion down to low temperatures can be precompensated. Results like the direct sampling of a Leviton pulse train inside a nanometric quantum conductor open up a wide range of time-controlled quantum-electronic optics experiments and also applications towards low-power 5G technology accessible with high frequency RF control setups similar to the work presented here at cryogenic temperatures. Finally, I outline some near future perspectives of the current quantum-electronic optics experiment. Single charges can produce significant phase shifts of the electronic wave function, as was recently shown by two electronic Mach Zehnder interferometer experiments in the DC current regime[55,56]. A natural extension of these experiments is to investigate time-resolved interference effects with an RF interferometer as shown in figure 7.1. The average time-resolved output current at ohmic contact four $\overline{I}_4^{ee}$ can be measured with respect to the Aharonov-Bohm phase or the time difference $\Delta t_u^{ee}$ of the electronic (single electron)

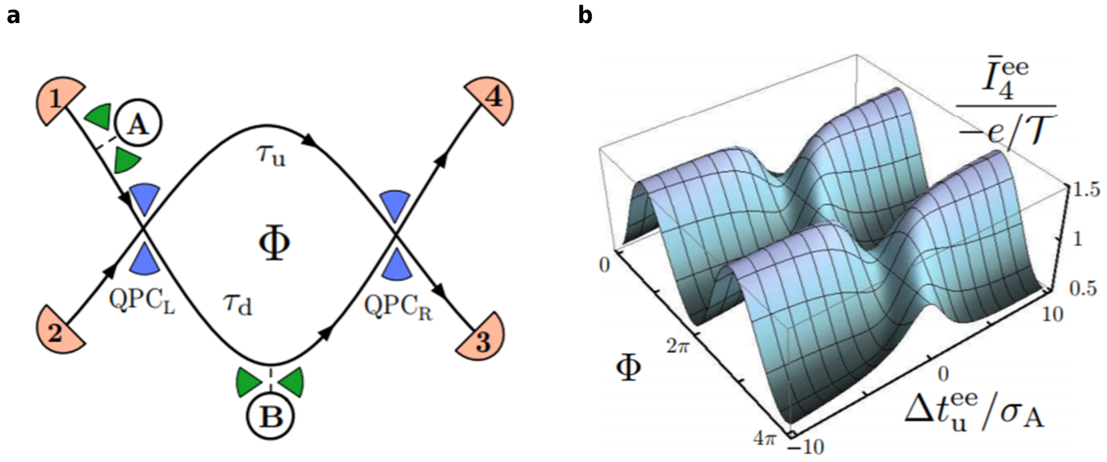

**Figure 7.1. | Electronic Mach Zehnder interferometer and current-phase relations.** **a**, Scheme of a time-resolved electronic interferometer with two paths, a single electron source, point contacts and (pico second) current meters. **b**, Simulation of the current correlations dependent on the Aharonov Bohm phase or time difference between two electrons in upper and lower arm. Reprinted figures with permission from [145]. Copyright (2015) by the American Physical Society.

wave functions in the arms[145]. A direct example to analyze a wave function would be probing phase shifts using the Leviton wave function measured during this project. If two sources (A, B) injecting into the upper and lower arm can be synchronized, a phase shift dependent signal can be detected in the time-resolved average current signal. Therefore, Levitons could be prime candidates for the efficient control of conditional phase shifts on (electrically interfaced) quantum bit states on picosecond time scales[66]. Partitioning the electronic wave functions at high magnetic fields at a quantum point contact splits the wave functions into fractions. Thus, the Levitons also could be used to directly probe more complex topological states in 2D and electronic quantum materials like fractionalized electronic states or anyonic states[89]. Interesting electronic wavefunctions like Majorana states could then be characterized at the nano scale by their current phase relation in a time-resolved manner.

In conclusion, progress in quantum-electronic pulse control is required to advance technology in our rapidly changing digital age. It is definitely worth progressing in each of the directions mentioned above, since there are still many exciting aspects to be discovered around the project presented here on ultra-fast pulse control of electronic wave functions.

# A

# SUPPLEMENTARY INFORMATION

Open science is also providing a clear overview about basic sources and materials useful for your work. Consequently, I try to also list up supplementary information about materials, software and methods.

## A.1 LIST OF TOOLS AND MATERIALS

The list is given in the format: ⟨type/name of device⟩ - ⟨producer⟩ : ⟨specific label⟩

— Arbitrary Waveform Generator - Tektronix : AWG7000

— Real-time Oscilloscope - LeCroy : WaveExpert 100H

— Noise Spectrum/Dynamic Signal Analyzer - Agilent (formerly HP): 35670A

— Lock-In Amplifier - Signal Recovery : SR7280, SR7265

— RF source - Rohde & Schwarz : SMF100A

— RF source - Agilent : E8257D

— PLL RF source - Texas Instruments : LMX2595

— Clock Synchronizer Jitter Cleaner - Texas Instruments : LMK0483

— Multimeter 8.5 digits - Keysight (formerly HP) : 3458A

— DAC built at electronics workshop of Institut Néel

- ADC - National Instruments: PXI-6722

Tools used during the fabrication processes:

- Scanning electron microscope for nano imaging - ZEISS : ULTRA plus FESEM
- Stylus Profilometer for edge scans - Veeco : Dektak 6M
- Thin film interferometer for resist check - Ocean Optics : NanoCalc
- 3D Optical profiler for height profiles - Bruker : Contour GT-K
- Evaporator for thin film deposition - PLASSYS : MEB550S
- Rapid thermal annealing for ohmic contacts - Jipelec : JetFirst 150 RTP
- Laser system for optical lithography - Heidelberg Instruments : DWL 66FS
- Electron beam machine for nano lithography - NANOBEAM : nB5
- Wire bonder for micro wire contacts to sample chip - Westbond : 7476E-79

## A.2 OPEN HARDWARE

### A.2.1 *Electronics at low temperatures*

It can be useful to know in advance which electronic devices work as expected at cryogenic temperatures. A quick test can be done by cooling down a test chip to liquid nitrogen 77 K. The following summarizes which commercial components[34] and materials[60] should be working close to the specifications at low cryogenic temperatures. Parts of the list can also be found online at the CERN open hardware electronic design wiki[17]:

- Thin film metal resistors[155] with a temperature coefficient below 25ppm work (e.g. Panasonic ERA3 series)
- Ceramic capacitors[135], only NP0 dielectrics do not vary their dielectric properties down to low temperatures (e.g. Kemet C series)

- Plastic capacitors usually work fine. Panasonic ECPU are a good SMD series with PPS dielectric - others should be fine too (PET or PP).
- Ceramic chip inductors[142] (Coilcraft 1206CS series up to around 800 nH)
- Standard FR4 PCB material[60] works at cryogenic temperatures
- Rogers RO4350B PCB dielectric is more stable at low temperatures and useful for high frequency boards
- Tin/lead solder and also lead-free solder[60]
- Most signal MOSFETs
- Many CMOS ICs[34] work as well, including digital logic and a few op amps
- CMOS multiplexers (e.g. TC74HC4051)
- Some SiGe transistors[177] work and even become better (lower noise, higher gain and bandwidth)
- Schottky diodes usually work, their forward voltage drop increases.
- Small signal relays usually work (e.g. Omron relay).
- Circulators
- LEDs work, also with increased Vf and brightness

Electronic devices which do not work (close to the specifications) are:

- Thick-film resistors[33] made of RuO2 go up in resistance and can thus be used for thermometry[61].
- Bipolar Si transistors and diodes.
- Phase locked loops on ultra-fast time scales.
- Most ferromagnetic materials have a strong temperature dependence (e.g. ferrite cores).
- Electrolytic capacitors.
- High-valued capacitors with X7R dielectric and others don't work[74].

- Power supplies, reference voltages should be placed outside of the cryogenic refrigerator due to for instance bipolar transistors and high power components therein, which need specialized design techniques for cryogenic applications[124].

## A.3 FABRICATION

### A.3.1 *Optical Laser Lithography*

- Cleaning of the sample chip: Acetone in low-power ultrasound bath 1 min, isopropyl alcohol (IPA) 30 s, Blow-dry with clean Nitrogen
- Pre-bake on hot plate 30 s at 115 °C
- Spin coating resist S1805 (MICROPOSIT) : 6000 rpm, acceleration 6000,
- Post-bake after coating 115 °C for 1 min (Thickness: 400-450 nm with NanoCalc Ocean Optics interferometer)
- Check clean resist surface, alignment, rotation, origin offsets and laser power
- Exposure of pattern with laser (Heidelberg Instruments DWL 66FS) using HQ mode, Typical laser power: 85%
- Development of resist: Dip in deionized water : micro developer concentrate (MICROPOSIT) (1:1) for 1 min, Rinse in deionized water for 1 min
- Final check of the developed pattern at optical microscope, use only UV filtered light during all steps.

### A.3.2 *Mesa Etching*

- Preparation of (inverse) mesa pattern by optical laser lithography
- Synthesis Piranha acid: Mix 25 mL of DI water $H_2O$ with 5 mL of sulfuric acid $H_2SO_4$ and add 1 mL of peroxide $H_2O_2$ (25:5:1)

- Cool down solution at least 1.5 h and check etch rate with GaAs test chip (Veeco Dektak 6M Stylus Profilometer)
- Etching: Dip HEMT sample into acid 12-15 s with a typical etch rate of ≈ $7\,\mathrm{nm\,s^{-1}}$
- Rinse in DI water.

### A.3.3 *Ohmic Contacts*

- Preparation of contact pattern by optical laser lithography
- Evaporation 5 nm nickel (Ni) + 60 nm germanium (Ge)+ 120 nm gold (Au) + 10 nm Ni + 100 nm Au (PLASSYS MEB550S)
- Lift-off in Acetone for few hours and use pipette and/or low-power ultrasound 5 s to remove all resist.
- Rapid thermal annealing at 450 °C for 1 min.

### A.3.4 *Large Schottky gates and alignment marks*

- Preparation of contact pattern by optical laser lithography
- Evaporation 20 nm titanium (Ti) + 100 nm Au (PLASSYS MEB550S)
- Lift-off in Acetone for few hours and use pipette and/or low-power ultrasound 5 s to remove all resist.

### A.3.5 *Electron beam lithography*

- Cleaning of the sample chip: Acetone in low-power ultrasound bath 1 min, IPA 30 s, Blow-dry with clean Nitrogen

- Pre-bake on hot plate 30 s at 115 °C
- Spin coating resist Polymethyl methacrylate alias acrylic glass (PMMA) 2% with anisole thinner (MicroChem Corp.) : 4000 rpm, acceleration 4000, 30 s
- Post-bake after coating 180 °C for 5 min (Thickness: 70 nm)
- Check clean resist surface, alignment, rotation, origin offsets and dose rate
- Exposure of pattern by electron beam (NANOBEAM nB5) using low current mode: Typical dose condition: $11\,\mathrm{C\,m^{-2}}$ at 100 kV
- Development of resist: 30 s in methyl isobutyl ketone (MIBK) : IPA (1:3) then rinse in IPA for 1 min.

### A.3.6 *Small sub-micron gates and contacts*

- Preparation of pattern by electron beam lithography
- Evaporation 3 nm Ti + 14 nm Au
- Lift-off in Acetone for few hours and use pipette and/or low-power ultrasound 5 s to remove all resist.

### A.3.7 *Small sub-micron isolating bridge patch*

- Cleaning of the sample chip: Acetone in low-power ultrasound bath 1 min, IPA 30 s, Blow-dry with clean Nitrogen
- Pre-bake on hot plate 30 s at 115 °C
- Spin coating resist SU8 2000 (MicroChem Corp.) : thinner, anisole (1 : 1), speed 3000 rpm, acceleration 3000 for 1 min
- Exposure with electron beam (NANOBEAM nB5): Typical dose condition: 0.3 - $0.6\,\mathrm{C\,m^{-2}}$ at 100 kV
- Post-bake after exposure 95 °C for 3 min

— Development: Dip in SU8 Developer 20 s, rinse in IPA 40 s.

### A.3.8 *Small final bridge gold patch*

— Cleaning of the sample chip

— Spin Coating PMMA 4% (MicroChem Corp.) speed 3000 rpm, acceleration 3000

— Post-bake 180 °C for 3 min

— Repeat coating and bake to deposit two resist layers (Thickness: 400 nm)

— Exposure by electron beam (NANOBEAM nB5), typical dose $11\,\mathrm{C\,m^{-2}}$ at 100 kV

— Development of resist: 30 s in MIBK : IPA (1:3) then rinse in IPA for 1 min.

— Angle Evaporation (PLASSYS MEB550S): 10 nm Ti at −7.5° , 10 nm Ti at 7.5° Ti, 10 nm Ti at 0°, 25 nm Au at −7.5° , 25 nm Au at 7.5° , 200 nm Au at 0° (tilt with respect to short bridge connection axis)

— Lift-off in Acetone for few hours and use pipette and/or low-power ultrasound 5 s to remove all resist.

### A.3.9 *Bond wire interconnects*

Gold bond wire with a diameter $d = 25\,\mu\mathrm{m}$ at West Bond 7476E-79 connecting to bond pads $\geq 80 \times 80\mu\mathrm{m}^2$ with the settings:

— First wedge bonding: power 300, time 30ms, force high

— Second wedge bonding: power 350, time 30ms, force low

weight 24g, loop height 50 (1270 μm), wire pull 24, wire tail 30, dual force on, ultrasound power during feed 200, clamp home position 30. All PCB lines grounded the wire bonder during bonding.

### A.3.10 *Mini SMP connection at PCB*

- miniSMP right angle connectors (Rosenberger 18S141-40ML5)
- Home made Semi rigid miniSMP coaxial lines (Rosenberger 18K102-271L5)
- RF solder paste (Henkel LOCTITE GC 10, baking 120s at 160 °C 300s at 300 °C)
- Additional tin-solder spot at the ground plane back side and the center pin of the right-angle connector for good mechanical fixation at low temperatures and reconnecting the RF cables.

## A.4 FROM COMPLEX FOURIER SERIES TO FOURIER TRANSFORM

There are equivalent ways to write a complex Fourier series reconstruction of a signal $v(t) = r_N(t)$:

$$r_N(t) = \sum_{n=-\infty}^{\infty} c_n \exp(2\pi int/T) = \frac{a_0}{2} + \sum_{n=1}^{\infty} A_n \cos(2\pi nt/T + \phi_n), \tag{A.1}$$

with amplitude $A_n$ and phase offset $\phi_n$

$$A_n = \sqrt{a_n^2 + b_n^2} \tag{A.2}$$

$$\phi_n = \tan^{-1}(-b_n/a_n) \tag{A.3}$$

using the complex Fourier coefficient, with odd and even part:

$$c_n = \int_{-\frac{T}{2}}^{\frac{T}{2}} v(t) \exp(-2\pi int/T)\, \mathrm{d}t = \begin{cases} \frac{a_n - jb_n}{2} & n > 0 \\ \frac{a_0}{2} & n = 0 \\ \frac{a_n + jb_n}{2} & c < 0 \end{cases} \tag{A.4}$$

For an infinite period $T \to \infty$ $c_n$ is a discrete Fourier transform.

## A.5 CAUCHY DISTRIBUTION FUNCTION AND FOURIER TRANSFORM PROPERTIES

A Lorentzian function is also known as a Cauchy probability distribution with[179]:

$$P(x) = \frac{1}{\pi} \frac{\epsilon}{(x-m)^2 + \epsilon^2}, \tag{A.5}$$

The sum of $n$ Lorentzian functions is also a Cauchy distribution[179]:

$$P_n(x) = \mathcal{F}_t^{-1}[\Phi(t)^n](x) = \frac{1}{\pi} \frac{\frac{1}{2} n\Gamma}{(\frac{1}{2} n\Gamma)^2 + (x - nm)^2} \tag{A.6}$$

where $\epsilon$ is the half width at half maximum and $m$ the median value where the peak is centered at. A Dirac delta distribution can be approximated in the limit $\epsilon \to 0$ with $\epsilon = \frac{1}{2} \cdot \Gamma$ related to $\Gamma$ the full width at half maximum a of a Lorentzian distribution:

$$\delta(t) = \frac{1}{\pi} \lim_{\epsilon \to 0} \frac{\epsilon}{t^2 + \epsilon^2} \tag{A.7}$$

The delta distribution has a Fourier transform pair:

$$\mathcal{F}\left[\delta(t-a))\right](f) = e^{-2\pi i f \cdot a}. \tag{A.8}$$

## A.6 GAUSSIAN RESPONSE AND ERROR FUNCTION

The error function is defined as the integral over a Gaussian $G(x)$ via:

$$G(x) = A \cdot \mathrm{e}^{-(x-\mu)^2/2\sigma^2} \tag{A.9}$$

$$\int G(\tilde{x})\,\mathrm{d}\tilde{x} = a \cdot \operatorname{erf}\left((x-\mu)/c\right) + d, \tag{A.10}$$

where $A, a, d$ are constants, $\mu$ is the center expectation value, $\sigma$ is the standard deviation relating to the full width half maximum $\Gamma$:

$$\Gamma = 2\sqrt{2\ln 2} \cdot \sigma, \tag{A.11}$$

and the broadening $c$ of the error stepfunction:

$$c = \frac{\Gamma}{2\sqrt{\ln 2}} \tag{A.12}$$

The rise time $t_R$ between the 10% value $G(t_1) = 0.1 \cdot a/2$ and the 90% value $G(t_2) = 0.9 \cdot a/2$ of the error stepfunction can be calculated as:

$$t_R = t_2 - t_1 = \frac{4}{\sigma} \operatorname{erf}^{-1}(0.8) \tag{A.13}$$

using that the step function has odd symmetry around the origin $\mu = 0$:

$$\operatorname{erf}(-t) = -\operatorname{erf}(t) \tag{A.14}$$

The convolution of two Gaussians leads to a Gaussian with broadened pulse width:

$$\sigma_{g*f} = \sqrt{\sigma_g^2 + \sigma_f^2}. \tag{A.15}$$

The Fourier transform pair of a Gaussian response function in time domain is also a Gaussian function in frequency domain $\mathcal{F}\left[\mathrm{e}^{-at^2}\right](f) = \sqrt{\frac{\pi}{a}}\mathrm{e}^{-\pi^2 f^2/a}$.

## A.7 STRIPLINE DESIGN CALCULATION

The dispersion of striplines can be calculated using conformal mappings of the stripline or waveguide geometry. The mapping of a coplanar waveguide above a ground plane with width $W$, slot width $s$ and substrate hight $h$ (as shown in figure 3.2a) can be well described using an effectiv dielectric permittivity[173] and the following analytical expressions:

$$\epsilon_{eff} = 1 + q \cdot (\epsilon_r - 1), \tag{A.16}$$

with filling factor:

$$q = \frac{\frac{K(k_3)}{K'(k_3)}}{\frac{K(k_1)}{K'(k_1)} + \frac{K(k_3)}{K'(k_3)}}, \tag{A.17}$$

and the ratio $K(k)/K^{'}(k)$ of the complete elliptic integral of first kind $K(k)$ and it's complement $K'(k)$ well approximated by:

$$\frac{K(k)}{K'(k)} = \begin{cases} \frac{\pi}{\ln\left(2\frac{1+\sqrt{k'}}{1-\sqrt{k'}}\right)} & 0 \geq k \geq 1/\sqrt{2} \\ \frac{\ln\left(2\frac{1+\sqrt{k}}{1-\sqrt{k}}\right)}{\pi} & 1/\sqrt{2} \geq k \geq 1 \end{cases} \tag{A.18}$$

where $k^{'}$ is the complementary modulus:

$$k^{'} = \sqrt{1-k^2}, \tag{A.19}$$

$$k_1 = \frac{W}{W+2s}, \tag{A.20}$$

$$k_2 = \frac{\sinh\frac{\pi W}{4h}}{\sinh\frac{\pi\cdot(W+2s)}{4h}}, \tag{A.21}$$

and

$$k_3 = \frac{\tanh \frac{\pi W}{4h}}{\tanh \frac{\pi \cdot (W+2s)}{4h}}, \tag{A.22}$$

leading to the impedance of a coplanar waveguide above a ground plane:

$$Z_{CPW} = \frac{60\pi}{\sqrt{\epsilon_{eff}}} \frac{1}{\frac{K(k_1)}{K'(k_1)} + \frac{K(k_3)}{K'(k_3)}} \tag{A.23}$$

## A.8 SOLID STATE QUANTUM INFORMATION HARDWARE

The data state for processing quantum information is the quantum bit (qubit). A qubit encodes the classical bits of information 0 and 1 in a quantum mechanical basis $|0\rangle$ and $|1\rangle$. The quantum mechanical bit system can be in a superposition of the two states $|0\rangle$ and $|1\rangle$ with an arbitrary complex phase coefficient between the states. When the total quantum state can be described by a set of complex number of each basis state, the quantum state is said to be coherent. In a theoretical sense, the coherence can be described by complex off-diagonal elements of the density matrix $\rho_{mn}$[86]. Quantum interference, superposition, and entanglement are only measurable in coherent quantum systems. The complex phase space accessible by quantum superposition and entanglement allows quantum computers to do massively parallel calculations. The quantum computer then works by preparing a superposition $\frac{1}{\sqrt{2^n}} \Sigma_x |x\rangle |f(x)\rangle$, where $f(x)$ is the function of interest to be calculated and $x$ varying over the possible solutions to the problem[128]. The phase space or the theoretical computational power grows exponentially $2^n$ if $n$ qubits can be prepared in the way noted above. A multi-qubit state is called entangled, if the state of each qubit cannot be described individually. Entangled states are difficult to describe efficiently by classical computational methods, since the state cannot be factored as for instance the tensor product of the individual states[132]. Entanglement can therefore be seen as a resource for providing a quantum advantage for computation and simulations. The parallelism of many entangled qubits is a very powerful and fascinating concept for information processing. Recognizing the power of quantum information processing[129], researchers started to think about hardware for quantum computing in the nineties[39,112]. Solid-state based quantum computation using a semiconductor quantum dot memory was proposed[112]. The hardware of a spin-based quantum computer should fulfill the key criteria[50]:

1. A scalable physical system with well-characterized qubits
2. The ability to initialize the state of the qubit to a simple state like $|000...\rangle$
3. An universal set of quantum logic gates
4. Long relevant decoherence times, much longer than the gate-operation time ($10^4$ quantum operations before reset)
5. A qubit-specific measurement capability
6. The ability to inter-convert stationary and flying qubits
7. The possibility to transmit flying qubits between distant locations

A lot of these pioneering criteria could be achieved to develop solid-state qubit devices for quantum computing[98,170]. But still, there is no qubit approach fulfilling all the norms at once without having its drawbacks. Full-scale quantum computers with error correction are largely theoretical devices. Thus, the criteria for building useful quantum computing hardware stay relevant and are needed to describe challenging problems even after more than 20 years of advances and developments. The most considerable hardware challenges are nowadays scaling (1), fast coherence-protected operation (4) and long distance quantum communication (6,7). Keeping coherent quantum information and even more transferring solid-state qubits on-the-fly is very demanding. Hybrid superconductor-semiconductor resonator-qubit structures have recently been investigated to overcome material challenges and to introduce strongly coupled long-range connect-ability[76,105,121,149,150].

## A.9 SOFTWARE

A short list of software and related tutorials used during this thesis follows. The instruments' drivers and LabVIEW environment used during the thesis are linked and shared in a GitHub directory[137]. Data analysis is mainly performed with Python using standard least-squares fitting methods and propagation of uncertainty[163]. The main open source packages used for calculations and data analysis with python are matplotlib, numpy, pandas, seaborn, scipy and skrf[140]. Numerical software packages used for device, chip design and transport simulations are COMSOL[43], nextnano[26], LTspice[3], Qucs[186] and kwant[71].

# GLOSSARY

## ABBREVIATIONS

| | |
|---|---|
| $H$ | Hamiltonian operator |
| 0D | Zero-dimensional or point-like |
| 1D | One-dimensional |
| 2D | Two-dimensional |
| 2DEG | Two-dimensional electron gas |
| 3D | Three-dimensional |
| AC | Alternating electric current |
| ADC | Analog-to-digital converter |
| AlAs | Aluminium arsenide |
| AlGaAs | Aluminium gallium arsenide |
| Au | Gold |
| AWG | Arbitrary wave function generator |
| DAC | Digital-to-analog converter |
| DC | Direct electric current |
| DEMUX | Demultiplexer |
| FPGA | Field-programmable gate array |
| GaAs | Gallium arsenide |

| | |
|---|---|
| Ge | Germanium |
| HEMT | High-electron-mobility transistor |
| IPA | Isopropyl alcohol |
| IV | Current-to-voltage |
| LDO regulator | Low-dropout regulator |
| MIBK | Methyl isobutyl ketone |
| MUX | Multiplexer |
| Ni | Nickel |
| PCB | Printed circuit board |
| PID | Proportional-integral-derivative |
| PLL | Phase-locked loop |
| PMMA | Polymethyl methacrylate alias acrylic glass |
| QD | Quantum dot |
| QPC | Quantum point contact |
| RF | Radio frequency |
| Si | Silicon |
| SMD | Surface mount device |
| TDR | Time domain reflectometer |
| Ti | Titanium |
| VCO | Voltage-controlled oscillator |

## PHYSICAL CONSTANTS

| Name | Symbol | Numerical value | Unit |
|---|---|---|---|
| Number $\pi$ | $\pi$ | 3.14159265358979323846 | |
| Number e | e | 2.71828182845904523536 | |
| Elementary charge | $e$ | $1.602176634 \cdot 10^{-19}$ | C (def) |
| Speed of light in vacuum | $c$ | $2.99792458 \cdot 10^{8}$ | m/s (def) |
| Magnetic constant | $\mu_0$ | $\frac{2h\alpha}{ce^2} \approx 4\pi \cdot 10^{-7}$ | H/m |
| Permittivity of the vacuum | $\varepsilon_0$ | $\frac{1}{c^2\mu_0} \approx 8.854187817 \cdot 10^{-12}$ | F/m |
| $(4\pi\varepsilon_0)^{-1}$ | | $8.9876 \cdot 10^{9}$ | $\mathrm{Nm^2C^{-2}}$ |
| Planck's constant | $h$ | $6.62607015 \cdot 10^{-34}$ | Js (def) |
| Dirac's constant | $\hbar = h/2\pi$ | $1.054571800 \cdot 10^{-34}$ | Js |
| Bohr magneton | $\mu_B = e\hbar/2m_e$ | $9.2741 \cdot 10^{-24}$ | $\mathrm{Am^2}$ |
| Avogadro's constant | $N_A$ | $6.02214076 \cdot 10^{23}$ | $\mathrm{mol^{-1}}$ (def) |
| Boltzmann's constant | $k = R/N_A$ | $1.380649 \cdot 10^{-23}$ | J/K (def) |
| Electron mass | $m_e$ | $9.10938356 \cdot 10^{-31}$ | kg |

**Table A.2. | Values of constants** following the redefinition draft of the SI units by the International Bureau of Weights and Measures in 2019 [25].

*«Veritas vos liberabit.» :*
*"The truth shall set you free."*

– Motto of Université Grenoble Alpes

# B

# RÉSUMÉ SUBSTANTIEL

## B.1 INTRODUCTION ET MOTIVATION

En physique quantique, la nature discrète et quantifiée d'une propriété telle que l'énergie ou la matière détermine le comportement d'un processus étudié. Au début du XXe siècle, la physique quantique s'est concentrée sur le développement et la mise à l'essai de la nouvelle théorie quantique. Des esprits brillants comme Albert Einstein, Marie Curie, Niels Bohr, Max Planck et bien d'autres ont discuté de façon très vivante à la conférence Solvay de 1927 sur "les électrons et les photons" et, fondamentalement, une nouvelle compréhension du comportement des particules basé sur un formalisme ondulatoire a été présenté. À l'époque où les fondements de la mécanique quantique ont été posés est souvent appelé la première révolution quantique. De nos jours les résultats expérimentaux ont vérifié une grande partie des premières théories quantiques et l'approche quantique pour décrire la nature est bien acceptée. Une partie de la physique peut donc se développer davantage vers des technologies quantiques appliquées. La technologie de pointe atteint des limites fondamentales, où contrôler les processus quantiques à très basse température, à haute résolution et à petite échelle nanométriques de longueur devient indispensables. La fonctionnalité quantique imposée au-delà des limites de la physique classique marque le début d'une nouvelle ère technologique appelée la seconde révolution quantique. Quelques exemples célèbres de fonctionnalité quantique amélioré sont les lasers cohérents pour spectroscopie et pour la communication rapide de données, la résonance magnétique nucléaire pour la détection et l'imagerie, les horloges atomiques pour le chronométrage de précision, les canaux quantiques à effet Hall définissant un étalon de résistance, les dispositifs supraconducteurs à effet Josephson pour un contrôle précis du flux formant également un étalon de tension et l'effet de tunnel dans les dispositifs à transistors. Les interactions de charge et le bruit limitent le fonctionnement quantique cohérent de ces dispositifs. Un contrôle électronique à haute fréquence et aussi à bruit minimal dans les conducteurs proches est crucial pour des opérations quantiques et des lectures d'information rapides et efficaces. C'est pour ça que le contrôle électronique rapide et silencieux est optimisé sur puce et à basse température pendant ce projet de thèse. La cohérence signifie aussi que les phases relatives des états sont expérimentalement accessibles, par exemple en cas d'une expérience d'interférence. Un moyen possible de sonder la cohérence de charge d'un paquet d'ondes électroniques est l'injection d'une impulsion très courte de tension (demi-largeur maximale d'environ 100 ps) dans un interféromètre à deux voies. Le contrôle rapide d'impulsions à faible nombre d'électrons peut être décrit de manière efficace de manière optique en forme d'onde. Par la suite les connaissances de base en physique du transport quantique seront passées en revue.

## B.2 TRANSPORT QUANTIQUE ET OPTIQUE ÉLECTRONIQUE

Les expériences d'optique électronique se sont développées rapidement au cours de la dernière décennie en raison de nouvelles méthodes expérimentales d'isolement et de transfert d'électrons individuels. Les analogues électroniques aux interféromètres de Mach-Zehnder[83], Hanbury Brown-Twiss[126], Hong-Ou-Mandel[30] et quantum la tomographie de la fonction d'onde électronique[87] ne sont que quelques points clé de ces fortes avancées expérimentales. Il existe plusieurs façons d'injecter des charges individuelles dans les conducteurs quantiques[14,158]. Les sources d'électrons uniques couramment utilisées sont le tourniquet à confinement quantique[169], un seul électron assisté par une onde sonore de surface (SAW)[19] et des impulsions de tensions courtes de forme lorentzienne appelées Levitons[107]. L'injection d'une impulsion de tension de forme de Lorentzienne, dépendante du temps, forme un électron cohérent dans un guide d'ondes électronique :

$$V\left(t\right)=\frac{2\hbar}{e}\frac{\tau_e}{\left(t-t_0\right)^2+\tau_e},\tag{B.1}$$

où chaque impulsion porte un flux quantique proportionnel à l'intégrale de temps de l'impulsion :

$$\int V\left(t\right)dt=\frac{h}{e}.\tag{B.2}$$

La fonction d'onde électronique cohérente ci-dessus est aussi appelée Leviton[82,90,107]. Le Leviton a une forme lorentzienne dans le domaine temporel :

$$\Psi^{(e)}_{Levitov}\left(t\right)=\sqrt{\frac{\tau_e}{2\pi}}\frac{1}{t+i\tau_e}\tag{B.3}$$

et suit une exponentielle décroissante dans le domaine énergétique avec 1 k n électrons[58] La fonction de Wigner fournit puis un cadre de travail pour faire une analyse quantique d'une mesure électronique quantique[36]. Les levitons sont injectés directement sur la distribution thermique de la mer de Fermi. Par conséquent, la température de l'expérience présentée ici doit être basse par rapport à la fréquence de l'injection étudiée :

$$hf > k_B T_{el}, \tag{B.4}$$

où $T_{el}$ est une température de base électronique basse et $f$ est la fréquence de l'injection. En d'autres termes, cela signifie que l'effet électronique quantique en excès doit pouvoir être distingué de la contribution thermique à l'état de la mer de Fermi. Les lévitons dans un conducteur quantique à des températures de l'ordre de quelques mK montrent un comportement quantique sur des échelles de temps ultra-rapides en picosecondes et la fonction Wigner a été mesurée par spectroscopie photo-assistée du bruit de grenaille[87]. De plus, une relation de Josephson pour l'apparition de l'excès de bruit de grenaille aux fréquences micro-ondes (GHz) permet d'analyser expérimentalement des signatures de bruit dépendantes de la fréquence d'états électroniques topologiques complexes tels que récemment mesurés avec des états quantiques de Hall fractionnaires[89]. Un dispositif mis au point pour l'échantillonnage direct ultra-rapide à l'intérieur du conducteur quantique[147] qui permet ensuite de créer un laps de temps d'une impulsion électronique telle qu'un Léviton à des températures cryogéniques est présenté ultérieurement dans la partie expérimentale.

## B.3 STRUCTURE DES DISPOSITIFS ET INTERCONNEXIONS

Les puces à haute mobilité sont produits en utilisant des techniques de croissance d'épitaxie par jet moléculaire de haute qualité[117,153]. De faibles taux de croissance de seulement 0,1 à deux monocouches par seconde accessibles en épitaxie par jet moléculaire permettent de produire des interfaces atomiquement lisses. La concentration d'impuretés et de défauts peut être très faible dans des conditions de vide très élevé. Les meilleures conditions de vide, des transitions d'interface nettes réglables par le taux de croissance et une faible contamination par défaut forment la base pour atteindre des mobilités électroniques très élevées. Les hétérostructures AlGaAs sont le seul système matériel où de telles mobilités peuvent être atteintes. L'empilement d'une hétérostructure typique à haute mobilité d'électrons AlGaAs est schématiquement représenté sur la figure 3.1a et 2.3d. Les grilles, qui sont évaporées en surface, définissent des grilles de Schottky pour l'épuisement du 2DEG, les lignes de transmission pour l'injection des hautes fréquences, pour l'échantillonnage sur un QPC et les contacts ohmiques pour la lecture et l'établissement d'une référence de fond de charge stable. Les signaux à haute fréquence doivent être envoyés vers les lignes quantiques nanométriques à l'aide de lignes de transmission. Une structure de guide d'onde coplanaire conique montrée dans la figure 3.2a est utilisée comme ligne de transmission. Elle se compose d'un conducteur central de largeur W et d'épaisseur Tmet et de longueur L, de deux fentes d'air co-parallèles de largeur S et de plans de masse des deux côtés et à une hauteur de substrat H sous les bandes métalliques pour confiner et protéger l'onde en mouvement. Ces paramètres dimensionnels sont ensuite également utilisés pour simuler les profils de champ et l'impédance du guide d'onde coplanaire[43,173]. L'effet des grilles d'épuisement Schottky peut être simulé électro-statiquement à l'aide de l'équation de Poisson et d'un solveur numérique pour cartographier la géométrie des grilles[71]. Les grilles y sont discrétisées à l'aide de rectangles et de polygones[46,174]. L'équation de Poisson est ensuite résolue et ajustée à l'aide d'estimations réalistes des paramètres du dispositif. La figure 3.4 montre la carte potentielle coupée à la hauteur de la feuille 2DEG. Les grilles Schottky définissent un trajet supérieur et inférieur pour former un interféromètre. La coupe horizontale à travers la carte du potentiel à $y = 0$ dans la figure 3.4 montre l'île centrale et la région à faible potentiel couplée par effet tunnel. Les bras de l'interféromètre à deux voies peuvent être fermé par des contacts ponctuels. L'effet tunnel d'électrons entre les bras peut être accordé en appliquant une tension à la grille fendue telle qu'elle est représentée par les coupes verticales sur le côté droit de la figure 3.4.

## B.4 CONTRÔLE DES IMPULSIONS ET DE LA STABILITÉ À FAIBLE BRUIT

Le matériel quantique atteint des limites lorsqu'une seule fonction d'onde est confinée et détectée à une très petite échelle de longueur de quelques dizaines de nanomètres seulement. De petites variations des tensions de grille et des signaux parasites peuvent nuire au contrôle d'un état quantique puisqu'ils créent des effets de champ électrique relativement importants à des échelles nanométriques ($|\mathbf{E}| \propto 1/|\mathbf{r}|$). Par conséquent, la caractérisation du bruit et de la stabilité d'un dispositif électronique pour tester le matériel quantique est cruciale pour un fonctionnement fiable et cohérent. Défauts dans les interfaces atomiquement pointues de AlGaAs HEMTs sont réduits. L'utilisation d'un HEMT avec une faible densité de défauts et l'augmentation de la capacité de la source de grille $C_{gs}$ pour faire la moyenne des fluctuations peut à cette fin réduire le niveau de bruit d'un préamplificateur cryogénique à $200\,\mathrm{pV}\sqrt{\mathrm{Hz}}$[84]. Le contrôle des matériaux jusqu'au défaut unique et le contrôle cryo-électronique à très faible bruit est l'un des défis majeurs pour améliorer et comprendre le fonctionnement des dispositifs quantiques à l'état solide. La spectroscopie de bruit utilisant le HEMT cryogénique connecté à une pointe de microscope à effet tunnel à balayage peut cartographier l'origine du bruit sur une échelle sub-nanométrique pour étudier par exemple les supraconducteurs à haute température[12]. La zone de travail de l'amplificateur cryogénique HEMT stabilisé permet d'opérer l'amplificateur même au stade 1K du frigo à dilution. La largeur de bande du dispositif testé connecté à la chaîne d'amplification est alors limitée par la capacité de cette ligne coaxiale. La ligne coaxiale (ligne bleue dans la figure 4.10) avec l'impédance au kHz la plus élevée pour l'isolation thermique mais de bonnes propriétés de transmission à hautes fréquences dues à la faible capacité par mètre sont choisies avec un diamètre du noyau constantan $d_c = 70\,\mu\text{m}$ et un diamètre capillaire en acier inoxydable $D_d = 400\,\mu\text{m}$. L'amplificateur a un gain plat jusqu'à 300 kHz mesuré à 4K en utilisant le câble coaxial constantan. Les autres combinaisons de matériaux testées pour la construction d'une ligne coaxiale à basse température sont résumées dans le tableau 4.1. Le signal en bande de base est dans notre configuration de mesure également acquis sur une partie plate de la chaîne de l'amplificateur telle que mesurée dans la figure 4.8b. Le signal en bande de base à la fréquence de modulation $\omega_{LI}$ est ensuite amplifié par un amplificateur de deuxième étage (NF SA-421-F5) stabilisé à température ambiante. Le signal de sortie de l'amplificateur du deuxième étage est finalement numérisé par une détection homodyne (DSP Lock-In 7280).

## B.5 CONTRÔLE D'IMPULSION ULTRARAPIDE À BASSES TEMPÉRATURES

L'échantillonnage électronique nécessite des impulsions ultra-rapides et des délais précis. La limite de haute fréquence de l'acquisition de traces de temps est obtenue par échantillonnage optoélectronique sur des échelles de temps inférieures à la picoseconde[167]. L'échantillonnage optoélectronique de tension utilise un laser pulsé frappant un commutateur photoconducteur dans un semiconducteur pour créer des pulseurs et des échantillonneurs. La puissance moyenne du laser de pompe pour l'ouverture de l'interrupteur (généralement > mW) est un facteur limitant pour le fonctionnement à basse température des interrupteurs à commande ultra-rapide, puisque la puissance de refroidissement (généralement $<$ mW) d'un réfrigérateur à dilution standard au plus bas niveau de température doit être suffisante. Ainsi, nous commençons par étudier l'échantillonnage commandé par tension à basse température dans ce projet beaucoup plus économe en énergie. La figure 5.8b montre comment l'échantillonnage est réalisé à basse température. Les impulsions sont injectées dans un conducteur quantique qui peut être échantillonné en ouvrant momentanément un interrupteur RF QPC. L'échantillonneur QPC est commandé par une impulsion de commande d'échantillonneur temporisée produite par un AWG (Tektronix AWG7000 série 24GS/s). La séquence d'impulsion est modulée à une fréquence qui peut être utilisée pour la détection de verrouillage (12kHz). La figure 5.13 montre comment la forte non-linéarité de la courbe QPC IV permet de créer un échantillonneur à grande largeur de bande. Le contact du point quantique a une courbe caractéristique I-V montrée dans l'encadré de la figure 5.13. L'échantillonneur applique une impulsion gaussienne avec un FWHM de 70 ps. L'impulsion gaussienne peut être désaccordée par un décalage en courant continu à l'aide d'un bias-tee (SHP 65GHz) par rapport à la position fermée du contact du point quantique ($V_{pinch} = -0.8\,\mathrm{V}$). Le produit de la fonction de conductance et de l'impulsion gaussienne peut être optimisé pour obtenir une fraction de conductance nette représentée en rouge sur la figure 5.13. Le décalage de l'impulsion par rapport au pincement des QPC n'ouvre le conducteur quantique que sur une courte échelle de temps et aiguise l'impulsion gaussienne. La tension de sortie échantillonnée Vechantillon d'un commutateur à effet de champ suit la relation[85] :

$$V_{echantillon}(t) = \int_{-\infty}^{\infty} V_{in}(\tau) h(\tau - t_S)\, \mathrm{d}\tau \tag{B.5}$$

où la tension d'entrée est obtenue par la convolution avec la fonction d'ouverture $h(t)$. La partie la plus lente (ou la partie la plus petite en bande passante) de la configuration testée domine la bande passante :

$$B_{tot} = \frac{1}{\sqrt{1/B_{probe}^2 + 1/B_{osci}^2}} \tag{B.6}$$

## B.6 LEVITONS GENERÉES PAR UN PEIGNE DE FRÉQUENCE

Un générateur de peigne à micro-ondes avec une largeur de bande multi GHz est utilisé pour créer des harmoniques pour produire une forme d'impulsion de Lorentz. Dans le domaine fréquentiel, la puissance de l'harmonique de base injectée est répartie sur les multiples harmoniques supérieurs via :

$$f_{comb} = \sum_{n} f_{base} \cdot n \tag{B.7}$$

La sortie a beaucoup de pics aux espacements de fréquence équidistants donnés par la fréquence de base $f_{base}$. Tout d'abord, les composantes de Fourier de sortie du générateur en peigne sont analysées. La sortie d'impulsions à résolution temporelle du peigne de fréquence hyperfréquence (marki NLTL-6026) est mesurée sur la figure 6.4 à une fréquence d'entrée $f_{base} = 3\,\text{GHz}$. Les données (points bleus) indiquent le train d'impulsions et la ligne rouge est l'intégrale sur la forme d'onde, formant des pas de flux par impulsion. La figure 6.4b montre la transformée de Fourier rapide (FFT) des données acquises. L'amplitude des différentes harmoniques ne décroît pas linéairement sur l'échelle dBm. Ceci peut expliquer la forme de l'impulsion qui n'est pas lorentzienne. Les harmoniques jusqu'à 48GHz contribuent à l'impulsion comme indiqué dans le spectre de Fourier (cf. figure 6.4b). Une dispersion non linéaire signifie que pour chaque entrée de fréquence différente et aussi pour différentes puissances d'entrée, la puissance de sortie des harmoniques est légèrement différente et doit être compensée en amplitude et en phase pour former un train d'impulsions spécifique. L'avantage d'utiliser un peigne de fréquence alimenté à partir d'une seule fréquence de base vient de la relation de phase verrouillée inhérente aux harmoniques de sortie donnée par la dispersion fixe du générateur de peigne. La figure 6.6 montre la sortie du générateur de peigne pour 3 GHz et 6 GHz entrée fréquence de base avec l'amplitude maximale d'impulsion 2 V (juste sous la saturation du LeCroyWaveExpert 100H). Les amplitudes de sortie suivent déjà de très près une tendance exponentielle et les impulsions de sortie semblent de forme lorentzienne pour une entrée haute fréquence de 6 GHz comme indiqué par des croix vertes. La compensation nécessaire pour obtenir une dispersion exponentielle de la fréquence de sortie (ligne cible rouge et surface en dB) est représentée par les points bleu et vert. Les amplitudes et les phases sont compensées et réglées dans une configuration de mise en forme des impulsions.

## B.7 PERSPECTIVES

Enfin, j'esquisse quelques perspectives à court terme des expériences actuelles enoptique électronique quantique. Les charges uniques peuvent produire des déphasages importants de la fonction d'onde électronique, comme l'ont montré récemment deux expériences électroniques d'interféromètre de Mach Zehnder dans le régime du courant continu[55,56]. Une extension naturelle de ces expériences est d'étudier les effets des interférences résolues dans le temps avec un interféromètre RF comme le montre la figure 7.1. Le courant de sortie moyen à résolution temporelle au contact ohmique quatre $\overline{I}_4^{ee}$ peut être mesuré par rapport à la phase Aharonov-Bohm ou à la différence de temps $\Delta t_u^{ee}$ des fonctions électroniques (électron unique) dans les bras[145]. Un exemple direct d'analyse d'une fonction d'onde serait de sonder les déphasages à l'aide de la fonction d'onde de Léviton mesurée pendant ce projet. Si deux sources (A, B) injectant dans le bras supérieur et inférieur peuvent être synchronisées, un signal dépendant du déphasage peut être détecté dans le signal de courant moyen résolu dans le temps. Par conséquent, Levitons pourraient être des candidats de choix pour le contrôle efficace des déphasages conditionnels sur des états de bits quantiques (interfacés électriquement) sur des échelles de temps picosecondes[66]. La partition des fonctions d'ondes électroniques à des champs magnétiques élevés au niveau d'un contact quantique divise les fonctions d'ondes en fractions. Ainsi, les Lévitons pourraient aussi être utilisés pour sonder directement des états topologiques plus complexes dans des matériaux quantiques 2D et électroniques comme des états électroniques fractionnés ou des états anioniques. Des fonctions d'ondes électroniques intéressantes comme les états de Majorana pourraient alors être caractérisées à l'échelle nanométrique par leur relation de phase actuelle dans un temps résolu. En conclusion, des progrès dans le domaine du control électronique quantique de l'impulsion sont nécessaires pour faire progresser la technologie dans notre ère numérique en rapide évolution. Il sera profitable de progresser dans chacune des directions mentionnées ci-dessus, car il reste encore beaucoup d'aspects passionnants à découvrir autour du projet présenté ici sur le contrôle ultra-rapide des fonctions d'onde électroniques.

# BIBLIOGRAPHY

[1] E. Afshari and A. Hajimiri, *Nonlinear transmission lines for pulse shaping in silicon*, IEEE Journal of Solid-State Circuits **40**, 744 (2005) (cit. on p. 108).

[2] E. Akkermans and G. Montambaux, *Mesoscopic Physics of Electrons and Photons* (Cambridge University Press, Cambridge, 2007) (cit. on p. 42).

[3] Analog Devices, *LTspice ciruit simulation software* (cit. on p. XIV).

[4] Ardent Concepts, *Spring Probe Connectors* (cit. on p. 78).

[5] S. Ashhab, P. C. de Groot, and F. Nori, *Speed limits for quantum gates in multiqubit systems*, Physical Review A **85**, 249 (2012) (cit. on p. 3).

[6] A. S. Averkin et al., *Broadband sample holder for microwave spectroscopy of superconducting qubits*, The Review of scientific instruments **85**, 104702 (2014) (cit. on pp. 76, 78).

[7] D. D. Awschalom et al., *Quantum spintronics: Engineering and manipulating atom-like spins in semiconductors*, Science (New York, N.Y.) **339**, 1174 (2013) (cit. on p. 67).

[8] S. Baer and K. Ensslin, « Measurement Setup Optimization for Low Electron Temperatures, » in *Transport spectroscopy of confined fractional quantum Hall systems*, edited by S. Baer and K. Ensslin, Springer series in solid-state sciences, 0171-1873 (Springer, Cham, 2015), pp. 97–122 (cit. on p. 70).

[9] L. Banszerus et al., *Ballistic Transport Exceeding 28 µm in CVD Grown Graphene*, Nano letters **16**, 1387 (2016) (cit. on p. 31).

[10] J. C. Bardin et al., *A 28nm Bulk-CMOS 4-to-8GHz <2mW Cryogenic Pulse Modulator for Scalable Quantum Computing* (cit. on p. 62).

[11] J. Basset et al., *Evaluating charge noise acting on semiconductor quantum dots in the circuit quantum electrodynamics architecture*, Applied Physics Letters **105**, 063105 (2014) (cit. on p. 58).

[12] K. M. Bastiaans et al., *Charge trapping and super-Poissonian noise centres in a cuprate superconductor*, Nature Physics **14**, 1183 (2018) (cit. on pp. 61, 64, 6).

[13] F. Bauer et al., *Microscopic origin of the '0.7-anomaly' in quantum point contacts*, Nature **501**, 73 (2013) (cit. on p. 20).

[14] C. Bäuerle et al., *Coherent control of single electrons: A review of current progress*, Reports on progress in physics. Physical Society (Great Britain) **81**, 056503 (2018) (cit. on pp. 16, 22, 3).

[15] T. Bautze et al., *Theoretical, numerical, and experimental study of a flying qubit electronic interferometer*, Physical Review B **89** (2014) (cit. on p. 37).

[16] C. Beenakker and H. van Houten, *Quantum Transport in Semiconductor Nanostructures*, (None) **44**, 1 (1991) (cit. on pp. 11, 16).

[17] N. Beev, *Lowtemp · Wiki · Projects / Electronics Design* (cit. on p. II).

[18] A. Benoit et al., *A Time Domain Multiplexer for Large Arrays of High Impedance Low Temperature Bolometers*, Journal of Low Temperature Physics **151**, 940 (2008) (cit. on p. 20).

[19] B. Bertrand et al., *Fast spin information transfer between distant quantum dots using individual electrons*, Nature nanotechnology **11**, 672 (2016) (cit. on pp. 23, 3).

[20] J.-C. Besse et al., *Single-Shot Quantum Nondemolition Detection of Individual Itinerant Microwave Photons*, Physical Review X **8** (2018) (cit. on p. 71).

[21] U. Bhattacharya, S. T. Allen, and M. Rodwell, *DC - 725 GHz sampling circuits and subpicosecond nonlinear transmission lines using elevated coplanar waveguide*, IEEE Microwave and Guided Wave Letters **5**, 50 (1995) (cit. on p. 108).

[22] J. Biamonte et al., *Quantum machine learning*, Nature **549**, 195 (2017) (cit. on p. 4).

[23] A. Bienfait et al., *Reaching the quantum limit of sensitivity in electron spin resonance*, Nature nanotechnology **11**, 253 (2016) (cit. on p. 46).

[24] D. Bimberg, ed., *Semiconductor nanostructures*, Nanoscience and technology (Springer, Berlin and Heidelberg, 2008) (cit. on p. 11).

[25] BIPM, *9th edition of the SI Brochure*, (2019) (cit. on p. XVII).

[26] S. Birner, *nextnano Tutorial mobility calculation in 2DEGs*, 19/06/2017 (cit. on pp. 13, 14, 37, XIV).

[27] R. Bisognin et al., *Microwave photons emitted by fractionally charged quasiparticles*, Nature communications **10**, 1708 (2019) (cit. on p. 23).

[28] K. Bladh et al., *Comparison of cryogenic filters for use in single electronics experiments*, Review of Scientific Instruments **74**, 1323 (2003) (cit. on p. 70).

[29] X. Blase, *An introduction to solid-state physics: International summer School in electronic structure Theory: electron correlation in Physics and Chemistry*, 10/11/2015 (cit. on p. 8).

[30] E. Bocquillon et al., *Coherence and indistinguishability of single electrons emitted by independent sources*, Science **339**, 1054 (2013) (cit. on pp. 23, 3).

[31] E. Bocquillon et al., *Electron quantum optics in ballistic chiral conductors*, Annalen der Physik **526**, 1 (2014) (cit. on p. 16).

[32] L. Bogani and W. Wernsdorfer, *Molecular spintronics using single-molecule magnets*, Nature Materials **7**, 179 (2008) (cit. on p. 67).

[33] A. Briggs, *Characterization of some chip resistors at low temperatures*, Cryogenics **31**, 932 (1991) (cit. on p. III).

[34] E. D. Buchanan et al., *Cryogenic applications of commercial electronic components*, Cryogenics **52**, 550 (2012) (cit. on pp. II, III).

[35] M. Büttiker, *Quantized transmission of a saddle-point constriction*, Physical Review B **41**, 7906 (1990) (cit. on p. 19).

[36] C. Cabart et al., *Taming electronic decoherence in one-dimensional chiral ballistic quantum conductors*, Physical Review B **98**, 101 (2018) (cit. on pp. 23, 24, 27, 4).

[37] J. Chen et al., *Classical Simulation of Intermediate-Size Quantum Circuits* (cit. on p. 4).

[38] K. S. Chou et al., *Deterministic teleportation of a quantum gate between two logical qubits*, Nature **561**, 368 (2018) (cit. on p. 54).

[39] Cirac and Zoller, *Quantum Computations with Cold Trapped Ions*, Physical review letters **74**, 4091 (1995) (cit. on p. XIII).

[40] L. COAX CO., *Coaxial cable SC-219/50-SSS-SS* (cit. on p. 76).

[41] L. A. Coldren, S. W. Corzine, and M. Mashanovitch, *Diode lasers and photonic integrated circuits*, 2nd ed., Vol. 218 (Wiley, 2012) (cit. on p. 9).

[42] J. I. Colless and D. J. Reilly, *Modular cryogenic interconnects for multi-qubit devices*, The Review of scientific instruments **85**, 114706 (2014) (cit. on p. 78).

[43] COMSOL, *Transmission Line Parameter Calculator App* (cit. on pp. 32, 74, 75, XIV, 5).

[44] I. D. Conway Lamb et al., *An FPGA-based instrumentation platform for use at deep cryogenic temperatures*, The Review of scientific instruments **87**, 014701 (2016) (cit. on p. 67).

[45] J. H. Davies, *The physics of low-dimensional semiconductors: An introduction* (Cambridge University Press, 1998) (cit. on pp. 9, 12).

[46] J. H. Davies, I. A. Larkin, and E. V. Sukhorukov, *Modeling the patterned two–dimensional electron gas: Electrostatics*, Journal of Applied Physics **77**, 4504 (1995) (cit. on pp. 36, 5).

[47] Delft Circuits, *CrioFlex* (cit. on pp. 75, 76).

[48] M. H. Devoret and R. J. Schoelkopf, *Superconducting circuits for quantum information: An outlook*, Science (New York, N.Y.) **339**, 1169 (2013) (cit. on p. 67).

[49] L. DiCarlo et al., *System for measuring auto- and cross correlation of current noise at low temperatures*, Review of Scientific Instruments **77**, 073906 (2006) (cit. on p. 64).

[50] D. P. DiVincenzo, *The Physical Implementation of Quantum Computation*, Fortschritte der Physik **48**, 771 (2000) (cit. on p. XIII).

[51] Q. Dong et al., *Ultra-low noise high electron mobility transistors for high-impedance and low-frequency deep cryogenic readout electronics*, Applied Physics Letters **105**, 013504 (2014) (cit. on p. 61).

[52] J. P. Dowling and G. J. Milburn, *Quantum technology: The second quantum revolution*, Philosophical transactions. Series A, Mathematical, physical, and engineering sciences **361**, 1655 (2003) (cit. on p. 2).

[53] D. Drung, J. Storm, and J. Beyer, *SQUID Current Sensor With Differential Output*, IEEE Transactions on Applied Superconductivity **23**, 1100204 (2013) (cit. on p. 61).

[54] J. Dubois et al., *Integer and fractional charge Lorentzian voltage pulses analyzed in the framework of photon-assisted shot noise*, Physical Review B **88**, 225 (2013) (cit. on pp. 23, 25).

[55] H. Duprez et al., *Transferring the quantum state of electrons across a Fermi sea with Coulomb interaction* (cit. on pp. 116, 10).

[56] H. Edlbauer et al., *Non-universal transmission phase behaviour of a large quantum dot*, Nature communications **8**, 1710 (2017) (cit. on pp. 116, 10).

[57] A. Einstein, *Method for the determinination of the statistical values of observations concerning quantities subject to irregular fluctuations*, IEEE ASSP Magazine **4**, 6 (1987) (cit. on p. 46).

[58] D. Ferraro et al., *Wigner function approach to single electron coherence in quantum Hall edge channels*, Physical Review B **88**, 205303 (2013) (cit. on pp. 22, 23, 3).

[59] G. Fève et al., *An on-demand coherent single-electron source*, Science (New York, N.Y.) **316**, 1169 (2007) (cit. on p. 27).

[60] M. Fink et al., *Measurement of mechanical properties of electronic materials at temperatures down to 4.2K*, Cryogenics **48**, 497 (2008) (cit. on pp. II, III).

[61] D. J. Fixsen et al., *A low noise thermometer readout for ruthenium oxide resistors*, Review of Scientific Instruments **73**, 3659 (2002) (cit. on p. III).

[62] J. D. Fletcher et al., *Clock-controlled emission of single-electron wave packets in a solid-state circuit*, Physical review letters **111**, 216807 (2013) (cit. on p. 28).

[63] B. Foxen et al., *Qubit compatible superconducting interconnects*, Quantum Science and Technology **3**, 014005 (2018) (cit. on p. 78).

[64] B. M. Freeman, J. S. Schoenfield, and H. Jiang, *Comparison of low frequency charge noise in identically patterned Si/SiO 2 and Si/SiGe quantum dots*, Applied Physics Letters **108**, 253108 (2016) (cit. on p. 58).

[65] G. Giedke and J. Ignacio Cirac, *Characterization of Gaussian operations and distillation of Gaussian states*, Physical Review A **66**, 1260 (2002) (cit. on p. 24).

[66] D. C. Glattli and P. S. Roulleau, *Levitons for electron quantum optics*, physica status solidi (b) **254**, 1600650 (2017) (cit. on pp. 117, 10).

[67] D. C. Glattli et al., *A noise detection scheme with 10 mK noise temperature resolution for semiconductor single electron tunneling devices*, Journal of Applied Physics **81**, 7350 (1997) (cit. on pp. 68–70).

[68] R. J. Glauber, *Quantum Theory of Optical Coherence* (Wiley-VCH Verlag GmbH & Co. KGaA, Weinheim, Germany, 2006) (cit. on p. 21).

[69] C. Grenier et al., *Electron quantum optics in quantum hall edge channels*, Modern Physics Letters B **25**, 1053 (2011) (cit. on p. 21).

[70] R. Gross and A. Marx, *Festkörperphysik*, 2., aktualisierte Auflage (De Gruyter, Berlin and Boston, 2014) (cit. on p. 8).

[71] C. W. Groth et al., *Kwant: A software package for quantum transport*, New Journal of Physics **16**, 063065 (2014) (cit. on pp. 19, 20, 36, 37, XIV, 5).

[72] E. Grumbling and M. Horowitz, *Quantum Computing* (National Academies Press, Washington, D.C., 2018) (cit. on pp. 2, 4).

[73] L. Hai-Ou et al., *Controlled Quantum Operations of a Semiconductor Three-Qubit System*, Physical Review Applied **9** (2018) (cit. on p. 5).

[74] A. Hammoud et al., « Performance of surface-mount ceramic and solid tantalum capacitors for cryogenic applications, » in 1998 Annual report conference on electrical insulation and dielectric phenomena (1998), pp. 572–576 (cit. on p. III).

[75] G. Hasnain, A. Dienes, and J. R. Whinnery, *Dispersion of Picosecond Pulses in Coplanar Transmission Lines*, IEEE Transactions on Microwave Theory and Techniques **34**, 738 (1986) (cit. on p. 34).

[76] N. W. Hendrickx et al., *Gate-controlled quantum dots and superconductivity in planar germanium*, Nature communications **9**, 2835 (2018) (cit. on pp. 58, XIII).

[77] H. Homulle and E. Charbon, *Cryogenic low-dropout voltage regulators for stable low-temperature electronics*, Cryogenics **95**, 11 (2018) (cit. on p. 98).

[78] P. Horowitz and W. Hill, *The art of electronics*, Third edition (Cambridge University Press, New York, NY, 2015) (cit. on pp. 47, 51, 58).

[79] T. Ihn, *Semiconductor nanostructures: Quantum states and electronic transport / Thomas Ihn* (Oxford University Press, Oxford, 2010) (cit. on p. 11).

[80] Ioffe Institute Archive, *Band structure and carrier concentration of Gallium Arsenide (GaAs)*, 24/02/2009 (cit. on p. 13).

[81] Ioffe Institute Archive, *Aluminium Gallium Arsenide (AlGaAs) - Band structure and carrier concentration*, 26/12/2002 (cit. on p. 14).

[82] D. A. Ivanov, H. W. Lee, and L. S. Levitov, *Coherent states of alternating current*, Physical Review B **56**, 6839 (1997) (cit. on pp. 23, 3).

[83] Y. Ji et al., *An electronic Mach-Zehnder interferometer*, Nature **422**, 415 (2003) (cit. on pp. 23, 3).

[84] Y. Jin et al., *Ultra-low noise HEMTs for high-impedance and low- frequency preamplifiers: Realization and characterization from 4.2 K to 77 K*, Journal of Physics: Conference Series **568**, 032009 (2014) (cit. on pp. 61, 6).

[85] H. O. Johansson and C. Svensson, *Time resolution of NMOS sampling switches used on low-swing signals*, IEEE Journal of Solid-State Circuits **33**, 237 (1998) (cit. on pp. 85, 8).

[86] E. Joos and H. D. Zeh, *The emergence of classical properties through interaction with the environment*, Zeitschrift für Physik B Condensed Matter **59**, 223 (1985) (cit. on p. XII).

[87] T. Jullien et al., *Quantum tomography of an electron*, Nature **514**, 603 (2014) (cit. on pp. 23, 25, 3, 4).

[88] M. Kahrs, *50 years of RF and microwave sampling*, IEEE Transactions on Microwave Theory and Techniques **51**, 1787 (2003) (cit. on p. 82).

[89] M. Kapfer et al., *A Josephson relation for fractionally charged anyons*, Science (New York, N.Y.) **363**, 846 (2019) (cit. on pp. 25, 117, 4).

[90] J. Keeling, I. Klich, and L. S. Levitov, *Minimal excitation states of electrons in one-dimensional wires*, Physical review letters **97**, 116403 (2006) (cit. on pp. 23, 3).

[91] J. Kelly et al., *Physical qubit calibration on a directed acyclic graph* (cit. on p. 54).

[92] E. C. Kemble, *A Contribution to the Theory of the B. W. K. Method*, Physical Review **48**, 549 (1935) (cit. on p. 19).

[93] H. N. Khan, D. A. Hounshell, and E. R. H. Fuchs, *Science and research policy at the end of Moore's law*, Nature Electronics **1**, 14 (2018) (cit. on p. 2).

[94] J.-Y. Kim et al., « Wideband characterization of multiple bondwires for millimeter-wave applications, » in 2000 Asia-Pacific microwave conference proceedings (2000), pp. 1265–1268 (cit. on p. 40).

[95] C. Kittel, *Introduction to solid state physics*, 8th ed. (John Wiley, Hoboken, N.J., 2005) (cit. on p. 12).

[96] P. V. Klimov et al., *Fluctuations of Energy-Relaxation Times in Superconducting Qubits*, Physical Review Letters **121** (2018) (cit. on p. 61).

[97] K. von Klitzing, *Quantum Hall Effect: Discovery and Application*, Annual Review of Condensed Matter Physics **8**, 13 (2017) (cit. on p. 16).

[98] C. Kloeffel and D. Loss, *Prospects for Spin-Based Quantum Computing in Quantum Dots*, Annual Review of Condensed Matter Physics **4**, 51 (2013) (cit. on p. XIII).

[99] S. Krinner et al., *Engineering cryogenic setups for 100-qubit scale superconducting circuit systems*, 2018 (cit. on pp. 67, 78).

[100] H. Kroemer, *Nobel Lecture: Quasielectric fields and band offsets: teaching electrons new tricks*, Reviews of Modern Physics **73**, 783 (2001) (cit. on pp. 9, 14, 15).

[101] F. Kuemmeth and C. M. Marcus, « Reducing noise and temperature during measurements in cryostats, » pat. 9826622 (27/08/2013) (cit. on p. 70).

[102] A. Kumar et al., *Nonconventional odd-denominator fractional quantum Hall states in the second Landau level*, Physical review letters **105**, 246808 (2010) (cit. on p. 16).

[103] P. Kurpiers et al., *Characterizing the attenuation of coaxial and rectangular microwave-frequency waveguides at cryogenic temperatures*, EPJ Quantum Technology **4**, 771 (2017) (cit. on p. 75).

[104] S. Landrein, *Illustrations and artworks* (cit. on p. 5).

[105] T. W. Larsen et al., *Semiconductor-Nanowire-Based Superconducting Qubit*, Physical review letters **115**, 127001 (2015) (cit. on p. XIII).

[106] G. B. Lesovik and I. A. Sadovskyy, *Scattering matrix approach to the description of quantum electron transport*, Physics-Uspekhi **54**, 1007 (2011) (cit. on p. 17).

[107] L. S. Levitov, H. Lee, and G. B. Lesovik, *Electron counting statistics and coherent states of electric current*, Journal of Mathematical Physics **37**, 4845 (1996) (cit. on pp. 23, 25, 28, 3).

[108] Lew Yan Voon, L. C. and M. Willatzen, *The k.p method: Electronic properties of semiconductors* (Springer, Dordrecht and London, 2009) (cit. on p. 13).

[109] E. H. Lieb and D. W. Robinson, *The finite group velocity of quantum spin systems*, Communications in Mathematical Physics **28**, 251 (1972) (cit. on p. 3).

[110] Linear Technology Corporation, *AN124 - 775 Nanovolt Noise Measurement for A Low Noise Voltage Reference*, (cit. on p. 52).

[111] G.-Q. Liu et al., *Coherent quantum control of nitrogen-vacancy center spins near 1000 kelvin*, Nature communications **10**, 1344 (2019) (cit. on p. 24).

[112] D. Loss and D. P. DiVincenzo, *Quantum computation with quantum dots*, Physical Review A **57**, 120 (1998) (cit. on p. XIII).

[113] J. M. Luttinger and W. Kohn, *Motion of Electrons and Holes in Perturbed Periodic Fields*, Physical Review **97**, 869 (1955) (cit. on p. 13).

[114] P. Magnone et al., *$1/f$ Noise in Drain and Gate Current of MOSFETs With High-k Gate Stacks*, IEEE Transactions on Device and Materials Reliability **9**, 180 (2009) (cit. on p. 61).

[115] P. Mahnke, *Characterization of a commercial software defined radio as high frequency lock-in amplifier for FM spectroscopy*, The Review of scientific instruments **89**, 013113 (2018) (cit. on p. 46).

[116] S. Mandal et al., *Efficient radio frequency filters for space constrained cryogenic setups*, The Review of scientific instruments **82**, 024704 (2011) (cit. on pp. 70, 71).

[117] M. J. Manfra, *Molecular Beam Epitaxy of Ultra-High-Quality AlGaAs/GaAs Heterostructures: Enabling Physics in Low-Dimensional Electronic Systems*, Annual Review of Condensed Matter Physics **5**, 347 (2014) (cit. on pp. 31, 4).

[118] I. L. Markov, *Limits on fundamental limits to computation*, Nature **512**, 147 (2014) (cit. on p. 2).

[119] I. L. Markov et al., *Quantum Supremacy Is Both Closer and Farther than It Appears*, 2018 (cit. on p. 4).

[120] J. M. Martinis and M. Nahum, *Effect of environmental noise on the accuracy of Coulomb-blockade devices*, Physical Review B **48**, 18316 (1993) (cit. on pp. 68, 73).

[121] X. Mi et al., *A coherent spin-photon interface in silicon*, Nature **555**, 599 (2018) (cit. on p. XIII).

[122] Microwave Studio, *Circular waveguide - CST Tutorial*, 6/03/2018 (cit. on p. 75).

[123] F. Mueller et al., *Printed circuit board metal powder filters for low electron temperatures*, The Review of scientific instruments **84**, 044706 (2013) (cit. on p. 70).

[124] NASA Glenn Research Center, *Low Temperature Electronics Program* (cit. on p. IV).

[125] F. D. Natterer et al., *Reading and writing single-atom magnets*, Nature **543**, 226 (2017) (cit. on p. 67).

[126] I. Neder et al., *Interference between two indistinguishable electrons from independent sources*, Nature **448**, 333 (2007) (cit. on pp. 23, 3).

[127] C. Nelson et al., *Phase Noise Suppression in Frequency Comb Generators*, (cit. on p. 112).

[128] M. A. Nielsen, *What does the quantum state mean?* 14/12/2018 (cit. on p. XII).

[129] M. A. Nielsen and I. L. Chuang, *Quantum computation and quantum information* (Cambridge University Press, Cambridge, 2000) (cit. on p. XIII).

[130] M. Okuyama and M. Ohzeki, *Quantum Speed Limit is Not Quantum*, Physical review letters **120**, 070402 (2018) (cit. on p. 3).

[131] A. V. Oppenheim and G. C. Verghese, *Signals, systems & inference*, Global edition (Pearson, Harlow, 2017) (cit. on p. 46).

[132] R. Orús, *A practical introduction to tensor networks: Matrix product states and projected entangled pair states*, Annals of Physics **349**, 117 (2014) (cit. on p. XII).

[133] R. OSI, *PRIZM LightTurn*, (cit. on p. 78).

[134] T. Owen and A. Patel, *Measuring 2nV/$\sqrt{}$Hz Noise and 120dB Supply Rejection on Linear Regulators: AN159 - Linear Technology Corporation*, (cit. on pp. 49, 52).

[135] M.-J. Pan, *Performance of capacitors under DC bias at liquid nitrogen temperature*, Cryogenics **45**, 463 (2005) (cit. on p. II).

[136] J. R. Petta et al., *Coherent manipulation of coupled electron spins in semiconductor quantum dots*, Science (New York, N.Y.) **309**, 2180 (2005) (cit. on p. 20).

[137] PhD students, *Lab instruments' drivers - coworking space shared on GitHub* (cit. on p. XIV).

[138] N. Picqué and T. W. Hänsch, *Frequency comb spectroscopy*, Nature Photonics **13**, 146 (2019) (cit. on p. 108).

[139] D. M. Pozar, *Microwave engineering*, 4th ed. (Wiley, Hoboken, NJ, 2012) (cit. on p. 74).

[140] Python Software Foundation, *PyPI – the Python Package Index* (cit. on p. XIV).

[141] R. Ran and T. Avishay, *Oracle Separation of BQP and PH* (cit. on p. 4).

[142] D. J. Reilly et al., *Fast single-charge sensing with a rf quantum point contact*, Applied Physics Letters **91**, 162101 (2007) (cit. on p. III).

[143] M. Rodwell et al., *GaAs nonlinear transmission lines for picosecond pulse generation and millimeter-wave sampling*, IEEE Transactions on Microwave Theory and Techniques **39**, 1194 (1991) (cit. on p. 108).

[144] H. Rosenberger, *Spring Loaded Coax System*, (cit. on p. 78).

[145] G. Rosselló et al., *Interference and multiparticle effects in a Mach-Zehnder interferometer with single-particle sources*, Physical Review B **91** (2015) (cit. on pp. 117, 10).

[146] B. Roussel et al., *Electron quantum optics as quantum signal processing*, physica status solidi (b) **254**, 1600621 (2017) (cit. on p. 23).

[147] G. Roussely et al., *Unveiling the bosonic nature of an ultrashort few-electron pulse*, Nature communications **9**, 2811 (2018) (cit. on pp. 25, 4).

[148] E. Rubiola, *Phase noise and frequency stability in oscillators*, The Cambridge RF and microwave engineering series (Cambridge University Press, New York, 2009) (cit. on pp. 43, 53).

[149] N. Samkharadze et al., *Strong spin-photon coupling in silicon*, Science (New York, N.Y.) (2018) (cit. on pp. 5, XIII).

[150] P. Scarlino et al., *Coherent microwave photon mediated coupling between a semiconductor and a superconductor qubit* (cit. on p. XIII).

[151] C. P. Scheller et al., *Silver-epoxy microwave filters and thermalizers for millikelvin experiments*, Applied Physics Letters **104**, 211106 (2014) (cit. on p. 70).

[152] M. J. A. Schuetz et al., *Acoustic Traps and Lattices for Electrons in Semiconductors*, Physical Review X **7** (2017) (cit. on p. 3).

[153] J. Schuster et al., *Interlayer charge transfer in n-modulation doped Al1−x Ga x As–GaAs single heterostructures*, Semiconductor Science and Technology **33**, 095020 (2018) (cit. on pp. 31, 4).

[154] C. E. Shannon, *Communication in the Presence of Noise*, Proceedings of the IRE **37**, 10 (1949) (cit. on p. 45).

[155] A. Skwarek et al., *Electrical properties of thin-film resistors in a wide temperature range*, Circuit World **41**, 116 (2015) (cit. on p. II).

[156] P. R. Smith, D. H. Auston, and W. M. Augustyniak, *Measurement of GaAs field–effect transistor electronic impulse response by picosecond optical electronics*, Applied Physics Letters **39**, 739 (1981) (cit. on p. 82).

[157] Southwest Microwave, *Optimizing-Test-Boards-for-50-GHz-End-Launch-Connectors*, (cit. on p. 100).

[158] J. Splettstoesser and R. J. Haug, *Single-electron control in solid state devices*, physica status solidi (b) **254**, 1770217 (2017) (cit. on pp. 22, 3).

[159] S. Stahl, *Cryogenic Low Pass Filter Unit Datasheet KA-Fil2a*, (cit. on p. 70).

[160] R. L. Swerlein, *Precision AC Voltage Measurements Using Digital Sampling Techniques*, (cit. on p. 57).

[161] S. Takada et al., *Transmission phase in the Kondo regime revealed in a two-path interferometer*, Physical review letters **113**, 126601 (2014) (cit. on p. 31).

[162] E. Tang, *A quantum-inspired classical algorithm for recommendation systems*, (cit. on p. 4).

[163] J. R. Taylor, *An introduction to error analysis: The study of uncertainties in physical measurements*, 2nd ed. (University Science, 1997) (cit. on p. XIV).

[164] Texas Instruments, *Considerations for High-Gain Multistage Designs: SBOA135*, (cit. on p. 51).

[165] M. Thalmann et al., *Comparison of cryogenic low-pass filters*, The Review of scientific instruments **88**, 114703 (2017) (cit. on pp. 67, 70).

[166] D. B. Tuckerman et al., *Flexible superconducting Nb transmission lines on thin film polyimide for quantum computing applications*, Superconductor Science and Technology **29**, 084007 (2016) (cit. on p. 75).

[167] J. Valdmanis and G. Mourou, *Subpicosecond electrooptic sampling: Principles and applications*, IEEE Journal of Quantum Electronics **22**, 69 (1986) (cit. on pp. 82, 7).

[168] B. J. van Wees et al., *Quantized conductance of point contacts in a two-dimensional electron gas*, Physical review letters **60**, 848 (1988) (cit. on pp. 18, 19).

[169] D. M. T. van Zanten et al., *Single Quantum Level Electron Turnstile*, Physical review letters **116**, 166801 (2016) (cit. on pp. 23, 3).

[170] L. M. K. Vandersypen et al., *Interfacing spin qubits in quantum dots and donors—hot, dense, and coherent*, npj Quantum Information **3**, 34 (2017) (cit. on p. XIII).

[171] M. Vanević, Y. V. Nazarov, and W. Belzig, *Elementary events of electron transfer in a voltage-driven quantum point contact*, Physical review letters **99**, 076601 (2007) (cit. on p. 26).

[172] P. Vogl, H. P. Hjalmarson, and J. D. Dow, *A Semi-empirical tight-binding theory of the electronic structure of semiconductors*, Journal of Physics and Chemistry of Solids **44**, 365 (1983) (cit. on p. 13).

[173] B. C. Wadell, *Transmission line design handbook* (1991) (cit. on pp. 32, 34, XI, 5).

[174] X. Waintal and C. W. Groth, *kwant software package* (cit. on pp. 36, 5).

[175] M. M. Waldrop, *The chips are down for Moore's law*, Nature **530**, 144 (2016) (cit. on p. 9).

[176] W. Walukiewicz et al., *Electron mobility in modulation-doped heterostructures*, Physical Review B **30**, 4571 (1984) (cit. on pp. 14, 15).

[177] S. Weinreb, J. C. Bardin, and H. Mani, *Design of Cryogenic SiGe Low-Noise Amplifiers*, IEEE Transactions on Microwave Theory and Techniques **55**, 2306 (2007) (cit. on pp. 61, III).

[178] C. Weisbuch and B. Vinter, *Quantum semiconductor structures: Fundamentals and applications* (Academic Press, Boston, 1991) (cit. on p. 14).

[179] W. E. Weisstein, *Cauchy Distribution From MathWorld - A Wolfram Web Resource.* (Cit. on p. IX).

[180] V. Wong, *ADA4530-1 Femtoampere Level Input Bias Current Measurement: AN-1373*, (cit. on p. 51).

[181] K. Wu, D. Desiandes, and Y. Cassivi, « The substrate integrated circuits - a new concept for high-frequency electronics and optoelectronics, » in 6th International conference on telecommunications in modern satellite cable and broadcasting services, edited by B. D. Milovanović (2003), P–III–P–X (cit. on p. 36).

[182] C. H. Yang et al., *Silicon quantum processor unit cell operation above one Kelvin* (cit. on p. 24).

[183] C. H. Yang et al., *Silicon qubit fidelities approaching incoherent noise limits via pulse engineering*, Nature Electronics **2**, 151 (2019) (cit. on pp. 5, 42, 54).

[184] J. Ye and S. T. Cundiff, eds., *Femtosecond optical frequency comb: Principle, operation, and applications* (Springer, New York, 2010) (cit. on p. 108).

[185] J. Yoneda et al., *A quantum-dot spin qubit with coherence limited by charge noise and fidelity higher than 99.9%*, Nature nanotechnology **13**, 102 (2018) (cit. on p. 5).

[186] A. Zonca et al., *Modeling the frequency response of microwave radiometers with QUCS*, Journal of Instrumentation **5**, T12001 (2010) (cit. on pp. 36, XIV).

[187] F. A. Zwanenburg et al., *Silicon quantum electronics*, Reviews of Modern Physics **85**, 961 (2013) (cit. on p. 67).